Irradiation damage concurrent challenges with RAFM and ODS steels for fusion reactor first-wall/blanket: a review

Journal of Physics: Energy

PAPER

Irradiation damage concurrent challenges with RAFM and ODS steels for fusion reactor first-wall/blanket: a review

Arunodaya Bhattacharya[1,*], **Steven J Zinkle**[1,2], **Jean Henry**[3], **Samara M Levine**[2], **Philip D Edmondson**[1], **Mark R Gilbert**[5], **Hiroyasu Tanigawa**[6] and **Charles E Kessel**[4]

[1] Materials Science and Technology Division, Oak Ridge National Laboratory, Oak Ridge, TN, United States of America
[2] University of Tennessee, Knoxville, TN, United States of America
[3] Université Paris-Saclay, CEA, Service de Recherches Métallurgiques Appliquées, 91191 Gif-sur-Yvette, France
[4] Fusion Energy Division, Oak Ridge National Laboratory, Oak Ridge, TN, United States of America
[5] United Kingdom Atomic Energy Authority, Culham Centre for Fusion Energy, Culham Science Centre, Abingdon, Oxford OX14 3DB, United Kingdom
[6] National Institutes for Quantum Science and Technology, Rokkasho, Aomori, Japan
* Author to whom any correspondence should be addressed.

E-mail: bhattacharya@ornl.gov

Keywords: RAFM steels, ODS steels, fusion reactor, irradiation damage, design, fusion neutron science facility

Supplementary material for this article is available online

OPEN ACCESS

RECEIVED
30 November 2021

REVISED
20 March 2022

ACCEPTED FOR PUBLICATION
13 May 2022

PUBLISHED
6 July 2022

Abstract

Reduced activation ferritic martensitic (RAFM) and oxide dispersion strengthened (ODS) steels are the most promising candidates for fusion first-wall/blanket (FW/B) structures. The performance of these steels will deteriorate during service due to neutron damage and transmutation-induced gases, such as helium/hydrogen, at elevated operating temperatures. Here, after highlighting the operating conditions of fusion reactor concepts and a brief overview, the main irradiation-induced degradation challenges associated with RAFM/ODS steels are discussed. Their long-term degradation scenarios such as (a) low-temperature hardening embrittlement (LTHE)—including dose-temperature dependent yield stress, tensile elongations, necking ductility, test temperature effect on hardening, Charpy impact ductile-to-brittle transition temperature and fracture toughness, (b) intermediate temperature cavity swelling, (c) the effect of helium on LTHE and cavity swelling, (d) irradiation creep and (e) tritium management issues are reviewed. The potential causes of LTHE are discussed, which highlights the need for advanced characterisation techniques. The mechanical properties, including the tensile/Charpy impact of RAFM and ODS steels, are compared to show that the current generation of ODS steels also suffers from LTHE, and shows irradiation hardening up to high temperatures of ∼400 °C–500 °C. To minimise this, future ODS steel development for FW/B-specific application should target materials with a lower Cr concentration (to minimise α'), and minimise other elements that could form embrittling phases under irradiation. RAFM steel-designing activities targeting improvements in creep and LTHE are reviewed. The need to better understand the synergistic effects of helium on the thermo-mechanical properties in the entire temperature range of FW/B is highlighted. Because fusion operating conditions will be complex, including stresses due to the magnetic field, primary loads like coolant pressure, secondary loads from thermal gradients, and due to spatial variation in damage levels and gas production rates, an experimentally validated multiscale modelling approach is suggested as a pathway to future reactor component designing such as for the fusion neutron science facility.

1. Introduction

The Fe(8–9)%Cr-based reduced activation ferritic martensitic (RAFM) steels are the most promising candidates for fusion first-wall/blanket (FW/B) structures [1–5]. In the interest of maintaining the vision for fusion as clean energy with few harmful radioactive by-products, RAFM steels were originally derived from 9Cr–1Mo steels to facilitate simplified waste management like shallow land burial or the possibility of material recycling. As a result, radiologically undesirable neutron activation prone elements with long decay half-lives, such as Nb and Mo, are replaced by metallurgically equivalent relatively low activation elements, Ta and W [6–8]. Further, severe restrictions are imposed on the concentrations of other elements like Cu, Co, Al, Ni and various impurities to limit the generation of high long-term radioactivity [7]. The ideas of a RAFM steel concept were postulated in the early 80s [9]. In the mid-80s, this gave birth to the very first successful normalised-tempered 9%Cr RAFM steel designs based on Cr–W–V–Ta by researchers in the US at oak ridge national lab (ORNL) [10, 11], by JAEA in Japan [12] and almost simultaneously by researchers in the UK at Culham lab and British Steel [13]. Following this, several experimental RAFM steels using a combination of slightly different micro-alloying chemistries and heat treatment conditions have been developed in the US [7, 10, 11, 14–16], Japan [12, 17–20], UK [21] and Europe [22–27]. More recently China [28, 29], India [30, 31], Russia [32, 33] and South Korea [34–36] are developing their own RAFM steel variants. The design philosophy of RAFM steels is to obtain the desired material properties with a tempered martensitic structure that combines high strength due to martensitic transformation producing laths, followed by incorporating a high density of precipitates such as $M_{23}C_6$ carbides and MX carbonitrides that render high-temperature strength [5, 16, 37–39]. Precipitates in RAFM steels also act as a sink for point defects, thereby improving the overall irradiation performance of the steels. Following a normalisation treatment in the range of ∼980 °C–1150 °C, these steels are tempered at around ∼750 °C–760 °C to let carbon out from the supersaturated solid solution of the martensitic matrix that forms carbides and simultaneously recover the body-centered tetragonal crystal structure to render ductility. As a result, RAFM steels exhibit a good combination of strength (∼300–600 MPa) and tensile ductility (>9%–10%) in normalised-tempered state up to ∼500 °C [7, 38, 40–42]. By far, the most well-studied RAFM steels with the largest database of material properties exist for 8Cr2WVTa F82H [40, 43], which was initially produced in Japan in 1992 as a part of an international collaboration and for 9Cr1WVTa Eurofer97 steel developed in Europe since the late 1990s [23, 44, 45]. Specifically, the Eurofer97 steel fabricated using clean steel-making processes has achieved the major milestone of being recently code-qualified with non-irradiated property data in the RCC-MRx French reactor construction code that will be used to build the DEMO reactor [44], while efforts are ongoing to achieve code qualification of F82H in RCC-MRx [46]. A specificity of fusion reactors is that construction codes such as RCC-MRx require full code qualification of RAFM steels with neutron-irradiated properties, for which international collaborative research is ongoing jointly between the fusion programmes of Japan, the EU and the US to generate relevant neutron-irradiated properties for both Eurofer97 and F82H.

Initially not considered for fusion, fearing potential deleterious interactions of ferromagnetic steels with strong magnetic fields inside fusion reactors [47], the primary reason for the choice of RAFM steel in fusion reactors is driven by its cavity swelling resistance in irradiation environments [48–50]. This is because the operating conditions envisaged for the fusion FW/B are severe. While the ITER test blanket module (TBM) dose-temperature range is rather limited (∼2.5–3 dpa, ∼300 °C), fusion power demonstration concepts such as DEMO in EU/Japan and the Fusion Neutron Science Facility (FNSF) in the US will experience much worse irradiation damage compared to ITER (see figure 1). Currently, DEMO first-phase operations are expected to receive a maximum of ∼20 dpa in RAFM steels' starter blanket, rising up to ∼50 dpa for the second blanket. For the FNSF concept in the US, the neutron doses are not expected in Phase 1 (He/H plasma, known as the shakedown phase) and Phase 2 (deuterium–deuterium (DD) fusion, known as the plasma pulse extension phase) [51]. But significant neutron wall loading ramp-up in FNSF is expected from Phase 3 onwards with deuterium–tritium (DT) fusion reaction, where the doses and operating temperatures will be similar to DEMO [52–54] (figure 1). This means RAFM steels must at least survive $\leqslant$3 dpa for ITER-TBMs to be successful and ∼10–20 dpa for early-phase operations of FNSF or DEMO to be successful under relevant operating temperatures. For a full power generating fusion reactor, the end-of-life doses in the range of ∼150–200 dpa are expected over a wide temperature range [1]. Additionally, transmutation of Fe atoms in steels by 14 MeV neutrons will produce ∼10 atomic parts per million (appm) helium (He)/dpa and ∼45–50 appm hydrogen (H)/dpa in the near-plasma regions [55, 56]. In such scenarios, the well-studied 300 series Fe–Cr–Ni austenitic steels are unsuitable due to dimensional instabilities by cavity swelling that a high-dose irradiation environment with simultaneous generation of He/H will trigger [1, 49, 57]. In addition to cavity swelling resistance, RAFM steels have numerous other attractive properties as compared to austenitics, such as high strength, high thermal conductivity, low coefficient of thermal expansion, relatively

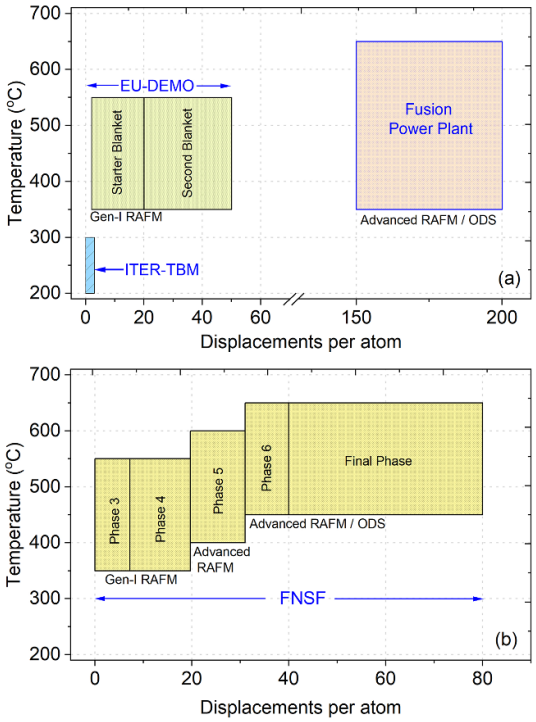

Figure 1. Operating temperatures and neutron dose regimes of fusion FW/B steel structures in different fusion reactor concepts. For FNSF in the US, neutron dose ramp-up is expected from Phase 3 onwards with DT fusion and conditions similar to European Union (EU) DEMO [51, 54], while no dpa is expected in Phase 1 (He/H fusion) and Phase 2 (DD fusion). The ITER-TBM and DEMO conditions obtained from [52, 57, 59].

low cost due to the absence of Ni, and ease of fabrication by the well-established conventional steel making process of casting-forging-rolling [7, 39, 58].

1.1. Major challenges for RAFM steels

The chief concern with current generation (Gen-I) RAFM steels is the projected very narrow operational temperature window of ∼350 °C–550 °C in fusion environments [45, 54, 58]. The lower temperature limit is imposed due to the irradiation-induced low-temperature hardening embrittlement (LTHE) phenomenon, resulting in an increase of yield and tensile strength, loss of tensile elongation and severe loss of fracture toughness (FT) with an increase in ductile-to-brittle transition temperature (DBTT) for neutron doses as low as ∼0.1–15 dpa and irradiation temperatures (T_{irr}) ⩽ ∼350 °C [38, 60–66]. LTHE is a major challenge in reactor design, particularly for the water-cooled DEMO blanket concepts, where operating temperatures in the range of ∼280 °C–350 °C are expected [67]. The lower operating temperatures envisaged especially for the early phases of FNSF (based on a dual-cooled lead lithium blanket design) are also very close to the temperature range where LTHE issues may pose a challenge—especially due to added uncertainties regarding the effect of helium (see figure 1). The upper temperature limit is imposed due to poor thermal ageing behaviour and loss of creep strength in the range of ∼550 °C–600 °C [45, 58, 61, 68, 69], which might further worsen with neutron irradiation and He/H co-generation in the steel [70]. In fact, the high-temperature thermal creep properties of RAFM steels are worse than many present-day 9%Cr steels, and equivalent to the second-generation Grade91/92 steel properties [70–77]. The upper temperature limit, that limits the thermodynamic efficiency of a power plant, is a critical challenge for He or dual-cooled blanket designs, where operating temperatures in the range of ∼600 °C–650 °C are envisaged [78, 79]. Further, fatigue and creep–fatigue interactions that cause cyclic softening of RAFM steels severely limit the maximum allowable design stresses [70, 80–84]. It is also worth noting that cavityswelling scenarios in RAFM steels are not fully mapped out, and it is quite likely that enhanced swelling will occur under a fusion neutron spectrum, synergistically aided by He/H generation beyond >20–50 dpa that could pose unacceptable dimensional instabilities further worsened with anticipated swelling–creep–fatigue interactions. Due to thelimited number of fusion-relevant neutron irradiation experiments, the performance of RAFM steels in the intermediate temperature range (∼400 °C–500 °C) is also not fully evaluated to identify acceptable lifetime doses affected by cavity swelling and other degradation mechanisms. Specifically, the deleterious effect of He on LTHE [65, 85, 86], cavity swelling [49, 87, 88] or high-temperature mechanical

properties [89] may further narrow the acceptable temperature range of RAFM steel's operations; this needs to be fully mapped out. In addition, uncertainties exist regarding the performance of RAFM weldments and heat-affected zones (HAZs) in fusion blankets. RAFM steels require post-weld heat treatments (PWHTs) that will be challenging in full-size breeding blankets and TBMs with the presence of many other complex welded components of different thicknesses. The gap between typical PWHTs and tempering treatments carried out at 750 °C–780 °C is quite narrow [90–93], further complicating this operation on bulky multi-shaped components due to the required accuracy of the temperature control [68]. Moreover, the behaviour of welds and HAZs under neutron irradiation is not sufficiently quantified, due to which uncertainties remain in predicting their performance. With the initial tempered martensitic structure largely modified in the HAZs [92], it is unclear how He might further worsen the fast fracture properties relevant for low-temperature operations and thermal/irradiation creep combined with swelling scenarios in mid- to high-temperature blanket operations. In the following sections, the irradiation damage scenarios of RAFM and oxide dispersion-strengthened (ODS) steels are presented to highlight their implications on FW/B designing for fusion reactors including DEMO and US FNSF, and the necessity to design high-performance alloys.

2. Low temperature hardening-embrittlement (LTHE) in RAFM and ODS steels

2.1. Irradiation hardening and loss of ductility in RAFM steels

During neutron irradiations at relatively low temperatures ($T_{irr} \leqslant 0.4T_m$, where T_m = melting point), RAFM and conventional FM steels suffer from LTHE, with the severity depending upon T_{irr} and dose [5, 45, 66, 68, 86, 90, 94–106]. LTHE is typically quantified using post-irradiation tensile tests, FT tests and Charpy impact tests. Without irradiation, the yield stress (σ_{YS}) of RAFM steels decreases monotonically with the temperature (figure 2). Due to LTHE, an increase in σ_{YS} (hardening) and severe loss of tensile elongation occurs for $T_{irr} < 400$ °C, which is particularly pronounced for $T_{irr} < 350$ °C. Minimal hardening is observed near 450 °C–500 °C and some slight softening may occur for $T_{irr} > \sim$450 °C–500 °C (figure 2). For $T_{irr} \leqslant 350$ °C, the σ_{YS} of both conventional FM and RAFM steels tends to continually increase at lower T_{irr} values. However, the variation of irradiated σ_{YS} at lower T_{irr} and up to ∼300 °C–350 °C is relatively gradual as compared to the rapid recovery of σ_{YS} when $T_{irr} \geqslant 350$ °C. Hardening increases sharply with neutron doses as low as ∼0.1–0.2 dpa, and continues to increase up to at least ∼10–15 dpa in RAFM steels (figure 3). By ITER-relevant conditions of 2.5–3 dpa around 300 °C, RAFM steels can harden by as much as 50%–70% (∼by 350–400 MPa) compared to their initial σ_{YS} [62, 66]. After ∼15 dpa, hardening in RAFM steels such as Eurofer97 or F82H saturates and remains nearly constant up to very high doses exceeding >50–70 dpa, as shown in figure 3. The saturation in hardening with the dose is interpreted to be due to saturation in the irradiation-induced microstructural defects in these alloys. The extent of irradiation hardening in RAFM steels is much lower than in conventional FM steels such as 9Cr–1MoVNb or 9Cr–1Mo, highlighting better LTHE resistance in RAFM steels. As an example, hardening in RAFM steels can be ∼200–300 MPa lower than in 9Cr–1MoVNb steels at high doses of >60–70 dpa. Moreover, saturation in hardening, for example in 9Cr–1MoVNb, occurs at much higher doses (>40 dpa) than in RAFM steels. For the important T_{irr} region between ∼250 °C and 350 °C that is relevant for water-cooled blanket concepts, conflicting data scatters exist regarding the effect of T_{irr} on incremental radiation hardening. Some studies have reported comparable or decreased radiation hardening in RAFM steels in this temperature range [3, 5, 45, 107, 108], whereas other studies such as on Eurofer97 have reported non-monotonic T_{irr} dependence with maximum hardening at ∼300 °C [41, 109], which is difficult to explain by the current understanding of irradiation-induced microstructural phenomena. These inconsistencies between different studies are most likely associated with differences in the dose-dependent hardening up to ∼5–10 dpa at different T_{irr} values [66]. Further, a major problem with literature data is that numerous neutron irradiation studies only provide the design neutron irradiation temperatures but lack proper thermometry data and neutron flux distribution data across samples. Differences between actual versus design temperatures in neutron irradiations and neutron flux inhomogeneities across samples are known to occur, which will contribute to scatter in the measured properties [66]. Unfortunately, such effects on measured properties for neutron irradiation experiments are typically not discussed in detail in published manuscripts.

It is generally observed that harder under-tempered RAFM steels (room temperature $\sigma_{YS} > 800$–900 MPa), being designed to optimise high-temperature strength [26, 62, 144], offer a relatively low percentage increase in σ_{YS} after neutron irradiation as compared to those produced by conventional heat treatments or by over-tempering [62, 66]. The harder steels also seem to show relatively less degradation of the tensile elongation due to irradiation. This behaviour should not be interpreted as improved LTHE performance. The steels being already much harder in the non-irradiated state and having low uniform elongation means the possibility to further harden or lose ductility is lower compared to softer steels. Such steels typically show relatively inferior pre- and post-irradiation FT [64, 145, 146].

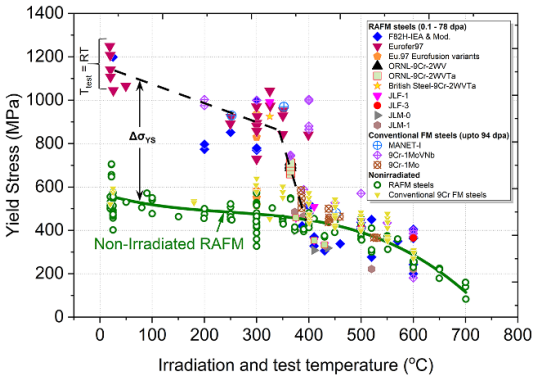

Figure 2. Yield stress of neutron-irradiated RAFM steels compared against some conventional FM steels for doses between ∼0.1 and 94 dpa, showing an increase in yield stress when $T_{irr} \leqslant 350\ ^{\circ}C$–$400\ ^{\circ}C$. Figure produced using data compiled from [5, 7, 20, 23, 41, 45, 62, 66, 86, 94, 107, 110–137].

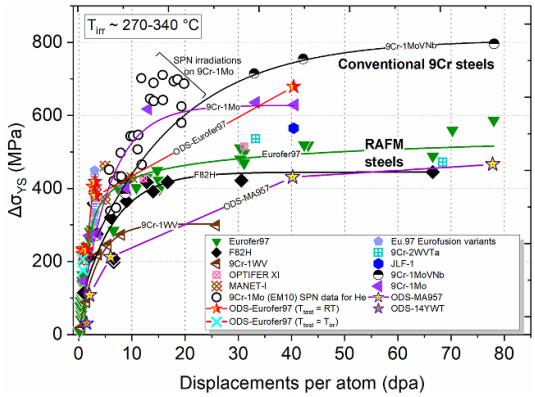

Figure 3. Irradiation hardening measured as increase in yield stress of RAFM steels compared with conventional FM and some ODS steels. Except otherwise stated in the figure, all tests performed at T_{irr}. SPN = spallation proton–neutron irradiations. Figure produced using data from [5, 66, 83, 96, 106, 114, 121, 123, 130, 136–143].

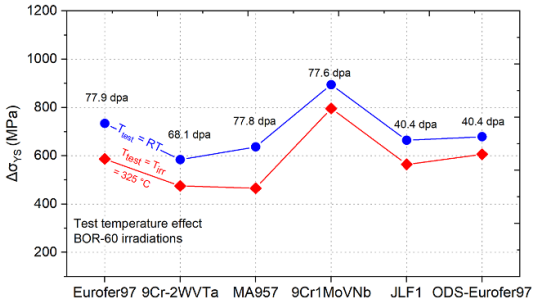

Figure 4. Effect of tensile test temperature on measured irradiation hardening. Figure compiled using data from [135].

Test temperatures play a role in the experimentally measured hardening. Typically, higher hardening is observed at lower tensile test temperatures, as shown in figure 4, where high-dose fast reactor irradiated data for a variety of steels is compiled. The yield stress increase is always much higher for tests performed at room temperature (RT) as compared to tensile testing at elevated temperatures such as T_{irr}. This behaviour is attributable to the stronger temperature dependence of the deformation activation volume for irradiation-induced defects compared to the non-irradiated value [147–149]. Dependence of the measured irradiation hardening on the test temperature implies that a single hardening value for RAFM/ODS steels should not be assumed over the temperature range of FW/B operations. The variation in irradiation hardening with the test temperature needs to be included in the engineering design of the components.

A major consequence of irradiation hardening is the severe loss of strain hardening capacity, typically measured as the ultimate tensile stress to yield stress ratio (σ_{UTS}/σ_{YS}) figure of merit. In the entire

temperature range of ITER-TBM-relevant operations, RAFM steels such as Eurofer97 or F82H show much lower strain hardening capacity as compared to 300 series austenitic steels [61]. After neutron irradiations to doses as low as 2.5–3 dpa (ITER-TBM), not much strain-hardening capacity is left in these materials with $\sigma_{UTS}/\sigma_{YS} < 1.1$ and approaching $\sigma_{UTS}/\sigma_{YS} \sim 1$ in many RAFM variants or at higher doses [45, 66]. Negligible remnant strain hardening capacity in RAFM steels after very low neutron doses is a critical design challenge, especially for the water-cooled blanket concepts, because RCC-MX/RCC-MRx imposes a minimum limit on this value; for example, Eurofer97 is currently set at a minimum $\sigma_{UTS}/\sigma_{YS} > \sim 1.18$ measured at RT in the non-irradiated condition [61, 150]. While Eurofer97 is code-qualified in RCC-MRx with non-irradiated properties and F82H will likely achieve this status soon, both these classes of materials require additional code qualification with irradiated property data for DEMO—for which joint research is ongoing at different European labs under EUROfusion for Eurofer97, in Japan for F82H, and in joint research efforts for generating irradiated property data of both Eurofer97/F82H in DOE-QST and ORNL-EUROfusion collaboration. Therefore, it remains to be seen what limits may be imposed for the irradiated properties. If the strain hardening capacity limit for irradiated steels in RCC-MRx is chosen to be similar to the values of non-irradiated steels, then it is likely that none of the Gen-I RAFM steels will meet the criteria. Historically, the reactor design programmes in Japan and EU have considered that RAFM steel will be suitable for water-cooled blanket concepts. The RCC-MX/RCC-MRx change is a relatively new modification that has not yet been assessed by other countries, including the US (and therefore it may not be required for licensing in other countries). Nevertheless, this highlights an important phenomenon that might require higher operating temperatures to avoid LTHE. In the US, code qualification activities of RAFM steels are currently not as elaborate as in Japan or the EU, but will likely be inspired by the ongoing DEMO-related activities. As detailed in figure 1, the initial development of FNSF with target doses up to 20 dpa is based on Gen-I RAFM steel designs because such steels are ahead in technology maturity level. But a shift towards advanced RAFM steels and/or a combination of RAFM-ODS steels is anticipated beyond 20 dpa. With the increasing dose, the preliminary strategy suggests a progressive increase in the lower operating temperature limit of components designed using advanced RAFM steels or ODS steels in the later FNSF phases. This strategy originates from the desire to operate a fusion reactor at higher temperatures (better for plant efficiency) [51, 54] depending upon the progress in the development of steels optimised for high-temperature performance and also likely influenced by uncertainties in LTHE behaviour at lower temperatures for steels optimised for high-temperature performance, such as ODS steels and newer RAFM steels currently in development in the US (like castable nanostructured alloy (CNA), on which no neutron-irradiated data currently exists).

Comparison of the tensile properties of neutron-irradiated FM and RAFM steels is often better expressed in true stress units, where regions of uniform plastic deformation versus the regions of no plastic deformation can be mapped as a function of irradiation-induced LTHE [66, 151, 152], as shown in figure 5. The true stress at σ_{UTS} is defined as the plastic instability stress (σ_{PIS}) [152, 153], which is constant for a given steel independent of the neutron dose [153]. The σ_{PIS} is effectively the true stress at maximum load up to which a material shows uniform plasticity as long as $\sigma_{YS} < \sigma_{PIS}$ [153]. As σ_{YS} increases with the neutron dose and approaches σ_{PIS}, the capacity to uniformly deform reduces under tensile loading conditions. When $\sigma_{YS} = \sigma_{PIS}$, no uniform deformation occurs, and the material shows plastic instability with prompt necking at yield [152]. The dose at which $\sigma_{YS} = \sigma_{PIS}$ is the critical neutron dose (Dc, in figure 5) for necking onset at yield. If dose > Dc, the worst case scenario occurs because RAFM and FM steels will show no uniform tensile ductility (although significant post-necking strain typically remains [66, 153]). Numerous values of Dc have been historically obtained for 9%Cr steels depending upon their chemistry and heat treatment condition. Generally, Dc for FM and RAFM steels ranges between ~0.04 and 0.1 dpa for $T_{irr} < 350$ °C [151–153], which are extremely small doses to lose uniform plasticity compared to the dpa values envisaged for fusion concepts like ITER, DEMO or FNSF. Therefore, alloy designing should target producing materials with a large separation between σ_{PIS} and σ_{YS}, so that the materials can maintain a relatively large work hardening margin and uniform deformation capability after irradiation, resulting in minimisation of the susceptibility to LTHE. The improvements in σ_{PIS} should not be achieved at the cost of a highly increased initial σ_{YS}, which is often the case for relatively harder RAFM steel concepts such as those produced by under-tempering to improve the high-temperature creep performance [66, 144]. However, this option may be unavoidable if high-temperature properties such as creep strength are of primary interest.

In LTHE scenarios, irradiation hardening is accompanied by loss of tensile ductility. To prevent failure, it is necessary to ensure that strain due to applied stresses during in-service conditions such as primary and secondary FW/B loading conditions do not exceed the remaining elongation of the material [61]. A major problem with all FM and RAFM steels is the severe loss of uniform elongation (UE) because of irradiation (see figure 6(a)). After ITER-TBM-relevant irradiation conditions, the UE measured at RT in Gen-I RAFM steels such as Eurofer97 or F82H is negligible (typically <1%), while some emerging advanced variants of Eurofer97 produced using non-standard manufacturing/processing routes perform only slightly better

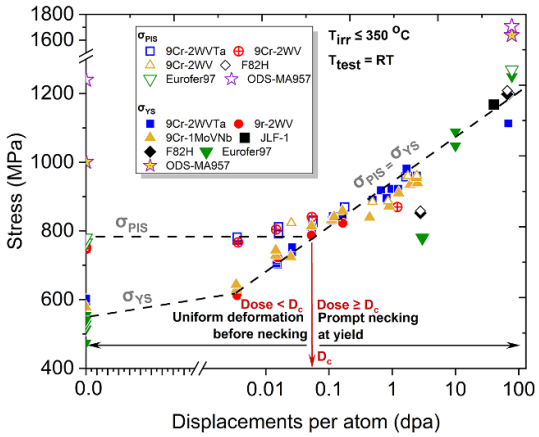

Figure 5. Plastic instability stress (σ_{PIS}) and yield stress (σ_{YS}) in neutron-irradiated RAFM, FM and ODS steels. Adapted from [152, 153] with additional RAFM and ODS data points added from [38, 45, 106, 135, 136].

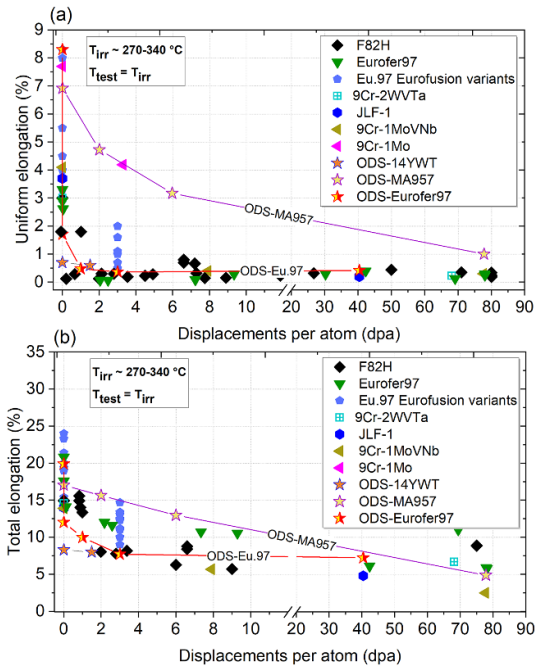

Figure 6. Loss of (a) uniform elongation and (b) total elongation of neutron irradiated RAFM steels compared with some conventional 9%Cr FM steels and certain 9%–14%Cr-based ODS steels for T_{irr} < 350 °C. Figure compiled using data from [5, 45, 70, 86, 122, 130, 135, 137, 140, 158].

[62, 66]. Matters are worse when test temperatures are higher because RAFM steels typically suffer from lower uniform tensile ductility at elevated test temperatures up to ∼500 °C–550 °C likely due to dynamic strain ageing (DSA) [154]. As a result, the UE reduces to even lower values when tensile tests are performed at component-relevant elevated temperatures [61, 66].

In general, the loss of UE due to LTHE when T_{irr} < 350 °C is very sharp with a drastic drop for doses as low as ∼0.1–0.5 dpa, and attains saturation at very low values (<1%) around ∼3–4 dpa (figure 6). While there are some uncertainties regarding the exact doses to attain saturation (including uncertainties as to what are the saturated UE values), and it is challenging to properly validate these values due to variations in irradiation temperatures and test temperatures between different studies, the overall tendency of RAFM steels is that the UE is almost non-existent when neutron irradiated in the severe LTHE regime (T_{irr} < ∼330 °C–350 °C). The total elongations and fracture strains remain high (⩾10%) after irradiations around ∼2.5–3 dpa, and typically saturate between ∼5%–10% by ∼10–12 dpa (figure 6(b)). From a power-plant design point of view such as the descriptions in ITER structural design criteria for in-vessel components [61, 155] or RCC-MRx, plastic flow localisation due to plastic instability in neutron irradiated RAFM steels is related to the loss of UE [156]—which presents the first failure mode, while ductility

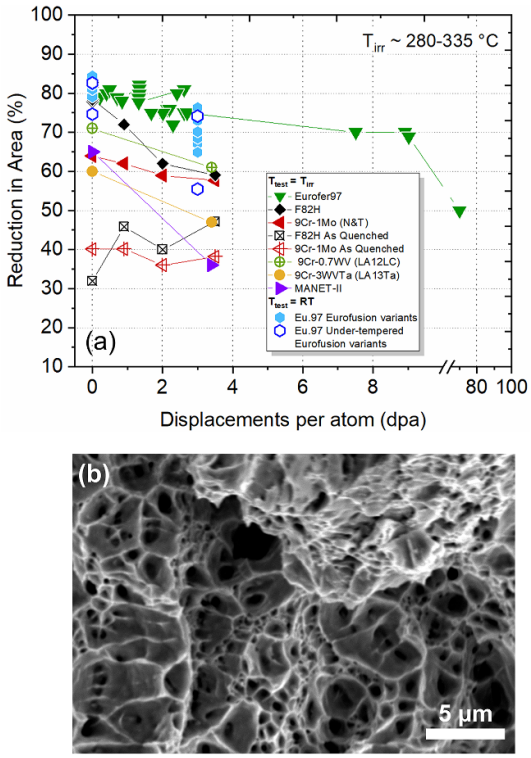

Figure 7. Necking deformation in neutron-irradiated RAFM and conventional FM steels. (a) RA eduction in area after neutron irradiation; data compiled from [41, 66, 110, 113, 130, 158]. (b) Scanning electron microscopy (SEM) results showing fully ductile fracture surface of Eurofer97 steel variant irradiated in HFIR to 2.94–3.24 dpa, $T_{irr} \sim 300 \pm 30$ °C.

exhaustion induced local fracture is the second mode of component failure that is linked to the loss of total elongation [61]. The second mode of deformation is typically not a major issue for Gen-I RAFM steels because they retain sufficiently high total elongations (⩾5%, see figure 6(b)), and tensile failures are largely ductile. However, failure due to immediate plastic flow localisation with almost non-existent UE is a concern for Gen-I RAFM steels [66, 152, 157]. It should be noted that the majority of RAFM steel irradiation data from European programmes originates from cylindrical gauge tensile samples [45, 94], while neutron irradiation programmes in the US and Japan have historically used miniature flat tensile geometries. The differences in sample geometries may affect the measured elongation values, and require some attention. From small specimen test technique studies, the differences between sheet and round tensile elongation values are reasonably comparable as long as pin- or shoulder-loaded specimen grips are used (clamped-end tab gripping should be avoided). The strength values estimated from miniature flat specimens and cylindrical specimens are robust and directly comparable.

2.2. Post-irradiation necking behaviour in LTHE regime in RAFM steels

Higher total elongations as compared to uniform plastic strain in neutron irradiated RAFM steels means the primary ductility remaining in the material is necking ductility. This is directly inferred from the reduction in area (RA) values that remain generally high, typically >65%–70% for doses up to ∼10 dpa, while values of >50% are reported for doses up to ∼70 dpa, when $T_{irr} \sim 300$ °C–330°C (figure 7(a)). Most tensile fractures are ductile cup-and-cone type (figure 7(b)). The post-necking strain and RA decreases due to irradiation as compared to non-irradiated RAFM steels, but this decrease is not as significant as compared to UE loss. Despite severe loss in UE, the sufficiently high necking ductility and ductile failures mean that calling RAFM steels 'embrittled' by only uniaxial tensile testing, as is often reported in the materials community, is technically incorrect in the absence of FT data. In other words, tensile tests measure hardening and loss of ductility but not embrittlement due to neutron irradiations (unless there is a clear proof of change in fracture mode to brittle fracture after irradiation). Figure 7(a) also shows that the RA of as-quenched FM or RAFM steels is typically much lower (less than 50%) as compared to normalised and tempered steels. Recent high flux isotope reactor irradiated (HFIR) results on Eurofer97 variants show that the RA of harder steels produced by under-tempering can also be quite low, with a substantial decrease in RA values by ∼3 dpa [66]. This further suggests that in the absence of high UE in RAFM steels, under-tempered RAFM varieties that are being tailored for improved high-temperature properties [3, 144] will perform poorly at low temperatures where LTHE is a concern.

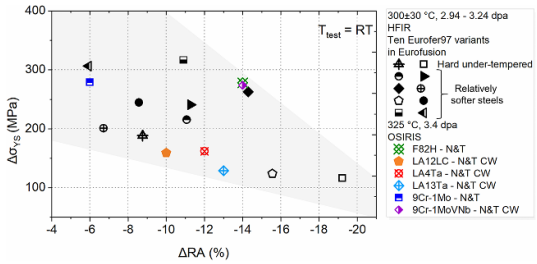

Figure 8. Irradiation hardening measured as increase in σ_{YS} plotted against loss in RA measured as the difference between RA of irradiated and non-irradiated samples of some low dose neutron irradiated RAFM and conventional FM steels. Reprinted from [66], copyright (2021), with permission from Elsevier.

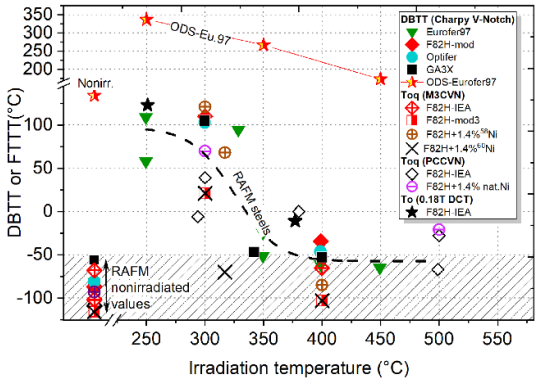

Figure 9. DBTT or FTTT of neutron irradiated RAFM and ODS-Eurofer97 steel, ~4–70 dpa. Data compiled from [94, 96, 100, 142, 159]. M3CVN = miniature 3-notch bend bar, PCCVN = pre-cracked Charpy V-notch, DCT = disc compact tension.

Low-dose (<3.5 dpa) neutron-irradiated FM and RAFM steel data compiled in [66] reported that hardening and loss in RA due to LTHE may be inversely correlated (figure 8). A similar trend is also speculated regarding loss in UE and loss in RA [66]. This is opposite to conventional wisdom and may imply that steels performing better after irradiation in terms of uniaxial properties (σ_{YS} and UE) may show a relatively poor performance for property changes relevant under triaxial stress states such as necking deformation. UE might be sensitive to material parameters that are different from those influencing RA after irradiation, even though both are measures of ductility. Historically, RA values are typically not compared with σ_{YS} and UE after irradiation because of the uniaxiality versus triaxiality argument. More experimental data points are needed to populate figure 8 and verify this speculation. In general, to complete the story of a materials' irradiated ductility, the UE, TE and RA values should all be reported because that might help better elaborate the key underlying mechanisms responsible for the loss of ductility under irradiation in this class of materials.

2.3. Irradiation embrittlement of RAFM steels

Due to the LTHE phenomenon, the DBTT measured using Charpy impact tests or fracture toughness transition temperatures (FTTT) measured using FT tests increase to higher values in RAFM steels (see figure 9), accompanied with a reduction in upper-shelf toughness [45, 70, 94, 116, 142]. For doses as low as ~2.5–3 dpa, a significant increase of DBTT or FTTT can occur (sometimes higher than RT for under-tempered steels) and tends to be much higher than RT for most RAFM steels for doses $\geqslant$~10 dpa. This embrittlement is most severe for $T_{irr} \leqslant$ ~330 °C–350 °C as shown in figure 9. With the increase in dose, the shift in DBTT increases sharply up to ~5–7 dpa and tends to saturate around ~15–20 dpa, which generally correlates well with saturation in hardening detected after tensile testing. For doses around ~30–35 dpa, DBTT shifts as high as ~200 °C can occur in RAFM steels. For $T_{irr} \sim$ 400 °C, the increase in DBTT is generally much smaller than 100 °C and almost no DBTT shift occurs for $T_{irr} \geqslant$ 450 °C–500 °C because of the relatively low density of irradiation-induced dislocation obstacles at elevated temperatures. Compared to conventional FM steels, the DBTT shift of irradiated RAFM steels is typically much lower, highlighting better FT properties of the clean reduced activation steel variants (figure 10). As an example, >70 dpa-irradiated T91 steel can show a DBTT shift as high as >300 °C [135], while the same for Eurofer97 or F82H remains much smaller [96]. RAFM steels also perform better compared to other Fe-based bcc

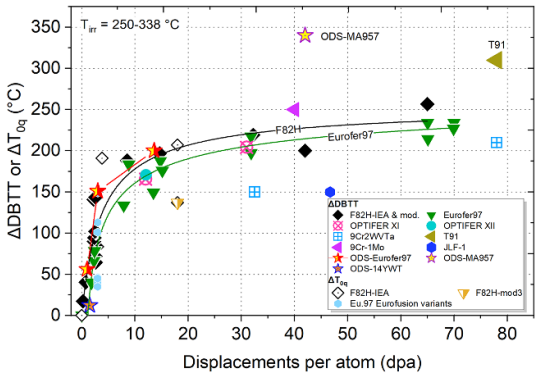

Figure 10. Irradiation embrittlement of RAFM, conventional FM and ODS steels shown as the shift in DBTT or FTTT with neutron dose. T_{oq} = Master Curve provisional reference FTTT. Data used from [63, 64, 94, 96, 135, 136, 142, 143, 160].

materials such as reactor pressure vessel (RPV) steels, which also suffer from well-known irradiation embrittlement [98]. Similar to RPV embrittlement scenarios, the shift in the DBTT or FTTT of RAFM steels correlates almost linearly with an increase in σ_{YS} or Vickers microhardness [64, 98, 159], suggesting as a first-order approximation that embrittlement resulting in poor FT is related to matrix hardening.

Differences between tensile tests showing largely ductile fracture surfaces while impact or FT testing showing embrittlement should be carefully and collectively analysed in irradiation experiments. During tensile tests, there is no stress concentrator initially (such as a notch) due to which the flow of a material is not constrained. As a result, the material has the margin to deform significantly until the true fracture stress limit is achieved. However, unlike in tensile tests, high stress concentration is already localised at the crack tip during FT testing. Therefore, the margin to reach fracture stress from the initial stress state is lower, resulting in much less deformation of a material (brittle fractures). Only performing tensile testing has the risk of incorrectly interpreting a material's failure mode as ductile when the same may fail by catastrophic brittle fracture in an irradiation environment. FT testing is particularly important because engineering materials and full-size components may often have imperfections that will stress concentrate under real loading conditions.

2.4. LTHE comparison: RAFM versus ODS steels

Literature on the mechanical properties of neutron-irradiated ODS steels is not as vast as for RAFM steels. With relatively limited data, it is still evident that ODS steels also suffer profusely from irradiation hardening and loss of tensile ductility (see figures 3 and 6). The susceptibility to LTHE of ODS steels is material dependent. Figure 3 shows that 9%Cr-based ODS-Eurofer97 hardens almost as much as Eurofer97 and other RAFM steels for doses <5 dpa but may harden significantly more than RAFM steels at high doses (>40 dpa) [86]. For 14%Cr-based MA957 (French INCO alloy), data up to ~40–80 dpa suggests comparable or slightly lower hardening as compared to the different RAFM steel varieties (figure 3—the extent of hardening seems slightly lower than Eurofer97 but comparable to F82H). Only low dose neutron data up to ~1.5 dpa exists for 14%Cr-based 14YWT alloy [143]. At such low doses, hardening in this material is very small (~30 MPa, figure 3) with almost no change reported in tensile ductility or FT, whereas Eurofer97 and ODS-Eurofer97 steels exhibited pronounced LTHE effects [143]. In the absence of medium to high dose neutron data, understanding of 14YWT's susceptibility to LTHE as a function of the neutron dose or T_{irr} is an open question. It is generally considered that radiation-induced hardening will be reduced in high sink strength materials such as ODS steels because the nano-dispersoids act as point-defect recombination sites that lower the overall defect supersaturation [50]. However, the data in figure 3 for both ODS-Eurofer97 and high sink strength ($>10^{16}$ m^{-2}) alloy MA957 shows that ODS steels can also harden significantly with values comparable to or higher than RAFM steels (depending on the alloy). The 14YWT alloy has a slightly higher sink strength than MA957, but within the same order of magnitude [50]. Therefore, quite likely this alloy may also behave in a qualitatively similar manner to MA957 with added neutron dose because both are designed based on a concentrated Fe–14%Cr matrix.

Recent results using Vickers microhardness indentation testing on several HFIR-irradiated ODS alloys suggest that significant radiation-induced hardening in this class of material can occur up to higher temperatures—T_{irr} > 400 °C–450 °C and maybe even up to 500 °C depending upon the material (see figure 11(a)). Data are plotted for 14%Cr-based MA957, 12%Cr-based 12YWT and 20%Cr–5.5%Al-based PM2000 that were irradiated between 300 °C–500 °C to the dose range of ~4.5–23.3 dpa. Compared to their

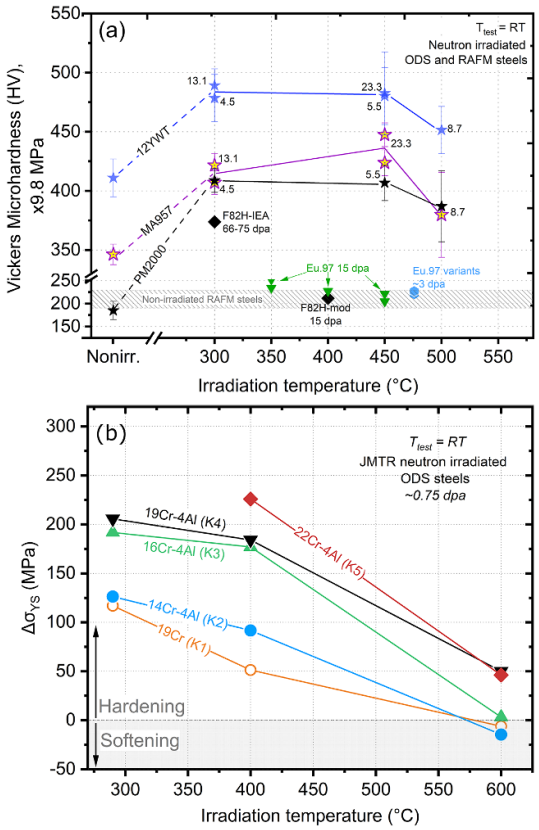

Figure 11. Irradiation hardening in ODS alloys. (a) Vickers microhardness after HFIR neutron irradiations at 300 °C–500 °C and 4.5–23.3 dpa. Results are reported for MA957 (INCO alloy), 12YWT (Kobelco) and PM2000 (Plansee) [163]. The dpa values are annotated in the figure. For comparison, hardness results from F82H-IEA, F82H-mod and Eurofer97 variants are overlaid. Adapted from [163] with RAFM data points added from [64, 163, 165]. (b) Increase in yield stress of several Fe–Cr and Fe–Cr–Al-based ODS steels developed in Japan after neutron irradiation in JMTR up to ∼0.75 dpa. Reprinted from [161], copyright (2007), with permission from Elsevier.

non-irradiated conditions, the hardness increased sharply for $T_{irr} = 300$ °C. However, no major recovery of irradiated hardness seems to occur in these steels for $T_{irr} = 450$ °C (figure 11(a)). For $T_{irr} = 500$ °C, some reduction in hardness occurs (especially for MA957), but the values remain higher than the non-irradiated matrix hardness of all three ODS steels. One of the well-known results of neutron irradiation-induced hardening in ODS steels was reported in Japan on a variety of Fe–Cr and Fe–Cr–Al-based alloys named as K1, K2, K3, K4 and K5 ODS alloys—after irradiations in the Japan Materials Test Reactor (JMTR) up to ∼0.75 dpa and $T_{irr} \sim 290$, 400 and 600 °C [161]. The increase in yield stress of the JMTR-irradiated materials after room temperature tensile testing are compiled from [161] in figure 11(b), where all the alloys showed hardening at 290 °C and 400 °C. The hardening behaviour was material dependent—higher hardening was reported in alloys with higher Cr concentration for the Fe–Cr–Al-based ODS steels. The data also showed some remnant hardening in 19%Cr–4%Al (K4) and 22%Cr–4%Al(K5) ODS alloys even at 600 °C. The authors concluded that while high-temperature hardening in the ODS steels was due to embrittling α' formation, Al addition increased the irradiation hardening (comparing K1 and K4 in figure 11(b)). The results of hardening at higher T_{irr} are qualitatively consistent between the five different ODS alloys irradiated in JMTR to low doses (0.75 dpa) and three ODS alloys irradiated in HFIR over a range of doses (4.5–23.3 dpa). Irradiation hardening at 400 °C is also reported in JOYO reactor irradiated ∼12%Cr ODS steels between ∼2.5–21 dpa [162]. The unexpected hardening of ODS steels in figure 11 for $T_{irr} > 350$ °C–400 °C is contrary to that in RAFM steels, where drastic recovery of radiation hardening occurs at higher temperatures and hardening almost completely subsides for $T_{irr} > 400$ °C–450 °C with a tendency for some slight softening for $T_{irr} >$ ∼450 °C–500 °C (see figure 2). This T_{irr}-dependent radiation hardening scenario of ODS steels requires careful further investigation to quantify the tensile and FT properties as a result of remnant hardening up to 500 °C. If radiation hardening of ODS steels up to ∼400 °C–500 °C poses a threat to the relevant engineering properties, then it is quite likely that the lower operating temperature limit of ODS steels (currently loosely taken as ∼350 °C based on RAFM steels data) may have to be increased to higher temperatures. Microstructural results exist that explain why ODS steels continue to harden up to such high temperatures; this is discussed in section 2.5.

In terms of post-irradiation tensile ductility, the UE and TE of ODS steels decrease with the dose; however, the behaviour is material-dependent as evident in figure 6. The ODS-Eurofer97 behaves almost identical to RAFM steels, where the UE reduces severely to values below ∼0.5%–1% for doses as low as ∼1 dpa. Thereafter, the UE saturates at the lower values and is almost non-existent. In MA957, irradiation data up to ∼6 dpa at 325 °C shows much higher post-irradiated UE values (∼between 3% and 6%) compared to RAFM steels [137]. But both RAFM steels and MA957 show a similarly poor UE (<1%) at higher neutron doses (>70 dpa); see figure 6(a). Figure 6(a) also shows that while RAFM steels and their tempered-martensitic 9%Cr ODS variants almost completely lose their capacity to uniformly deform very quickly (<1–2 dpa), fully ferritic ODS steels like MA957 lose the UE somewhat gradually. Therefore, despite radiation hardening of alloys like MA957, they still show superior tensile ductility compared to tempered martensitic RAFM steel variants or tempered martensitic ODS steel variants like ODS-Eurofer97. Between MA957 and ODS-Eurofer97, the difference in ductility may also originate from a variety of other reasons, including different chemistries, processing routes, grain microstructures (ferritic vs tempered martensitic) and different distributions of oxide particles. The irradiated tensile ductility of other alloys like 14YWT after high dose neutron irradiations remains to be quantified in the literature. It should, however, be explicitly noted that the most important property required for FW/B steel structures is FT because of the anticipated thick-walled nature of the components. For other envisaged applications of ODS steels, such as for thin-walled fast reactor cladding tubes, FT is not the primary requirement. Therefore, the higher tensile ductility of materials such as MA957 before and after neutron irradiation does not necessarily mean better properties for FW/B operations because the FT of ODS steels is generally worse compared to tempered martensitic FM steels (detailed below). In other words, a material can show vastly superior tensile ductility after neutron irradiation in terms of UE and TE values, but that does not directly imply that they have good FT; ODS steels like MA957 are a classic example of this behaviour. If relatively low FW/B temperature operations as detailed in figure 1 for fusion in-vessel components are unavoidable, future research should target developing ODS alloys with improved FT along with better tensile properties. One must note that FT is not necessarily linked to tensile ductility, but depends more on hardness (σ_{YS})—with a general tendency of most alloys typically showing poor FT for harder materials irrespective of their tensile ductility. It should also be noted that the elongation properties of ODS steels can be direction-dependent, with better properties measured along the extrusion direction while inferior properties in the other directions. Therefore, a full understanding of the tensile ductility reduction of ODS steels such as MA957 due to neutron irradiation require testing in both directions—which is unfortunately not the case for the data reported in the literature. For example, all MA957 tensile sample neutron irradiations in BOR60 [135, 136], OSIRIS [136, 137] and HFIR reactors [163] were performed on samples machined along the extrusion direction, implying the best case scenario for ductility. Another major difference between RAFM and different ODS steels is the inferior RA of the latter. While RAFM steels show high necking ductility with >80% RA in non-irradiated conditions and >50% RA remaining after doses as high as 70 dpa (figure 6(a)), the local necking deformation of ODS steels even in non-irradiated conditions is vastly inferior. As an example, the RA values of the well-known 14YWT alloy ranges between ∼15% and 25%, with the performance progressively worsening at higher temperatures between RT and 700 °C [164]. With the lack of neutron data, it is unclear how irradiations, specifically LTHE, may further worsen the necking behaviour in ODS steels.

ODS steels generally perform poorly in terms of impact or FT properties in non-irradiated conditions when compared to RAFM steels [94, 166], as also mentioned in the previous paragraph. As an example, Y_2O_3 particle addition in ODS-Eurofer97 worsens the DBTT and reduces the upper-shelf energy compared to reference Eurofer97. The FT of MA957 and early generations of 14YWT is also quite inferior [167–169]. In fact, the impact properties such as the DBTT of ODS steels in the non-irradiated condition have similar values to irradiated RAFM steels (see figure 9). Therefore, their applicability as thick-walled structures in nuclear environments where irradiation temperatures are lower than ∼400 °C (triggering LTHE) remains an open question. Improvements in non-irradiated FT have been recently demonstrated by processing optimisation for 14YWT alloy at ORNL [169]. This holds promise to develop toughness-improved ODS steels, but such alloys require neutron irradiation testing to validate their performance. The literature suggests the upper-shelf energy of Fe–Cr-based bcc steels scales linearly with the RA [158], so poor necking of ODS alloys during tensile testing is likely an indirect indicator of their poor impact or toughness properties. After neutron irradiation, properties are material dependent. Low-dose, ∼1.5 dpa/300 °C HFIR irradiations on 14YWT show no appreciable effect on FT measured using three-point bending [143]. Systematic higherdose data are needed for this alloy to confirm the behaviour. Results on ODS-Eurofer97 show a large increase in DBTT due to neutron irradiation (∼16–17 dpa, T_{irr} < 350 °C [94]), and the DBTT reduces progressively with T_{irr} up to 450 °C—however, it never fully recovers to the non-irradiated values as seen in figure 9. This is different from the behaviour of RAFM steels where no major DBTT shift occurs for T_{irr} > 350 °C–400 °C. Regarding MA957, the ∼40 dpa irradiation data in figure 10 shows an extremely high

DBTT shift (∼350 °C) due to neutron irradiation as compared to the ∼200 °C–225 °C DBTT shift for RAFM steels like F82H or Eurofer97 when exposed to similar doses—further confirming that ODS steels are not immune to LTHE and, depending upon the alloy system, their fast fracture performance degradation under neutron irradiation can be worse than that of RAFM steels. It should be noted that the database of neutron irradiated properties of ODS steels is still much smaller as compared to RAFM steels, and ODS steels are typically much more complex, consisting of widely varying chemistries and microstructures as compared to ∼8%–9% Cr-based RAFM steels. For a better understanding and quantification of LTHE in ODS steels more systematic future neutron irradiation experiments and data collection is needed to fully map the susceptibility of different ODS steel types to the important issue of LTHE and benchmark against the well-known results in RAFM steels.

2.5. Potential causes of LTHE

As evidenced in the earlier subsections, there are many aspects to the LTHE problem. The primary first-order aspects are the following: (a) increase in hardness and σ_{YS}, (b) loss of tensile ductility (most affected is UE), (c) deterioration of local necking deformation (but not quite as much as UE), (d) worsening of impact properties evidenced by increase in DBTT and reduction in upper-shelf energy, and (e) loss of FT. Each of these properties is inter-related. But despite decades of research, there is no full consensus on the true origins of hardening-embrittlement, not only for RAFM/ODS steels, but also for other materials such as RPV steels. From the analysis of tensile tests on conventional FM and RAFM steels and microstructural analysis on deformed samples it appears that plastic instabilities due to irradiation cause flow localisation (deformation channeling) [170, 171], and this is the reason for the loss of UE. However, tensile results analysed on true stress–true strain units suggest that the primary effect of irradiation is to partially exhaust the strain-hardening capacity of a material [152, 153, 172], resulting in higher strength and lower ductility until failure, while the true fracture stresses remain somewhat unaffected (until drastic embrittlement occurs when $\sigma_{PIS} = \sigma_{YS}$) [153]; see figure 5. This inference is strengthened from observations that the true stress–true strain curves of irradiated FM steels overlap with the non-irradiated curves, but are displaced to the right [153]. Which phenomenon is the dominant mechanism is an open question. From a mechanistic point of view, microstructural features that obstruct dislocation glide motion will cause hardening, and the harder matrix then results in lower ductility. Based on this argument, the hardening component of LTHE in RAFM steels is historically attributed to dislocation loops [173]; see figure 12(a). However, irradiation-induced solute nanoclustering can play a tremendous role in hardening in Fe–Cr-based conventional FM and RAFM steels that should not be ignored. As an example, results from irradiated binary Fe–Cr alloys show that impurities such as Ni, Si, P that form Cr-NiSiP co-clusters under irradiation can further contribute to the σ_{YS} increase [174–176]. The formation of CrMn-rich clusters around dislocation loops coupled with co-segregation of Si and P was shown to drastically increase the σ_{YS} of Eurofer97 neutron irradiated from ∼15–32 dpa at 300 °C–330 °C [177] (see figure 12(b)). Similarly, F82H-IEA steel also showed enhanced hardening due to irradiation-induced heterogeneous co-clustering of Mn and Si on dislocation lines/loops after HFIR neutron irradiations to ∼4.5 dpa at 300 °C (figure 12(a)) [178]. Interestingly, no Cr-rich clustering was detected in F82H compared to the high-dose Eurofer97 data, so it remains to be seen at what dose Cr starts to enter such clusters. Mn–Si–Ni-rich solute nanoclustering was also recently reported in neutron-irradiated 9Cr–1MoVNb steels [179]. The formation mechanisms of such solute nanoclustering of minor alloying or impurity elements are in the early stages of exploration for RAFM steels, but judging by the Eurofer97 and F82H results in figure 12 it is evident that Mn is a key element. The role of Mn in the formation of deleterious embrittling phases has been studied even in RPV steels for decades [180–183]. In addition to Mn–Si–Ni–P-rich clustering, the segregation of Cr to dislocation loops is experimentally known to occur in bcc Fe–Cr-based steels, which is also expected to contribute to additional hardening in these materials [184, 185].

Regarding ODS steels, these alloys are primarily high Cr concentration (∼9–20 wt.%)-based materials and contain numerous other elements in varying proportions [169, 186–190]. In the non-irradiated condition, ODS alloys typically consist of a high density of ultra-fine nano-dispersoids in the matrix (figure 13(a)) owing to Y_2O_3 particle addition during ball milling. After irradiation, dislocation loops are known to form in ODS steels that will cause hardening (figure 13(b)). The dislocation loops can often be irregularly shaped because of the presence of hard nano-dispersoids [186], highlighting that nano-dispersoids may affect the growth of loops by acting as pinning points. For ODS steels with >10% Cr, the most important factor in the temperature range of fusion blanket operations is the formation of Cr-rich embrittling α' precipitates under thermal ageing (well-known 475 °C embrittlement) or neutron irradiation; see figure 13(c) [191–199]. The radiation-enhanced α' formation is the main reason for the significant LTHE detected in the ODS steels for Cr $\geqslant$ 12% in the 300 °C–500 °C temperature range [194, 196–198, 200, 201]. For HFIR irradiated MA957, evidence of α' at both 300 and 450 °C is provided in figure 13c and d using

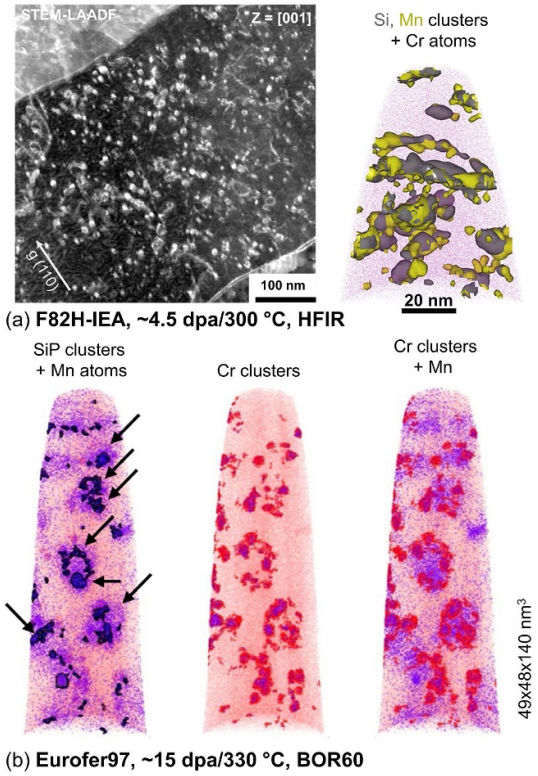

Figure 12. Neutron irradiation induced dislocation loops and radiation-induced/enhanced solute nanoclustering in RAFM steels that can contribute to hardening. (a) Low angle annular dark field STEM image of dislocation loops and atom probe iso-concentration analysis showing Mn–Si co-clustering on dislocation lines/loops in F82H-IEA steel irradiated in HFIR to ∼4.5 dpa at 300 °C, adapted from [178]. (b) Atom probe iso-concentration analysis showing CrMnSiP-rich co-clustering in Eurofer97 irradiated in BOR60 to ∼15 dpa at 300 °C. Reprinted from [177], copyright (2020), with permission from Elsevier.

multivariate statistical analysis (MVSA) of high-throughput scanning transmission electron microscopy (STEM)-energy dispersive x-ray spectroscopy (EDX) data and by atom probe tomography (APT). Moreover, α'-induced hardening and embrittlement is also reported for the JMTR-irradiated ODS alloys by Cho *et al* [161] and Oh *et al* [201]. The observed increase in hardening with increasing Cr concentration of the JMTR-irradiated ODS steels is also likely linked to α' because a higher α' formation is expected with an increase in Cr concentration; for Cr concentrations as high as 16%, 19% and 22% used in JMTR experiments, α' will form even at higher temperatures greater than 500 °C because such alloys will be inside the miscibility gap of the Fe–Cr phase diagram [202, 203]. Radiation-enhanced α' formation is also reported for fast flux test facility (FFTF) irradiated MA957 (412 °C, 109 dpa) [204], Phénix fast reactor irradiated MA957 (412 °C, 50 dpa and 430 °C, 75 dpa) [194], and α'-induced hardening and embrittlement is reported for Phénix irradiated 13%Cr-based DY ODS steel (∼13%Cr–1.5%Mo–2.03%Ti–0.45%Y–0.3% O–0.05%Al) [196, 205, 206]. This is a well-known challenge in concentrated Fe–Cr-based alloys [207], and causes overall uncertainties in the thermo-mechanical property resilience of ODS steels for a fusion FW/B. In addition to α', the experimental results also show irradiation-induced/enhanced solute nanoclustering and formation of other embrittling phases of different elemental species in ODS alloys after neutron irradiation. For example, Phénix fast reactor irradiations on 13%Cr ODS steels showed embrittling intermetallic χ phase (70%Fe–15%Cr–7%Ti–6%Mo) [196, 206, 208] formation. HFIR irradiated MA957 shows extensive clustering of Ni–Ti-rich phases due to neutron irradiation (figure 13(c)), whichis also expected to worsen LTHE.

For Fe–Cr–Al-based ODS steels, while α' embrittlement remains an issue, there is growing evidence of irradiation-induced or irradiation-enhanced formation of different phases that may also worsen the LTHE scenario; e.g. PM2000 alloy was shown to suffer from a homogeneous clustering of an Al–Ti-rich phase when neutron irradiated in HFIR to >50 dpa/300 °C and 4.5–8.7 dpa/$T_{irr} \geqslant$ 450 °C–500 °C [197, 209]. Moreover, Cho *et al* [161] concluded that adding Al increased irradiation hardening, which could be due to a similar phenomenon as reported for PM2000. In fact, the Fe–Cr–Al–Ti system is known to form an Al–Ti-rich β' phase upon thermal ageing [210, 211]. It is quite likely that such phase formation is accelerated under irradiation that may lead to observations such as those made recently in HFIR irradiated PM2000 [197, 209]. While α' precipitation is relatively well understood under neutron irradiation conditions, a proper

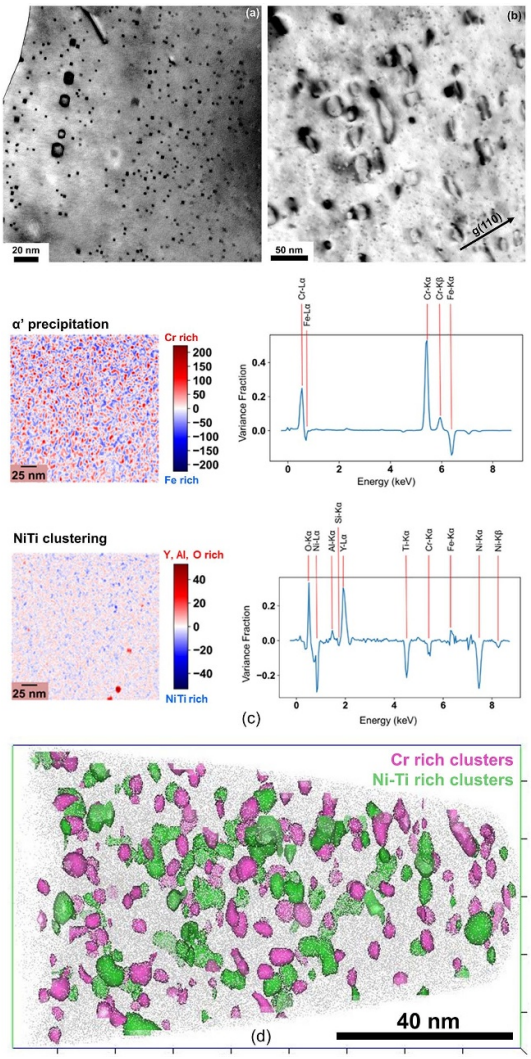

Figure 13. (a) Down axis bright-field TEM image of oxide nano-dispersoids in a 14%Cr-ODS steel (14%Cr–1%W–0.4%Ti–0.3%Y_2O_3) from CEA and (b) dislocation loops in the same ODS alloy after self-ion irradiation to ∼5 dpa at 450 °C; adapted from [214, 215]. (c) α' precipitation and NiTi co-clustering in 14%Cr MA957 (INCO alloy) neutronirradiated in HFIR to >50 dpa/300 °C, revealed using MVSA on high-throughput STEM-EDX maps; adapted from [197]. Iso-concentration analysis of APT data showing Cr-rich clusters (expected to be α') and NiTi co-clustering in MA957 neutron-irradiated in HFIR to 5.5 dpa/450 °C; adapted from [200]. The iso-concentration thresholds were Cr > 25 at.% and Ni > 2 at.% [200].

quantification of phase instabilities and microchemical phenomena related to other alloying elements is presently not fully detailed in the literature for ODS steels—this needs to be understood in order to explain LTHE in ODS steels. Presently, the combined effect of irradiation-induced/enhanced phase instabilities such as α', Ni–Ti and Al–Ti clustering is considered as a potential reason for the higher hardening detected in a few HFIR irradiated ODS alloys in figure 11(a) [197, 212]. Therefore, it appears that the extra hardening effects that seem to occur in many of the ODS steels are associated with specific solute additions. Further work is needed to evaluate preferable solute concentrations that suppress hardening at temperatures >350 °C. To minimise the deleterious effects of α–α' unmixing, lower Cr concentrations (∼8–10 wt.%) in ODS steels for fusion applications are desirable, such as in ODS-Eurofer97 designed in Europe and the recently developed 10%Cr-based M4/M5 ODS alloys designed at ORNL [213]. These alloys also require careful chemistry tuning to minimise the concentration of elements that may cluster under irradiation and enhance hardening embrittlement (like Ni–Mn–Si or Al–Ti).

In addition to solute nanoclustering, the stability of the oxide nano-dispersoids in ODS steels under irradiation is critical to ensure a satisfactory performance is maintained for in-service conditions including LTHE resilience and other important properties of ODS steels such as cavity-swelling resistance and high-temperature properties. Because oxide particles act as point-defect sinks, any changes to the nano-dispersoid microstructure will affect the overall radiation tolerance of the alloy in the entire operating temperature range for FW/B structures. The oxide particle stability, recently reviewed in [216], has been

extensively researched using neutrons [194, 196, 199, 204, 205, 217–230], ions [219, 231–260] and electron irradiations [261, 262] in a variety of ODS steels. Extensive ion irradiation literature exists on a wide range of ODS steels where nano-dispersoids are reported to be stable over the irradiation temperature and dose ranges of RT–835 °C and ion doses from ∼2 to 200 dpa [205, 233, 234, 237, 240, 243, 247–249, 251, 259, 263]. However, substantial literature also exists over a similar ion irradiation temperature and dose range, where deterioration of the oxide particles is reported [205, 219, 222, 226, 231, 235, 238, 239, 241, 242, 245, 250, 257, 261, 262, 264, 265]. The majority of these reports typically show changes in the size or number density of the nano-dispersoids, while irradiations in the temperature range of RT–400 °C have also shown radiation-induced amorphisation (RIA) of the oxide particles in many ODS steels [196, 229, 235, 243, 251, 261, 264]. This includes RIA near RT of oxide particles in MA957 [243], ODS-Eurofer97 [251], 18%Cr-ODS [264] and electronic stopping power-induced amorphisation of oxides in DY ODS steels [235], while RIA using heavy ions at higher temperatures (⩾400 °C) of nano-dispersoids is reported in EM10-ODS [205] and DY ODS steels [196, 205]. Dissolution of the nano-dispersoids under cascade damage conditions due to ballistic effects is also known, especially at lower temperatures, as seen in the results from cryogenic irradiations of 14YWT [226].

For fusion in-vessel applications, the stability of the nano-dispersoids under neutron irradiations, instead of ion irradiations, is of primary interest. Specifically under neutron irradiations, there is evidence of noteworthy structural deterioration and chemical changes occurring in nano-dispersoids in many ODS steels [196, 199, 205, 208, 217, 220–222, 224, 228, 266]. For example, fast reactor irradiations as fuel pin claddings in Phénix of 13%Cr DY ODS steel between 532 °C–580 °C 30.5–78.8 dpa showed dissolution and then reprecipitation of the oxides, leading to the formation of a halo of smaller oxides around the larger ones and a disappearance of the initially homogeneous distribution of oxides that were smaller than ∼20 nm in diameter (see figures 14(a)–(c)) [196, 205]. The authors further reported that the matrix–oxide interface upon irradiation became irregular [205]. Moreover, there was Al, Ti and Y loss from the nano-dispersoids due to irradiation, with greater loss of Al, then Ti and then Y [196, 205]. Microstructure examination of >50 dpa/300 °C HFIR-irradiated PM2000 steel shows complex structural-chemical transformations occurring within the particles—including the development of internal cavities and semi-amorphous transformation of the particles with distinct embedded crystalline islands (see figure 14(d) and [200, 224, 266]). The crystalline islands, visible as regions of relatively bright contrast in Z-sensitive high-angle annular dark-field STEM imaging, are likely distinct in chemistry as compared to the rest of the oxide particles [197, 209]. ODS-Eurofer97 has also shown formation of internal cavities along with complete amorphisation of the nano-dispersoids after fast neutron irradiations in the BOR-60 reactor at 250, 350 and 450 °C up to 16.2 dpa, reported by Klimenkov *et al* [221], thereby suggesting qualitatively similar observations between relatively coarse oxides of PM2000 versus relatively finer oxides in ODS-Eurofer97. Moreover, APT results from Rogozhkin *et al* on BOR-60-irradiated ODS-Eurofer97 (330 °C, 32 dpa) also show chemical changes in the nano-dispersoids due to irradiation—chemistry of the particles evolves by loss of V and progressive increase of Y concentration hypothesised due to dissolution of particles >10 nm in diameter [222, 228]. Structural deterioration including formation of internal cavities in the nano-dispersoids is known for neutronirradiated MA956 (328 °C, 4.36 dpa) [199]. Neutron irradiation-induced oxide particle stability was also studied in MA957 after irradiations in multiple reactors such as Phénix in France [194, 195, 218], JOYO in Japan [220], and FFTF and HFIR in the US [204, 230], while new microstructural studies are ongoing for MA957 irradiated in HFIR [197, 209]. The results are mixed. The JOYO irradiations were performed at higher temperatures between 502 °C and 709 °C, up to ∼100 dpa; this resulted in a number density reduction by about half of the non-irradiated particle density, claimed to be due to ballistic dissolution of the nano-dispersoids due to displacement cascades [220]. The authors also reported a progressive increase in the average size of the nano-dispersoids, collectively indicating significant changes to the nano-dispersoid microstructure. But HFIR irradiations at low doses of ∼3 dpa/600 °C, characterised using APT, did not suggest a major change in the particle size and density [230]. A Phénix irradiation study on MA957 at relatively lower temperatures (412 °C, 50 dpa and 430 °C, up to 75 dpa) also showed a slight decrease in the oxide nano-dispersoid number density but not much coarsening—likely due to the lower temperatures where disordering due to cascade effects may be more pronounced as compared to at higher temperatures. The entire collection of Phénix irradiated MA957 results analysed using analytical transmission electron microscopy (TEM) suggests that different oxides in the alloy are likely behaving differently—more severe dissolution of the coarse Ti-rich oxide particles was reported as compared to the (Y, Ti, O)-rich particles [194]. For FFTF irradiated MA957 (412 °C, 550 °C, 670 °C, 109–113 dpa), the results are opposite to the JOYO and Phénix data. At 412 °C, the authors reported a significant increase in the nano-dispersoid number density measured by APT analysis, postulated to be due to ballistic dissolution of

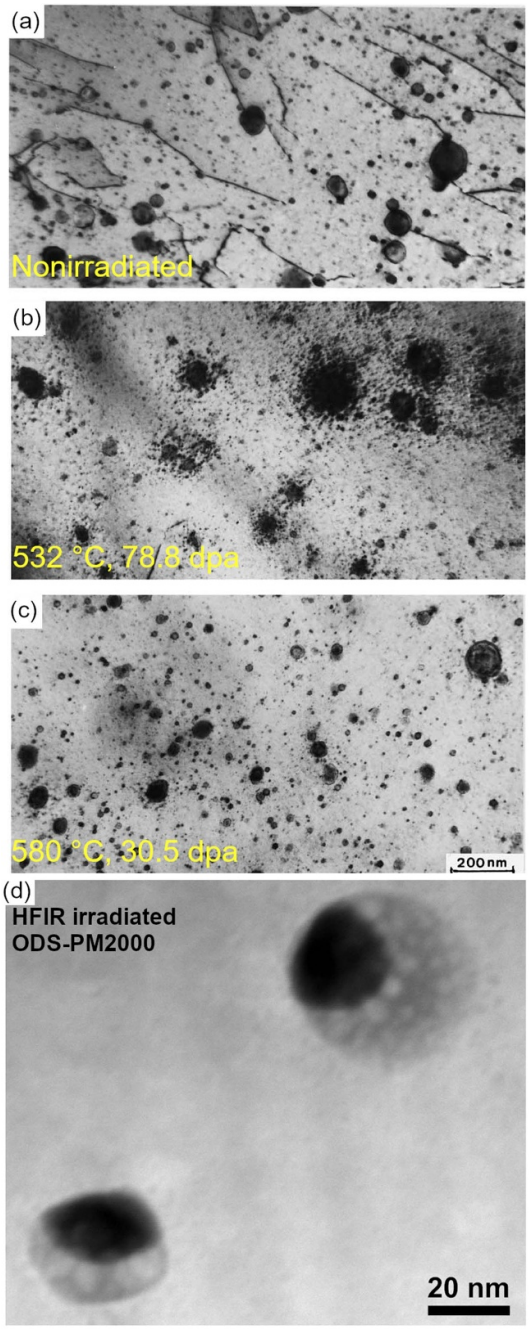

Figure 14. Structural and chemical transformation of oxide nano-dispersoids in ODS steels by neutron irradiation. (a)–(c) TEM images showing deterioration of oxides in DY ODS steel versus non-irradiated condition after fast neutron irradiation in Phénix reactor— [196], reprinted from [205], copyright (2004), with permission from Elsevier. (d) Z-sensitive high-angle annular dark field STEM image of nano-dispersoids in a PM2000 alloy irradiated in HFIR to >50 dpa at 300 °C. Dark contrast is internal cavities, while adjacent semi-amorphous regions within crystalline areas are visible as bright spotty regions. Different chemistries were reported for crystalline versus amorphous regions [224, 266].

the larger nano-dispersoids caused by displacement cascades [204]. At the higher irradiation temperatures, the nano-dispersoid density remained similar to the non-irradiated values, indicating a lesser contribution of ballistic effects [204]. Some of these discrepancies are likely due to the fact that different characterisation techniques are used for analysis, such as APT, conventional TEM, analytical STEM or high-resolution TEM, and each has its own advantages and limitations. Therefore, a combination of all these techniques is perhaps the best way forward to better understand how nano-dispersoids behave under irradiation. Nevertheless, the collection of data from the literature presented above points to the fact that nano-dispersoids in different ODS alloys can suffer from significant damage due to neutron irradiations in the entire temperature range of the envisaged FW/B operations. Such modifications of the nano-dispersoid microstructures will worsen the

overall radiation tolerance of ODS steels, including worsening LTHE, as previously discussed by Monnet *et al* [196, 205]. Future research is required to quantify a link between the degradation of the oxide nano-dispersoids and LTHE scenarios in fusion-specific ODS steel designs.

3. The effect of helium

Uncertainties regarding the potential synergistic effects of He with displacement damage on the performance degradation of fusion in-vessel components is a critical issue facing the development of FW/B structures. The high He generation rate envisaged in RAFM steels by D-T 14 MeV neutrons was the primary motivation to propose the International Fusion Materials Irradiation Facility (IFMIF), and a similar motivation is echoed for the Fusion Prototypic Neutron Source (FPNS) being planned in the US [267, 268]. Efficient management of He in steels to minimise its deleterious effect on microstructural evolution and mechanical property degradation may be achieved by incorporating high sink densities in high-performance alloys [50, 190, 269, 270] as compared to Gen-I RAFM steels. However, a fundamental understanding of the effect of He on the thermo-mechanical properties of RAFM steels over the entire temperature range of FW/B operations is not fully clear, while negligible neutron irradiation data on He effects in ODS steels currently exists. Specifically for RAFM steels, debate still exists on the deleterious effect of He on fast fracture properties (measured using tensile, Charpy and FT testing) relevant for water-cooled blanket designs, while very little research is available on the effect of He on high-temperature deformation/creep behaviour in RAFM steels that is relevant for He or dual-cooled blanket designs. Further, the effect of He on cavity swelling in the intermediate temperature range under fusion-relevant neutron irradiation conditions is also uncertain. The main reason for this is the lack of He generation in RAFM steels when irradiated by fission neutrons in materials test reactors (MTRs)—only ∼0.1–0.5 appm He dpa^{-1}. In the next sections, the challenges and strategies to obtain fusion-relevant He/dpa ratios for neutron irradiations are discussed along with the current understanding of the effect of He on hardening and embrittlement.

3.1. Challenges to obtain fusionrelevant He/dpa ratios in RAFM steels

In the absence of IFMIF or FPNS, simulating fusion-relevant He generation and obtaining the bulk mechanical properties from RAFM steels require irradiations either in spallation proton-neutron (SPN) facilities or using isotopic tailoring of steels with elements that have a high (n, α) reaction cross-section in the fission neutron spectrum such as for ^{10}B, ^{58}Ni and ^{54}Fe [271–273]. The coating of steels with He-producing elements such as Ni-rich injector foils/coatings is also efficient in producing He in MTR irradiations [274]. These methods have their specific advantages and disadvantages. For the injector foils/coatings method, He generation is limited to a few μm thick regions with no access to bulk properties (similar to ion irradiations). For SPN facilities, high doses are achievable. But the He generation rates are much higher than fusion (see figure 15). Furthermore, for certain early SPN irradiations such as STIP-I, obtaining constant temperature irradiations with a high beam current was challenging, and beam trips are known to occur that can cause temperature excursions during irradiations [86]. Another recently discovered issue is the formation of transmutation-induced solid spallation products in RAFM steels, revealed by atom probe analysis, that actively modify the microstructural evolution [275]. The potential effect of spallation products on the degradation of mechanical properties currently remains unaccounted for.

For the isotopic doping technique, ^{54}Fe isotope has the advantage of not modifying the chemistry of the alloys. However, ^{54}Fe is a very expensive isotope with costs typically ranging from $5000–$10 000 per gram. Moreover, the achievable He/dpa ratios are limited to ∼2–2.3 appm He dpa^{-1} in high-flux reactors (figure 15). Doping with boron can produce high He/dpa ratios in MTR irradiations and comparing ^{10}B and ^{11}B can isolate the effect of He from the effects of chemistry modification [85]. However, the very high (n, α) reaction cross-section of ^{10}B means rapid burn-up of the isotope in the first few days at the beginning of the cycle of neutron irradiations, which initially causes a very high He generation rate [276]. Boron also tends to segregate heavily at grain boundaries, due to which He generation is not homogeneous in the material [271]. Moreover, compared to reference RAFM steels, the addition of boron can significantly modify the steel microstructures due to the formation of coarse (Fe,Cr)B-rich precipitates [7, 85]. Further, extra dpa from ^{7}Li recoils needs to be considered and, depending upon the initial ^{10}B concentration, this added dpa may not be negligible [276, 277]. The addition of Ni to RAFM steels also stimulates He generation during MTR irradiations [273]. A major advantage is the possibility to obtain a wide range of He/dpa ratios by carefully tuning the ratio of ^{58}Ni/^{60}Ni in the material for a fixed total Ni concentration (figure 15). It must be noted that RAFM steels do not contain much Ni or B. Adding these elements to the steels affects their metallurgical properties. Therefore, neutron irradiations using isotopic tailoring must always be performed on steels doped with identical chemical elements with two distinct isotopes—one producing He (^{58}Ni, ^{10}B) and the other not producing much He (^{60}Ni, ^{11}B). This is necessary to isolate the effect of chemistry modification on

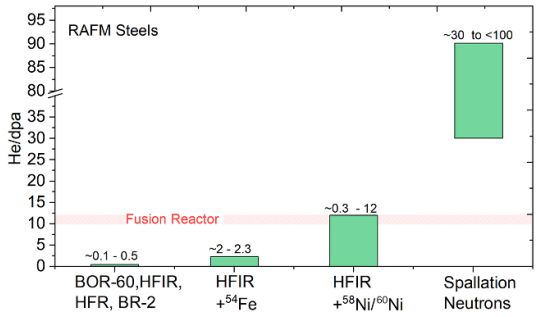

Figure 15. He/dpa ratios achievable in RAFM steels with different neutron irradiation facilities and isotope doping conditions. For ^{58}Ni/^{60}Ni addition, calculations are performed for a fixed total Ni concentration of ∼1.2–1.4 wt.% and progressively changing the ratio of the two isotopes. The ^{54}Fe and SPN data adapted from [271, 278].

the irradiated properties. A direct comparison of chemically modified isotopically tailored RAFM steel to non-chemically modified steel is not recommended.

Especially for the Ni doping technique, the total Ni concentration should be kept lower than ∼1.5–2 wt.%. Changes in the mechanical properties like the hardness and σ_{YS} of RAFM steels may occur even for [Ni] $\geqslant$ 0.5 wt.% [7]. Moreover, Ni is an austenite stabiliser, which lowers the ferrite to austenite transformation temperatures (Ae1 and Ae3 temperatures). If too much Ni is added ($\geqslant$1.2–1.5 wt.%), the typical tempering treatment temperatures of 750 °C–760 °C risk lying in the dual-phase austenite + ferrite region, which upon cooling risks producing untempered martensite [100, 279]. Therefore, if a direct comparison with Ni-doped and non-Ni-doped RAFM steels is sought, Ni concentrations more than $\geqslant$0.5 wt.% are discouraged. This will limit the total He generation rate achievable in steels. For higher Ni contents to obtain higher He/dpa ratios, the results should compare data between ^{58}Ni and ^{60} Ni-based steels and not with non-Niadded RAFM steels. A summary of the advantages and disadvantages of the different He generation methods for neutron and ion irradiations is given in table 1.

3.2. The effect of He on LTHE

Helium stabilises cavities/bubbles in the microstructure, which act as obstacles to the dislocation glide [280]. As a result, He may deleteriously affect LTHE. The effect of He on the irradiated tensile properties, impact properties and FT has been studied in RAFM steels doped with ^{10}B, ^{58}Ni, ^{54}Fe, and using SPN facilities [85, 86, 99, 100, 115, 281–283]. Because SPN irradiations do not require chemistry modification of RAFM steels, historically these data points have been the primary basis for our current understanding of the effect of He. For $T_{irr} \leqslant$ 350 °C, comparing SPN irradiations (up to 20 dpa, 1800 appm He, EM10 alloy) with fission MTR data suggests no saturation in hardening at ∼20 dpa in SPN-irradiated FM steels, while the behaviour is similar at lower doses ($\leqslant$10 dpa) (see figure 3). At around 20 dpa, the increase in σ_{YS} for SPN-irradiated FM steels can be as high as >700 MPa [86, 283]. The SPN results also show that hardening extends to higher irradiation temperatures ($\geqslant$350 °C–400 °C) where conventional RAFM steels typically do not show much LTHE after MTR irradiations [101]; see figure 16. This additional hardening after ∼10 dpa has been attributed to the effect of He-induced bubbles [65, 85]. Between ∼10–18 dpa and ∼750–1300 appm He, SPN irradiations also show almost no tensile ductility in RAFM steels with brittle intergranular fracture occurring, sometimes even before the σ_{YS} [101, 283]. A separate set of SPN irradiations for T_{irr} ∼140 °C–360 °C and doses up to 20 dpa and ∼1800 appm He on other 9%Cr steels such as EM10 and Grade91 also show significant hardening when tensile tests are performed at RT and >250 °C, accompanied with severe loss of ductility and fully brittle failures after ∼15–16 dpa [86].

MTR irradiations on ^{54}Fe-based F82H steel do not show a clear effect of ∼2–2.3 appm He dpa^{-1} generation rate on the irradiated tensile properties after ∼34 dpa at 300 °C [115]. Recent results on HFIR irradiated ORNL-9Cr-2WVTa alloy showed a higher σ_{YS} increase of up to ∼160 MPa in ^{58}Ni-doped samples (228 appm He, 9.5 appm He dpa^{-1}) compared to ^{60}Ni-doped samples (7 appm He, 0.03 appm He dpa^{-1}) when irradiated to ∼24 dpa at 300 °C ($T_{test} = T_{irr}$) [99]; see figure 16. This result questions the validity of a previous hypothesis suggesting irradiation hardening due to He is minimal below ∼500 appm He for T_{irr} < 400 °C based primarily on spallation data or high-energy He implantation data [85]. What is interesting is that the ^{58}Ni/^{60}Ni-doped ORNL-9Cr-1WVTa data do not show much change in tensile ductility due to He and neither shows a major effect of He on the tensile properties at a high T_{irr} of 400 °C [99], which is the opposite to the SPN data where He-induced hardening extends to higher temperatures (although He concentrations are higher); see figure 16. More experiments, especially MTR-based irradiations on

Table 1. Advantages/disadvantages of different He generation methods in RAFM steels under irradiation.

Type	Technique	He/dpa	Advantages	Disadvantages
Spallation neutrons	Spallation proton-neutron source	∼30 to <100	• High doses • High He generation rate	• He/dpa much higher than fusion • Poor temperature control due to very intense beam and beam instabilities • Solid spallation products that actively participate in microstructural development
Neutron irradiations in MTRs	^{54}Fe doping	∼2–2.3 ^{54}Fe$(n,\alpha)^{51}$Cr	• No major chemical effects • Homogeneous He generation	• Very high isotope cost • Low He/dpa
	^{10}B/^{11}B addition	Up to 10–12 ^{10}B$(n,\alpha)^{7}$Li	• High He generation rate • Inexpensive	• Nearly insoluble in steels • Segregates to grain boundaries—heterogeneous He generation • Non-negligible chemical effects: modification of metallurgical properties
	^{58}Ni/^{60}Ni addition	∼0.3 to >10 ^{58}Ni(n,γ) ^{59}Ni(n,α) ^{56}Fe	• Wide range of He/dpa ratios achievable by tuning isotopic ratio • More homogeneous distribution compared to B addition • Slow burn-up rate compared to B	• Can segregate to grain boundaries • Non-negligible chemical effects • More than ∼1.5%–2% Ni addition drastically changes steel's properties • Ni-induced enhanced hardening due to Ni-rich solute nanoclustering
	Ni-based injector foils/coatings	∼0.3 to >10 ^{58}Ni(n,γ) ^{59}Ni(n,α) ^{56}Fe	• Wide range of He/dpa ratios achievable • Homogeneous distribution of He • Chemistry modification of steels is not required	• He implantations limited to a few μm thick near-surface regions • Bulk properties inaccessible • Ballistic mixing of the coating-steel interface under cascade damage condition is not fully evaluated
Single/dual-beam ion irradiations	Implantation with accelerators	0 to >100	• Wide range of He/dpa ratios available • Relatively cheap • Good control over temperature and irradiation parameters • High doses achievable in reasonable time	• Very shallow irradiation depths • Bulk thermo-mechanical properties inaccessible • Inhomogeneous damage profile • Strong surface effect and injection ion artefacts • Major effect of high dose rate on microstructure evolution, including ballistic dissolution of precipitates/second-phase particles

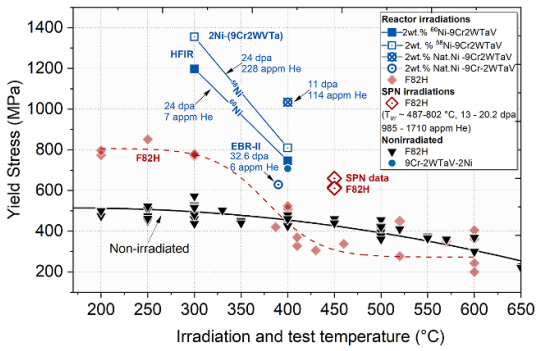

Figure 16. The effect of He on yield stress of RAFM steels. SPN = spallation proton/neutron irradiations. Figure plotted using data from [5, 99, 283, 284].

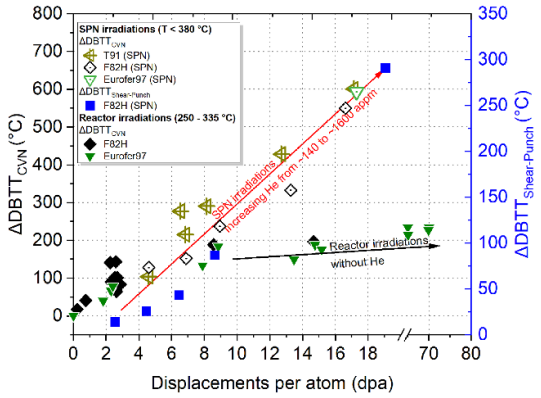

Figure 17. DBTT shifts measured using Charpy impact tests and shear punch tests on SPN-irradiated FM and RAFM steels compared to DBTT shifts measured on MTR irradiated steels. Adapted from [85, 283]. CVN = Charpy V-notch.

^{58}Ni/^{60}Ni-doped steels, are needed to fully understand and properly quantify the dose–temperature–He concentration scenarios on the tensile properties of RAFM steels.

In terms of the Charpy impact properties, the ^{10}B/^{11}B doping technique in F82H shows an appreciable further increase in DBTT in ^{10}B samples due to He after neutron irradiations in JMTR at 250 °C at very low doses (<2 dpa) [285]. The largest database of B-doped neutron irradiation results exists for Eurofer97 from the European irradiation programs SPICE and ARBOR [45, 94, 281], where a higher DBTT due to He is also claimed over a wide T_{irr} range of ∼250 °C–450 °C, doses up to ∼70 dpa and He generation between ∼10–432 appm He. Large DBTT shifts compared to non-doped steels were as high as ∼100 °C for only 120 appm He, and the extra DBTT shift rate of 0.5–0.6 °C/appm He was estimated. However, a major drawback of the studies in Eurofer97 is that the results are derived from natural boron (∼20% ^{10}B) and ^{10}B doping only, and did not include ^{11}B to account for the effect of chemistry modification. Therefore, even though these studies provide valuable data points, the results may not be viewed as a separate effects study purely originating due to He in the absence of ^{11}B data. It must also be noted that while the effect of B on non-irradiated microstructures is relatively well known, what effects it may bring about under irradiation are not fully evaluated in literature. This major unknown further mandates that ^{11}B samples should always be included in such irradiation campaigns and ^{10}B results are not directly comparable with non-doped steels. Data also exist for 2 wt.% natural Ni and ^{58}Ni-doped F82H and 9Cr–1MoVNb steels after HFIR irradiations where some effect of Ni was seen, interpreted as the effect of He on DBTT. However, the results are not clear because the effect of He is masked by the potential effects of Ni addition in the absence of ^{60}Ni-doped samples to account for chemistry modifications [286]. Charpy impact tests and shear punch tests on SPN-irradiated RAFM and conventional FM steels, however, suggest a drastic effect of He on the DBTT shift (figure 17). With increasing doses and added He concentration from ∼140 appm to ∼1600 appm, DBTT shifts as high as 600 °C–650 °C are reported for Eurofer97 and F82H, while the same for MTR irradiations tends to saturate at around ∼200 MPa in the absence of much He. Such drastically strong effects of He suggested by SPN irradiations require validation by high-dose MTR irradiations on carefully isotopically tailored RAFM steels.

While tensile and Charpy tests are important to study the LTHE phenomenon, FT data are the most engineering-relevant to quantify the fast fracture behaviour of RAFM steels. Because of the complexity of the testing technique on neutron irradiated materials, FT data on the effect of He are very limited in literature. Recently, DEMO/FNSF final phase-relevant neutron irradiation data on FT properties were obtained for F82H containing 1.4 wt.% ^{60}Ni and ^{58}Ni (220 °C–530 °C, 6.8–70 dpa and He generation rates of 0.3 and 11 appm He dpa^{-1}) [100]. While the results validated the use of 1.4 wt.% Ni addition, no conclusions could be derived on the critical dose or He concentration levels that could deteriorate FT. Results for T_{irr} ∼300 °C–342 °C, 70 dpa/770 appm He, showed FTTT shifts of >150 °C due to He, but no major effects of He were visible at lower doses up to ∼18 dpa/176 appm He and at higher temperatures (400 °C–500 °C, 8.6–22 dpa, 60–231 appm He), as shown in figure 18. These results contradict Eurofer97 data using the B-doping technique where very little He (as low as 120 appm He) seemed to show an effect on the impact properties [45, 94, 281].

It is evident that more dedicated research is needed to fully understand and quantify the effect of He on the LTHE scenario in RAFM steels. The significant discrepancies and lack of data in the literature imply that the hypothesis of concentrations below ∼500 appm He for T_{irr} < 400 °C having little effect on LTHE require unbiased scrutiny.

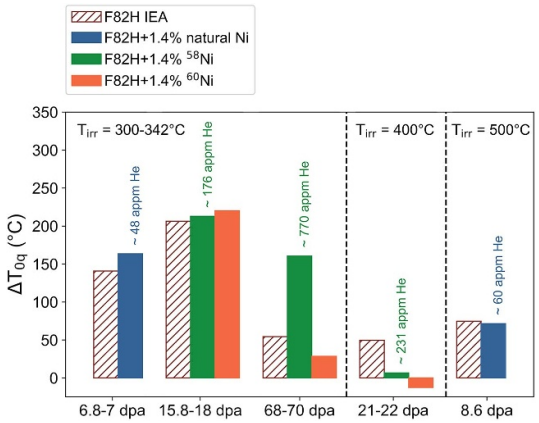

Figure 18. Comparing the positive shifts in the Master Curve provisional reference temperature T_{0q} between F82H IEA and Ni-doped F82H irradiated in HFIR between ~6.8 dpa and 70 dpa. The F82H-IEA data for 68–70 dpa case show low shift in T_{0q} likely due to deviation of irradiation capsule design temperatures versus actual sample temperatures. Reprinted from [100], copyright (2020), with permission from Elsevier.

Very little data exist regarding the susceptibility of ODS steels to potential He-modified fast fracture scenarios. Cyclotron-based He implantation studies followed by Charpy testing on 9%Cr- and 14%Cr-based ODS steels have shown no impact of ~1000 appm He on DBTT [287]. SPN irradiations between 100 °C–360 °C, 20 dpa and up to 1750 appm He show fully ductile tensile fractures in a 14%Cr-based MA957, while 9%Cr FM steels suffered brittle fracture [288]. More experiments are needed to holistically map the dose–temperature–He concentration range on the irradiated mechanical properties of ODS steels.

3.3. Susceptibility of RAFM steels to high temperature helium embrittlement (HTHE)—an open question?

At $T_{irr} \geqslant 0.4\text{-}0.5T_m$, the combination of high He concentration and applied stresses can induce non-hardening grain boundary embrittlement due to the enhanced formation of grain boundary bubbles [85]. This embrittlement being at very high temperatures means the neutron dose is not the primary factor contributing to HTHE [289]. However, conventional martensitic steels and RAFM steels are historically considered highly resistant to HTHE; this has been attributed to the high sink density [287, 290–292] and low creep strength [293, 294] in these steels. Specifically, it is considered that the good resistance of RAFM steels to HTHE is due to the high trapping capacity for helium atoms in the martensitic structure that consists of dislocations, lath/grain boundaries and carbide/matrix interfaces [295]. Thermal desorption studies and simulation studies show that indeed dislocations can trap helium atoms in a bcc Fe-based system [295], while positive binding of helium to other sinks such as grain boundaries or interfaces is a well-known phenomenon. However, SPN-irradiated tensile fracture data on martensitic steels do show severe grain boundary inter-granular failure due to He-induced bubble formation at low irradiation temperatures (<400 °C) [86, 139, 283]. The present hypothesis of better HTHE performance of RAFM steels primarily originates from He implantation studies using cyclotrons, which report no major effect of He on the tensile and in-beam creep performance for T_{irr} > 400 °C and up to 600 °C [290, 291, 293, 295, 296]. Moreover, data from ^{10}B-doped F82H steels neutron-irradiated in the JRR-2 reactor to low doses (<0.1 dpa) also do not show much effect of He on the tensile properties for T_{irr} >500 °C [116]—but high dose data are needed to better understand the behaviour. Further, ion irradiation and cyclotron implantation experiments systematically show very high He-induced grain boundary cavity formation in FM steels, which indirectly suggest a deleterious effect on mechanical properties. Major problems so far are (a) the absence of applied stresses during bulk neutron irradiations, without which the susceptibility of RAFM steels (and ODS) to grain boundary He bubble formation and HTHE cannot be evaluated, and (b) while the cyclotron based in-beam creep tests provide data for good fundamental understanding, they probe only limited sample volumes due to the shallow penetration depths (a few tens of μm) of He ions—therefore bulk properties are inaccessible which can be different from very thin He-implanted samples. Also, most HTHE studies in RAFM steels used post-implantation tensile test strain rates where the HTHE effects might not be evident as compared to reactor design-relevant strain rates of $<10^{-7}$ s^{-1} [297]. It should be noted that limited in-beam creep data on martensitic steels do suggest emerging signs of HTHE when the He concentration is ~3000 appm at 600 °C [293], which highlights that dedicated research on RAFM steel varieties is needed to properly quantify their susceptibility to HTHE. Research on austenitic steels, which has been extensively evaluated for HTHE, shows that the application of stresses during irradiations is critical in quantifying

HTHE because mechanical loads as low as ∼20 MPa can severely accelerate grain boundary cavitation [298]. In fact, the application of stresses during irradiation experiments is critical not only for evaluating the HTHE susceptibility of RAFM and ODS steels but also to properly quantify the overall thermo-mechanical performance relevant for FW/B conditions that will suffer from very high thermo-mechanical loading conditions, including transients [1, 51, 54, 299]. This is a critical technical gap that necessitates performing irradiation experiments under stress, especially during in-pile neutron irradiations.

An important point to note is that increasing the sink strength, such as by nano-dispersoids in ODS steels or increasing the concentration of MX in RAFM steels, is a desired pathway to distribute He in the alloys and prevent He-induced grain boundary embrittlement [190, 300]. In fact, oxide nano-dispersoids are excellent to sequester He [301, 302] and are therefore excellent to manage He in fusion structural steels. However, as will be detailed in section 7, increasing the nano-dispersoid or MX number density is a trade-off because on the one hand it helps to manage He better, but on the other hand there is a risk of excess tritium trapping in high sink strength materials [303].

4. Cavity swelling in RAFM and ODS steels

In the intermediate temperature range of ∼400 °C–500 °C, dimensional instabilities due to cavity swelling are a concern for fusion structural steels. Furthermore swelling–creep interactions concomitantly worsened by radiation-induced microchemical phenomenon such as radiation-induced segregation/precipitation that is pronounced in this temperature region [49, 304] are expected to synergistically worsen the steels' overall performance. Conventional FM and RAFM steels offer superior cavity swelling resistance as compared to Fe–Cr–Ni-based austenitic steels [49, 57]—which is the primary reason for their choice as FW/B structures [58, 299]. Their post-transient steady-state swelling rate is generally accepted as 0.2% dpa^{-1} as compared to 1% dpa^{-1} for austenitic steels [49, 305], while the length of the swelling incubation period is also larger for RAFM steels.

Despite the improved radiation tolerance, experimental observations after fission neutrons suggest that the cavity-swelling performance of RAFM steels such as F82H or Eurofer97 is adequate only for doses up to ∼20–50 dpa at ∼400 °C–500 °C (figure 19). While high dose swelling data exist for conventional steels like T91 or ODS varieties like MA957, there is a lack of neutron data in the literature beyond 50 dpa on the swelling behaviour of the well-known RAFM steels like F82H or Eurofer97. It has been recognised for many decades that high concentrations of He and H produced by neutron transmutation in RAFM steels will worsen the swelling behaviour. Therefore, the radiation resistance offered by RAFM steels during fission neutron irradiations may be severely impaired during DT fusion neutron irradiations. Figure 19 summarises some experimental results on the effects of He co-generation during neutron irradiations on RAFM steels for T_{irr} ∼380 °C–430 °C. Fission reactor data show ⩽1%–1.2% swelling at around ∼50 dpa at 400 °C in Boron-doped F82H due to combined neutron damage plus He, while the swelling reduces to lower values in the absence of He. It is unclear how the swelling scenario will evolve at higher doses. Particularly, identifying the onset doses for steady-state swelling around the peak swelling temperatures of RAFM steels requires high dose neutron irradiation experiments in the intermediate temperature range from ∼400 °C–500 °C. Dual and triple ion beam results suggest fusion-relevant He and H will accelerate the swelling in RAFM steels [306, 307].

Irradiation studies show exceptionally high swelling resistance of ODS steels as compared to FM steels [308–310]. Figure 19(a) shows the superior swelling resistance of 14%Cr-based MA957 compared to RAFM and conventional FM steels up to 500 dpa. The resistance to cavity swelling originates from the high density of oxide nano-dispersoids that act as efficient point defect sinks that lower the defect supersaturation by enhancing recombination at the matrix-dispersoid interface [49]. Therefore, the irradiation stability of the nano-dispersoids ultimately controls the radiation tolerance of ODS steels. Until now, it was typically considered that nano-dispersoids in ODS steels will be stable under thermal-ageing or neutron irradiations. However, as detailed in section 2.5, experimental results on many neutron irradiated ODS steels show severe structural and chemical instabilities in nano-dispersoids, including modifications of the matrix–particle interfacial chemistry [224, 266]. Such degradation of the nano-dispersoids may compromise the radiation tolerance of ODS steels, including resistance to dimensional stability, which requires thorough future evaluation. Further research using advanced analytical characterisation tools is needed to fundamentally understand the irradiation degradation mechanisms of ODS particles and its implications on radiation tolerance.

5. Irradiation creep and creep–fatigue interaction

In addition to cavity swelling, another crucial dimensional instability phenomenon is creep, which can be a combination of thermal creep or irradiation creep. It is well known that conventional FM and RAFM steels

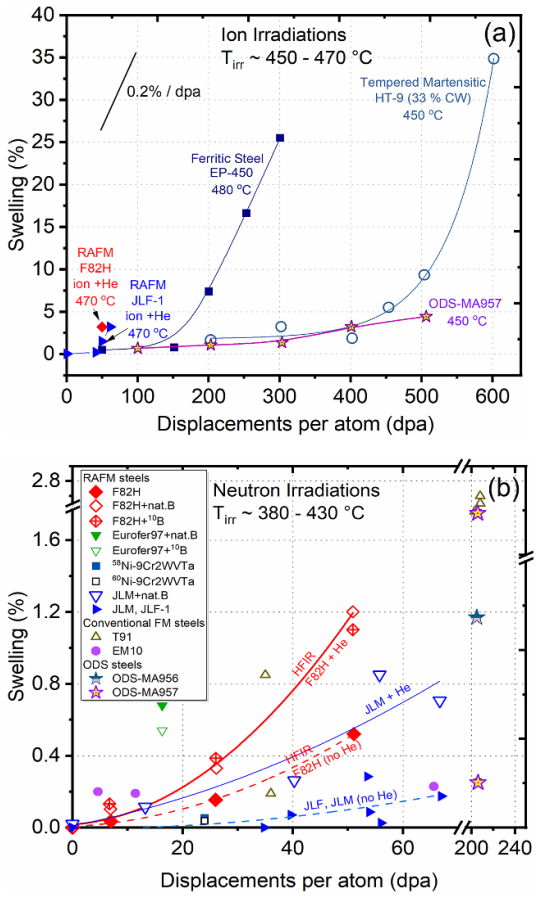

Figure 19. (a) Cavity swelling in ion irradiated and (b) neutron irradiated RAFM, conventional FM and ODS steels. For neutron irradiations, the effect of He on swelling is simulated by B doping and ^{58}Ni/^{60}Ni isotopic tailoring technique. Data used from [87, 99, 119, 199, 208, 308, 309, 311–317]. Figure (a) reprinted from [309], copyright (2014), with permission from Elsevier.

show poor thermal creep strength after 500 °C–550 °C, while ODS steels have a highly superior creep performance. Irradiation creep acts in addition to thermal creep. Collectively, creep and swelling can induce significant dose-dependent distortion of fusion reactor structures that experience variations in dose rate, temperature or stress state [319]. Irradiation creep is one of the earliest reported radiation degradation phenomena in materials [320], and phenomenologically is proportional to the displacement damage dose and the applied stress with a weak temperature dependence between ~0.25 and 0.5T_m [321–325]. The magnitude of steady-state irradiation creep can be empirically described by the following equation [326]:

$$\dot{\varepsilon} = \boldsymbol{\sigma}\left[\boldsymbol{B}_0 + \boldsymbol{D}\dot{\boldsymbol{S}}\right] \quad (1)$$

where $\dot{\varepsilon}$ is the plastic strain rate per unit dose, $\boldsymbol{\sigma}$ is the applied effective stress, $\mathbf{B_0}$ is the creep compliance for irradiation creep, $\mathbf{D}$ is the irradiation creep-swelling coupling coefficient, and $\dot{\boldsymbol{S}}$ is the cavity swelling rate per unit dose. Several studies on austenitic steels have also reported the existence of a transient low-dose regime with relatively high irradiation creep [327, 328], but there is limited reported evidence for this transient creep regime in FM steels. The typical reported creep compliance term for FM steels (including reduced activation steels) is $B_0 \sim 0.5 \times 10^{-6}$ MPa^{-1} dpa^{-1} [69, 305, 329, 330]. The swelling creep coupling coefficient (D) has reported values near 0.006–0.025 MPa^{-1} for ferritic steels [329]. Considering the reported steady-state cavity swelling rates in FM steels of 0.1–0.2% dpa^{-1} and much lower swelling rates in the lower-dose transient regime [49], the irradiation creep of FM steels is typically dominated by the B_0 creep compliance term in the low-dose (lowswelling rate) transient regime and is dominated by the creep-swelling coupling term once steady-state swelling is achieved. The overall plastic deformation associated with irradiation creep in FM steels is relatively minor for fusion reactor design-relevant conditions (figure 20). For example, assuming an applied stress of 100 MPa and a design dose of 100 dpa, the irradiation creep associated with the creep compliance term (B_0) is only ~0.5%, which is comparable to the linear expansion induced by heating the steel component from room temperature to 500 °C. Significant anisotropy in the faulted dislocation loop habit planes has been reported to occur in facecentered cubic alloys irradiated with applied stress (taken as evidence for stress-induced preferential absorption of point defects, SIPA, being a predominant contribution

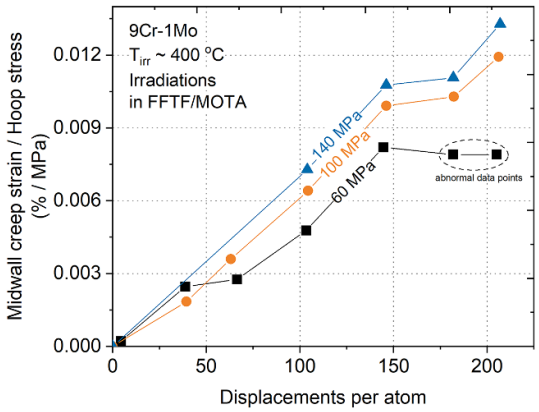

Figure 20. Irradiation creep in 9%Cr steels. Data show stress normalised midwall creep strains for 9Cr–1Mo steel pressurised creep tubes irradiated at nominal temperature of ∼400 °C by fast neutrons in the materials open testassembly in the FFTF. The data for 60 dpa hoop stress at higher doses show spurious results that should be ignored because irradiation creep should be proportional to dose. Reprinted from [334], copyright (1994), with permission from Elsevier.

to irradiation creep) [331, 332], but evidence of the pronounced anisotropic loop habit plane behaviour has not been frequently reported in FM steels, including the reduced activation variants.

There are mixed observations regarding the potential effect of high atomic densities of precipitates or dispersoids on the steady-state irradiation creep levels in alloys. From standard rate theory calculations, a high sink strength would be predicted to induce lower irradiation creep rates due to suppressed point defect supersaturation levels. Paxton *et al* reported reduced irradiation creep in austenitic alloys with high precipitate densities [325], whereas other austenitic steel studies have not observed a significant effect of sink strength [206, 325]. The reported steady-state irradiation creep compliance for MA957 ODS ferritic steel was comparable or slightly higher than the typical values for standard FM steel [333]. Additional experimental irradiation creep data on FM steels with a wide range of dispersoid densities would be useful to better quantify potential sink strength effects.

One important consequence of irradiation creep is that stress relaxation of components such as springs and fasteners will inevitably occur in irradiated structural components [335]. This creates considerable design challenges for secure fastening methodologies; the retained stress may decrease to ∼10% of the initial value after doses of ∼10 dpa [328].

Strength degradation associated with combined plastic deformation from creep and fatigue is an important consideration for structural materials exposed to non-static loads [336, 337]. Plastic deformation during cyclic fatigue can produce a dramatic reduction in creep lifetime. In general, either time fraction (stress-based) or ductility exhaustion (strain-based) approaches have been used to estimate creep–fatigue failure criteria [338–340]. It has been noted that the traditional ASME boiler and pressure vessel section III, Division 5 creep–fatigue methodology can produce very conservative predicted lifetimes in FM steels such as modified 9Cr–1Mo steel [341, 342]. This may be due in part to the effects of cyclic softening and coarsening of the FM steel microstructure during the fatigue testing; such effects may need to be taken into account for more precise damage calculations [343]. Essentially nothing is known regarding the creep–fatigue behaviour of FM and RAFM steels during irradiation, which remains a critical R&D gap to validate the application of such steels in fusion environments.

6. Strategies to improve RAFM steel performance for fusion applications

For high-temperature blanket operations, the structural steels must possess good high temperature mechanical properties. While ODS steels show excellent high temperature strength and creep performance, the main drawback of RAFM steels is their thermal creep performance, which is inferior to that of conventional steels like Grade91—which limits their maximum operating temperature at ∼550 °C [58, 299, 344]. To achieve a high thermal efficiency of the power conversion systems required for future fusion power plants, there is a need for structural steels that can operate up to significantly higher temperatures (up to 650 °C, possibly beyond) [345]. Therefore, there is an ongoing effort worldwide to develop alternative RAFM steels with improved high temperature mechanical properties such as strength, creep and creep–fatigue properties to allow for an extension of the operational temperature range [3, 70, 346]. As mentioned in the introduction, the high temperature mechanical properties of RAFM steels, in particular their thermal creep resistance, are due to their tempered martensite microstructure. Several

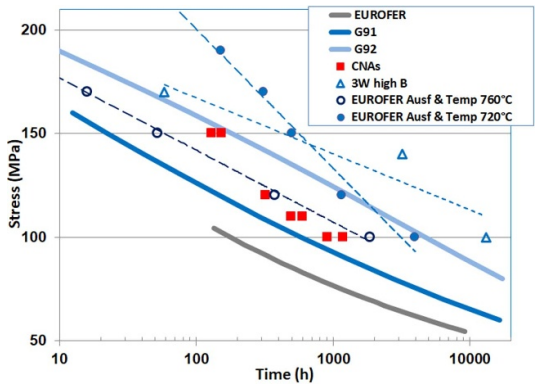

Figure 21. Stress as a function of time to rupture for creep tests performed at 650 °C on CNAs [355], 9%Cr–3%W-B (3WhB) RAFM steel [359] and Eurofer97 [360]. The data shown in this figure correspond to ausformed Eurofer97 tempered at 760 °C. Comparison with creep data for baseline Eurofer97 [361], Grade91 and Grade92 [362].

features contribute to the strength of these steels at elevated temperatures, such as dislocation and lath/block boundary hardening, solid solution strengthening and precipitation hardening [347, 348]. $M_{23}C_6$ carbides and MX (M: metallic elements; X: C and N) carbonitrides are formed during tempering, while other phases, for instance Laves phases, may precipitate during long-term operation at high temperature [347, 349–352]. The presence of fine coherent or semi-coherent MX particles is known to play a key role in the long-term creep resistance at high temperatures of FM steels due to their slow coarsening rate by Ostwald ripening [353]. Therefore, the strategy followed by alloy designers for certain advanced RAFM steels such as the CNAs [3, 354, 355] is to increase the amount of MX compared to the volume fractions present in Eurofer97 or F82H. CNAs strengthened by MX carbonitrides or MX carbides were developed, with a focus on strengthening by carbides [355]. The chemical compositions of the 'carbide-CNAs' include Ti, in the range 0.11–0.16 wt.%, and the N content is restricted to less than 40 ppm, which promotes the formation of (Ti, Ta)C carbides, while avoiding the formation of coarse TiN particles or the conversion of MN nitrides to Z-phase nitrides with a high coarsening rate during long-term service at high temperature, a phenomenon known to induce significant loss of precipitation strengthening [356]. The calculated equilibrium MX volume fractions in the CNAs are up to 0.5%, significantly higher than the MX volume fractions in Eurofer97 and F82H (<0.2%) [3, 354]. The CNAs were fabricated at laboratory scale (in batches of 0.7–23 kg), and their microstructures and mechanical properties were characterised in detail. In addition to a high density of MX precipitates, especially in the carbide-CNAs [269, 355], these steels also show much refined tempered martensite microstructures, i.e. smaller size of laths, packets, prior austenite grains as compared to the microstructures observed for baseline RAFM steels. As a result, the CNAs exhibit increased strength. For example, CNAs show up to 300 MPa higher yield stress than reference RAFM steels like Eurofer97 or F82H when tested in the RT–800 °C range, at a cost of slightly lower total elongation [355, 357]. It is important to note that despite the increased tensile strength, Charpy impact tests reveal DBTT values comparable to those measured on current RAFM steels, together with higher upper shelf energies (USEs). In particular, the carbide-CNAs exhibit a high USE, which is tentatively attributed to the lower nitrogen and carbon content [355]. Creep tests performed at 600 and 650 °C show that CNAs exhibit much higher creep resistance compared to baseline steels such as Eurofer97 (see figure 21 and [355]). Figure 21 also suggests an improved creep performance of CNAs as compared to Grade91, although additional data are needed for confirmation. It should, however, be noted that better creep properties of CNAs versus other steels requires further validation from long-term creep data, preferably up to 5000 h or higher.

Since ASME code approval of Grade91 in 1984, new 9%Cr FM steels with much improved creep resistance have been developed [356, 358] such as Grade92 (see figure 20). Contrary to Grade91, Grade92 is alloyed with W and with some B addition. The current 9%Cr conventional FM steels with the highest creep resistance contain about 3 wt.% of W as well as B content up to about 140 ppm [75, 347]. To increase the creep strength compared to Eurofer97, an approach followed in Europe was to investigate RAFM steel compositions inspired by the best performing conventional steels, i.e. with 3 wt.% W and high B content. However, due the low activation requirements, some elements, for instance Co, which among other effects acts as an austenite stabiliser, could not be included in the selected chemical compositions. Therefore, to somewhat mitigate the ferrite stabilising effect of high W content up to 3 wt.% and ensure a fully tempered martensite final microstructure, the Mn concentration was raised from 0.5 wt.% as in reference Eurofer97 to 1 wt.%. Further, the N content was kept low to avoid the formation of coarse boron nitride particles, which

would reduce the available B content and degrade the toughness properties. Boron has long been known to have a beneficial effect on creep lifetime [363]. The loss of creep strength during long-term tests at high temperature is correlated with the recovery of the tempered martensite microstructure, including the subgrain structure, which is enhanced near prior austenite grain boundaries [347]. $M_{23}C_6$ carbides stabilise the subgrains but become less efficient due to coarsening. Microstructural investigations such as atom probe experiments have shown that B is enriched in $M_{23}C_6$ carbides in B-added steels [360–362] but not in other types of precipitates. B enrichment is considered to decrease the coarsening rate of $M_{23}C_6$ carbides, thereby enhancing the creep resistance of B-added steels, although the underlying mechanism is yet to be fully understood [366]. As pointed out by Klueh [367], for use in a fusion reactors ^{11}B should be used, as natural B contains ∼20% ^{10}B, which transmutes during irradiation with the formation of He and Li. Regarding W, high W content improves the creep properties, due in part to solid solution strengthening. However, during creep at temperatures typically above 500 °C, Laves phase precipitation occurs in steels with supersaturated W in solid solution. It was shown that fine precipitation of the Laves phase is beneficial as it decreases the creep rate in the transient creep region, although subsequent coarsening of the precipitates induces a creep acceleration [368]. Recently, creep tests were performed at 650 °C on an experimental RAFM 9%Cr–3%W-B steel batch (known as 3WhB) designed in Europe [359]. While additional tests are needed to fully identify quantitative trends, the early results are encouraging as they indicate that the investigated B-added steel has higher creep resistance than Grade92 (see figure 21). However, in contrast to the CNAs, the 9Cr3WB RAFM steel exhibits poorer impact properties than Eurofer.

An alternative strategy to improve the high-temperature mechanical properties is to apply thermomechanical treatments (TMTs). These treatments usually involve nonstandard normalisation and/or tempering conditions, in most cases combined with a controlled plastic deformation stage, such as warm rolling in the metastable austenite domain (ausforming). This type of approach was used in the past for conventional FM steels [75, 77, 369–371]. Following the early pioneering work of Klueh at ORNL [14, 74], TMTs are also being further developed to improve the properties of RAFM steels (both baseline steels or steels with optimised chemical compositions) [27, 346, 360, 369]. In many studies, a higher austenitisation temperature than the standard values was used to enhance the dissolution of precipitates, especially MX [77, 346, 360, 370, 372]. This is to target an increased number density of MX precipitates after tempering, especially when tempering is performed at lower temperatures than the standard 750 °C–760 °C. However, this type of treatment leads to a coarsening of the austenite grains, which can grow to very large sizes when the selected austenitisation temperatures are high enough to induce complete dissolution of the MX precipitates that cannot pin the austenite grains any further [372]. Ausforming is reported to modify the martensitic microstructure both in the as-quenched and tempered conditions. For instance, in as-quenched martensite, ausforming increases the density of dislocations, which act as nucleation sites for MX precipitates during tempering and refine the sizes of martensite laths and subgrains [77, 369, 370, 373]. An additional effect is to produce an anisotropic microstructure, with elongated grains in the rolling directions, and texture, due to variant selection resulting from martensite transformation of deformed austenite [370, 372]. After tempering, in many cases ausforming is shown to modify the precipitate distributions, with increased densities of MX precipitates and refined precipitate sizes [369, 370, 374].

In terms of the mechanical properties at high temperatures, TMTs induce a large increase in tensile strength as well as a strong improvement of thermal creep resistance [75, 346, 360, 369, 374]. The fatigue properties are also improved, although the cyclic softening phenomenon known to occur in FM steels is typically not suppressed [75, 77]. An example of the effect of TMT on the creep properties of Eurofer97 is shown in figure 21, where ausforming (hot-rolled with 40% thickness reduction at 650 °C and tempered 1 h at 760 °C) exhibited a creep behaviour of Eurofer97 comparable to that of the CNAs. However, in contrast to CNAs, ausforming degrades the impact properties compared to the reference Eurofer97 in the standard metallurgical condition. Tempering at lower temperatures (720 °C) may result in much longer creep lifetimes, but at the cost of a further degradation of the impact behaviour [360]. Other drawbacks of TMT are the induced texture, elongated grains and associated anisotropy of mechanical properties. Finally, it should also be pointed out that the fabrication of breeding blankets (BB) for future fusion reactors will likely involve many welding operations. Therefore, the suitability of using RAFM steels subjected to TMT for BB fabrication is questionable, since the effect of TMT will likely be lost after welding, especially after several welding operations and post-welding heat treatments.

FT improvements of RAFM steels by TMTs combined with minor alloying chemistries has been attempted, for example in the mod3 variant of F82H [20] and some variants of Eurofer97 [62]. While the mod3 variants showed improved mechanical properties in the non-irradiated condition and seem to show slightly better FT properties after high dose neutron irradiations [100], the variants of Eurofer97 fabricated with TMTs showed only modest improvements in the neutron irradiated FT and tensile properties [64, 66]. While harder under-tempered steels designed to target improved high-temperature properties naturally

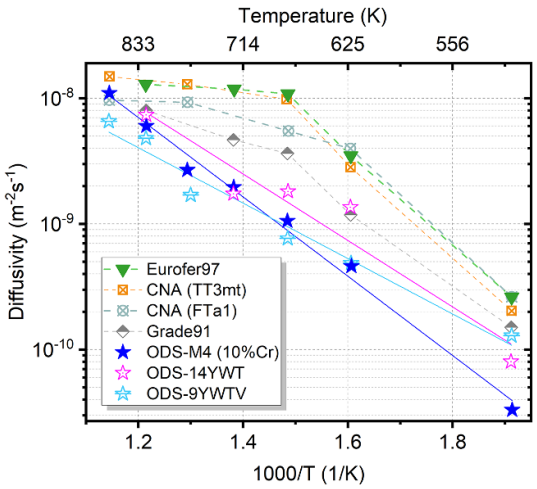

Figure 22. Diffusivity of deuterium in FM, RAFM and ODS steels. Reprinted from [384], copyright (2021), with permission from Elsevier.

show poor LTHE susceptibility [62, 66], only TMTs targeting prior austenite grain size reduction showed some promise regarding improved LTHE behaviour [63, 66]. It remains challenging to develop alloys that show improved resistance to radiation hardening/embrittlement while simultaneously showing better high-temperature creep.

7. Tritium management

In DT fusion reactors, tritium management is essential to minimise tritium loss to the coolant and release to the environment through the steam generator, and to minimise the amount of tritium inventory in the fusion reactor. Therefore, tritium permeation and inventory are key issues in fusion development [375, 376]. Since hydrogen permeability is generally known to be high in ferritic steels, the tritium permeability of RAFM steels and their ODS counterparts have been actively studied [377–384]. Tritium permeation of ferritic ODS steels (from the nuclear fuel pellet to the cooling water in fission reactors) has also been studied due to the interest in ferritic ODS steels as a candidate for accident-tolerant fuel cladding [385, 386]. It is observed that hydrogen diffusion in RAFM steels is generally comparable or better than in other martensitic steels, while higher Cr concentration results in lower permeability [378, 380, 384], and it has been pointed out that grain boundaries, including martensitic lath boundaries where Cr carbides precipitate, may serve as hydrogen trapping sites. The effect of surface oxidation has also been noted as a major factor in lowering the permeability [381], and the permeability of ODS steels has been reported to be much lower than that of RAFM steels. Some studies suggested that the ODS grain surface (or oxide/matrix interface) may be a further hydrogen trapping site that causes overall lower diffusivity [379, 385].

Figure 22 compiles the data on various RAFM, FM and ODS steels, where the diffusivity of different ODS steel varieties is compared to Grade91, two CNA variants and Eurofer97 using deuterium as a surrogate for tritium [384]. The lower diffusivity (higher retention) of deuterium in ODS steels is evident, and is presently attributed to the positive interaction and trapping of hydrogen with the high grain boundary density (due to the smaller grain sizes), dislocations and most importantly with the strengthening particles, postulated both experimentally [384, 387] and theoretically [388]. This trade-off issue, where the finer microstructure of ODS steels traps more hydrogen, but on the other hand is beneficial for helium embrittlement, requires further analysis to find the right balance of properties. If too much tritium remains trapped in ODS steels during in-service applications, it may pose risks to safety and operations, which requires scrutiny. Of particular potential concern is the possibility of dramatically enhanced tritium trapping at radiation-induced He-containing cavities preferentially located at the interfaces between ODS particles and the matrix (in addition to the H isotope trapping at dispersoid interfaces observed in non-irradiated materials) [50, 303]. Future research should focus on this critical topic, including understanding the tritium retention complexities in this class of materials in the presence of radiation damage (particularly in the void swelling regime) that are presently not well understood.

It should be noted that the permeation environment may influence the permeation behaviour. While many permeation studies have used a vacuum downstream to permeate hydrogen, it has been reported that an Ar gas atmosphere can alter the oxygen potential and affect the chemical form (gas or water) of the

molecules released from the surface, affecting the final permeation rate [382]. It has been reported that the molecular form of hydrogen released from the surface in ODS steels is the gaseous molecular form due to the high stability of the Cr_2O_3 surface.

8. Need for advanced characterisation and multiscale modelling

8.1. Advanced characterisation

Advanced characterisation of the microstructure is required for improving alloy designing activities in support of fusion energy [389]. Advanced characterisation of the microstructure and elemental distribution at the near-atomic scale is also required to understand the different irradiation degradation scenarios in RAFM and ODS steels, caused by either formation of second-phase precipitates and solute nanoclusters, extended interstitial-type/vacancy-type defects or changes induced by He or tritium present in the material. Many examples are available in the literature, in which advanced characterisation tools have improved the understanding of the structure and chemistry of defects, with the predominant characterisation tools being APT, TEM and STEM combined with analytical techniques such as EDX and electron energy loss spectroscopy (EELS), small angle neutron scattering (SANS), and more recently transmission Kikuchi diffraction. Tools such as APT and analytical STEM are a necessity because the chemistry of RAFM and ODS steels will evolve in-service, either by nuclear transmutation or by radiation-induced clustering of elemental species. The three-dimensionality of the analysis and the capacity to resolve the chemical identities of atoms with APT, even at extremely dilute concentrations, or of very light species that are not easily distinguishable via electron microscopy, help us understand the contribution of different chemical phenomena to the steels' thermo-mechanical response. As an example, the potential deleterious effect of Mn–Si and Cr–Mn–Si–P co-clustering on LTHE in RAFM steels was only discovered recently when APT experiments were performed on neutronirradiated materials (figure 12), which explained the extra experimental hardening detected in these alloys compared with dispersed barrier hardening model predictions [177]. Access to other complimentary analytical tools like STEM-EDX with modern data analytics like MVSA collectively aid in presenting a detailed picture of fusion structural steels' irradiation-driven chemical phenomena. However, because of the strengths and weaknesses of individual techniques, no single technique can solve the problems associated with fusion structural steels. Therefore, combinations of two or more techniques need to be applied in order to get a more complete picture, including the composition, morphology and distribution of radiation-induced defect features. For example, STEM-EDX spectrum imaging (with or without MVSA) usually presents an excellent picture of embrittling microstructural features like solute nanoclusters in steels (figure 13(c)), but the analysis is often qualitative because of the nanoscale features being embedded in a matrix containing similar elements as in the defect, thereby requiring quantification by APT. Combined analytical STEM and APT analysis of radiation-induced/enhanced solute nanoclustering is needed to understand the complex LTHE scenario in ODS steels, where irradiation hardening is detected up to very high temperatures (figure 11). Scattering techniques such as SANS that can probe the variances of length densities within a material have the advantage of yielding information from a relatively large volume of material; thereby the data derived from SANS are considered to be from the 'bulk' of the material [183, 390, 391]. A quantitative understanding of the Cr-rich embrittling α' phase in Fe–Cr-based steels is largely derived from combined APT and SANS studies [390]. It should be noted that while accurate quantitative prediction by SANS requires some prior knowledge of the features, combined STEM, APT and SANS investigation studies regarding embrittling features in RAFM and ODS steels are not nearly as vast as for other widely studied steels that are also prone to LTHE, such as RPV steels [183, 392]. Learnings from RPV steels also suggest that the quantification of vacancy-type defects that are below TEM's resolution limit is necessary to present a full picture of the steels' microstructural evolution scenario [183]. Given that the formation of solute nanoclusters causing hardening-embrittlement often requires vacancies, tools like positron annihilation spectroscopy are needed to quantify the vacancy defects and develop a phenomenological understanding of microstructure evolution in neutron irradiated RAFM and ODS steels.

The radiation tolerance of structural materials is inherently dependent upon the stability of the high density of point-defect sinks such as the MX phase in RAFM steels or nano-dispersoids in ODS steels. Central to this is how the composition of these nanofeatures and structures modified by irradiation may affect the bulk performance. While the MX particles are generally considered radiation-tolerant [393, 394], the stability of different oxide nano-dispersoids under neutron irradiation remains an open debate. Figure 14 suggests that oxide nano-dispersoids can suffer from drastic structural–chemical changes in real high dose neutron irradiation environments. While the true origins of such complex transformations in ODS particles are presently unknown, they are expected to be driven by multiple synergies under neutron irradiation (including transmutation effects) that may often not be well represented by high dose rate ion irradiation experiments, where nanoprecipitates are susceptible to ballistic dissolution [195]. Such degradation as in

figure 14 of ODS particles may not be easily distinguishable by conventional characterisation techniques and requires analytical STEM or high-resolution TEM/STEM studies. More neutron irradiation studies over a wide range of doses and temperatures followed with high-resolution characterisation in post-irradiation examination is required to develop a thorough understanding of the instabilities in both nano-oxide particles and MX-type precipitates. It should be noted that most studies examining the oxide particles have used APT. But due to trajectory aberrations during the field evaporation of oxides, obtaining accurate compositions can be challenging, and necessitates performing both APT and STEM investigations. In ODS-Eurofer97, APT was used to examine the composition of the nano-dispersoids, and it was found that the metal:oxide ratio (Y,Mn,Si:O) was around 3:2 [395]. In a high-resolution TEM study of nano-dispersoids in ODS-MA957, the structure was postulated to be that of a $Y_2Ti_2O_7$ pyrochlore phase [396]. This phase results in a M:O of 4:7—the inverse of the M:O ratio calculated in the characterisation of the ODS-Eurofer97. At this stage it is also important to acknowledge that the proposed structures of $A_2B_2O_7$ or A_2BO_5 pyrochlore phases for the nano-dispersoids can be thermodynamically stable in non-stoichiometric ratios, and can in particular accommodate significant structural vacancies [397, 398]. Given the propensity of the pyrochlore (and perovskite) phase to accommodate vacancies and additional elements [399, 400], measurement of the compositions of the nano-dispersoids can be challenging due to the errors/aberrations inherent to the techniques used for the observation, e.g. APT and STEM.

Regarding the effect of He, the accumulation within the matrix and on grain boundaries as cavities causing embrittlement requires dedicated studies using advanced characterisation tools [401]. While the classical method of quantifying the size and number density of He-induced cavities is using the Fresnel contrast in TEM [402], the content of He within cavities is a key question that has serious challenges. This quantification, if possible, would help to identify the early stages of potential He-induced hardening-embrittlement or to identify the key underlying He migration mechanisms in RAFM and ODS steels having complex microstructural features as compared to simple bcc Fe or Fe–Cr alloys. The use of EELS *in situ* of a STEM offers the possibility of determining the He concentration [403]. Using this technique, the He 1s signal is located within the low-loss region of the energy loss spectrum (∼15 eV depending on the material). This is co-located with the plasmon peak and therefore obtaining sufficient signal-to-noise to deconvolve the plasmon and He 1s signals is critical. Early research on He bubbles, for example in He-implanted SiC, showed that during data capture, the He signal decreased with increasing electron exposure [404]. This was ultimately attributed to the energetic electrons knocking out He from the cavity during observation. Surface plasmons should also be accounted for when attempting to quantify He concentrations using STEM-EELS techniques. With the advent of monochromated aberration-corrected STEM microscopes, the EELS energy resolution improvements below sub-10 milli eV are now possible [405], and hold promise to significantly improve the signal-to-noise ratio for quantifying He inside bubbles in fusion structural steels. This quantification is necessary not only for RAFM steels but also for ODS steels that can sequester He through trapping at the nano-dispersoids [406, 407]. As the He accumulates around the particles, it is unclear how the defect trapping efficiency of the matrix–particle interface may evolve.

8.2. Multiscale modelling

Modelling must play a critical role in alloy designing, in the planning and interpretation of irradiation experiments, and in the design of in-vessel components for fusion reactors. Regardless of the choice of structural and functional materials, it is unlikely that experimental testing alone will provide sufficient data to predict all aspects of engineering performance in future fusion builds. The challenge for modelling is to integrate and extrapolate from fundamental approaches at small length and time scales out to engineering-relevant predictions of performance at the reactor scale (size and operational time); this requires a so-called multiscale approach [408].

A key aspect of this integration concerns using predictions based on the fundamental nuclear physics of how neutrons interact and change matter in models that can elucidate the consequences for material behaviour associated with those fundamental reactions, including aspects related to transmutation and damage. Modern computational tools can simulate the propagation of neutrons through models of fusion reactors. These ‘transport simulations’ provide instantaneous neutron fluxes and energy-spectra but cannot easily consider the temporal effects (e.g. transmutation, swelling, functional changes) due to the computational expense of representing reactor geometries and propagating neutrons, usually via statistical Monte-Carlo methods, through metres of material and undergoing dozens of interactions (each). However, these simulations can be used to help predict the (structural) damage creation events in materials during reactor operation—by recording the energies of the recoiling atoms that undergo collisions with the neutrons. In practice, this is a little used feature of transport simulations, which often does not go beyond, from a damage perspective, the simple dpa measure of damage dose. Alternatively, moving beyond dpa [409] can begin with evaluation tools such as SPECTRA-primary knock-on atom (PKA) [410, 411], SPECTER

[412] or dedicated event-generator codes such as PHITS [413, 414], can calculate the distribution of recoil events, the so-called PKAs, which can be subsequently used in modelling to predict the creation and evolution of microstructural damage; for example, using the method of cluster dynamics [415]. In the case of alloys, including steels, codes such as DART [416] can even account for compound effects, where the total damage dose is not merely a linear combination of the evaluated damage in matrices of the individual elements making up a compound [417].

The same input nuclear data used in transport simulations (or PKA evaluations), describing how the neutrons interact with matter, and combined with the 'zero time' neutron fields from the transport simulations, can be used to perform inventory calculations, which model the time evolution in material composition (the transmutation or 'burn-up'). For example, figure 23 and the associated video file (available online at stacks.iop.org/JPEnergy/4/034003/mmedia) show the output of such a simulation, performed with the FISPACT-II inventory code [418] for Eurofer97 steel during a two full-power year irradiation in a typical first-wall fusion environment for EU-DEMO. These data, either at the individual nuclide/isotope level in the chart of the nuclides-style tableau [419] in the figure/video, which is particularly important for understanding the radiological response of materials, or at the elemental level (e.g. as shown in the line graph in the figure) must be included in any multiscale modelling framework. Of particular significance in figure 23 is the prediction of the production of He and H, which is calculated to be much higher in fusion compared to fission [56], due to the higher production probability (cross-section) of key gas producing neutron reaction at DT fusion neutron energies. Section 3 discussed the implications of high He production rates in RAFM steels.

Beyond the fundamental nuclear physics aspects, modelling of complex alloys like RAFM and ODS steels is challenging. However, there have been recent advances in the multiscale modelling formalism of fusion materials, including on Fe–Cr alloys (which are the most simple representatives of RAFM/ODS steels), where both modelling and supporting experiments on these binary (or sometimes ternary) systems are seen as a step on the path to being able to model the full complexity of engineering steels. Soisson and Jourdan [420] reproduced the experimentally observed radiation-enhanced diffusion (RED) in low-flux irradiation of Fe–Cr alloys, which leads to segregation of Cr and embrittling α' formation, using atomistic kinetic Monte Carlo simulations. Phase-field modelling [421], meanwhile, demonstrated that both RED and cascade mixing must be included to explain the formation of α' phase in Fe–Cr exposed to ion irradiation. Balbuena *et al* [422] confirmed, via Object kinetic Monte Carlo (OkMC) simulations, that segregation and precipitation in Fe–Cr is driven by the populations of defects—the vacancies and self-interstitials—created by irradiation. Modelling of how structural damage evolves in alloys beyond the initial formation of damage in individual cascades has also progressed. For example, OkMC has been used to study the microstructural evolution of irradiated Fe–Cr alloys. Chiapetto *et al* [423, 424] used OkMC to show that irradiation-induced swelling is strongly dependent on Cr content, allowing interpretation of the experimentally observed suppression of swelling in the presence of Cr [88, 425], while showing that too much C might negate the benefits produced by Cr. However, further work, even in the relatively simple binary Fe–Cr case, is still needed; for example, the complete phase diagram as a function of temperature for this system is still uncertain [426]. Translation of the fundamental modelling of phase separation in simple systems needs to evolve to incorporate complicated microstructures and differing chemistries typically encountered in steels that may explain other deleterious features contributing to the degradation of steels under irradiation (such as the clustering detected in neutron-irradiated RAFM and phase instability in ODS steels shown in figures 12 and 13). Such activities are crucial given the evolving chemistry of steels under irradiation (figure 23).

There have also been recent significant improvements in modelling and interpretation of behaviour in simple, one-component systems, and this is where multiscale modelling is beginning to provide an understanding at the engineering scale. Dudarev *et al* [427] developed an approach that exploits elasticity to evaluate the strains, stresses and swelling in nuclear components based on considering the relaxation volume of radiation-induced defects, which can now be applied, via finite element analysis, to real engineering designs of fusion components using information about damage events predicted by nuclear transport codes [428]. As discussed in the next section, constitutive models based on the experimentally measured properties of RAFM steels are helping to generate a first-hand impression of the mechanical response of FNSF components at engineering-relevant levels—such component scale modelling via the finite element method requires input from atomistic and microstructure models.

Even atomistic simulations (mainly molecular dynamics or MD), while still limited in scale (time and space), are at least now able to produce statistically significant databases of damage cascades, for example in Fe, that can be exploited to understand cascade overlap behaviour at higher doses [429, 430]. Furthermore, alternative atomistic simulations based on the creation reaction algorithm approach can model very high irradiation doses (approaching reactor-relevant doses) by exploring the steady-state equilibrium microstructure of defects created at longer operational timescales [431], and thus begin to explore

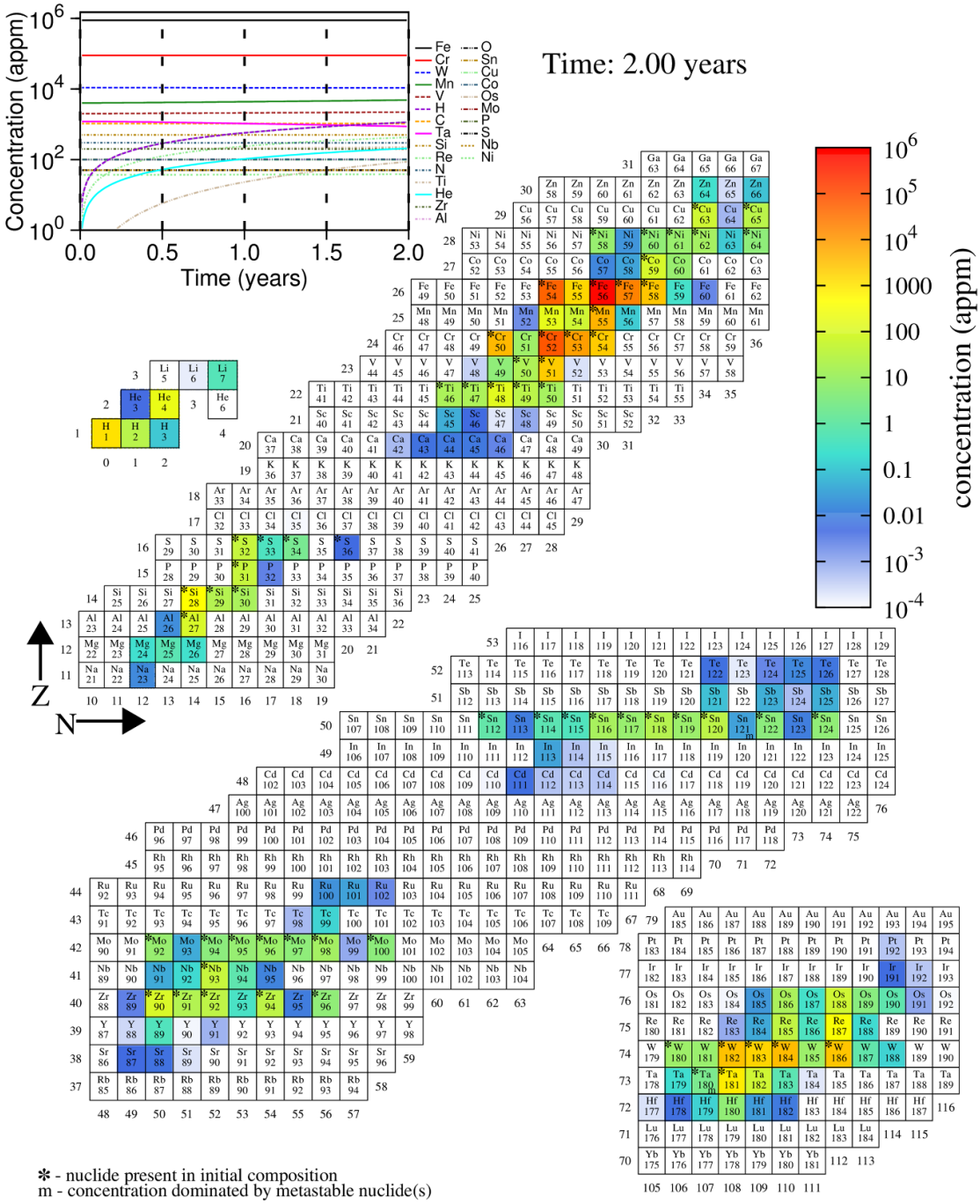

Figure 23. Transmutation response of Eurofer RAFM steel in a typical fusion first-wall environment. The graph and the embedded video show the elemental evolution of the composition during two full power years of exposure in DEMO. The nuclide chart tableau [419] shows the nuclide composition distribution at two years, demonstrating the creation of many additional nuclides not present in the original composition (original nuclides indicated by the * symbol). A video file showing the time evolution of isotopes can be found separately attached.

phenomena that could not previously be explored, such as macroscopic strains [432]. However, despite this progress at the atomistic level, which is a key component of any multiscale modelling framework [419], there is still a gap between capabilities that allow single elements or simple binary systems, such as Fe–Cr, to be modelled, and the fidelity that would be required to consider the full complexity of RAFM steels. A promising avenue that could provide a solution is the use of machine learning to develop descriptions of how atoms interact. First-principles calculations, subject to length scale constraints, can model structures in multi-component alloys such as Fe–Cr–Mn–Ni alloys [433]. But there remains a challenge when using such information to parameterise a potential that can reproduce these density function theory-predicted equilibrium structures and thence provide predictive modelling capabilities for dynamic scenarios. Machine learning has recently been shown capable of bridging the gap between quantum and classical (MD) methods

to provide accurate potentials for other elemental systems for fusion applications such as W [408, 434]. The method demonstrated could be applied to multi-component systems if sufficient training configurations can be generated from first principles, and thus allow for atomistic simulations with predictive modelling capability to support the future development and characterisation of fusion structural steels in multiscale frameworks combining a variety of techniques at various scales.

9. Design challenges for fusion reactors including FNSF

The engineering design of fusion core components, including FW/B structures (RAFM/ODS steels), divertors, radio-frequency launchers and diagnostic apparatus, requires an entirely new approach to assessing viability and reliability in an FNSF. The complex environment of plasma, neutrons and gamma rays, stress, temperature, transmutation products, and magnetic field combined with loading on the functionality of these components creates an enormous challenge to standard engineering approaches. One critical aspect is that fusion in-vessel components will have their material properties degrade over a relatively short time (∼2–5 years), due to both the irradiation environment and their operating conditions—to the point where they must be replaced. This provides some relief to requiring that a component survive for an entire fusion power plant lifetime. However, some components behind those close to the plasma will be lifetime components (e.g. vacuum vessel), and their degradation will have to be much weaker.

For a fusion power plant design to be successful, component design and materials science (including irradiation effects) must be integrated, with non-irradiated and irradiated property data and failure modes feeding into macroscale models with realistic geometries, temperatures and stress-driven thermo-mechanics analysis. Furthermore, correlating microstructural characterisations to macroscopic property changes is essential to producing efficient and accurate projections of component performance throughout its life. A deep fundamental understanding of the various irradiation environments (using ions, fission neutrons and fusion neutrons) is needed to provide a useful translation to accurate predictions of material degradation scenarios. For fusion in-vessel components such as the FW/B, a major complexity is introduced due to the anticipated strong variations in radiation parameters with the distance from the plasma. For example, the neutron dose, He production and H production all vary at different rates through the depth of the blanket. The neutron energy spectra that the fusion core structural materials in FNSF must endure can be seen in figure 24, for the FW, the vacuum vessel and the toroidal field coil case [435]. Here, the 14.1 MeV maximum neutron energy peak is evident, but the FW and regions behind it will experience a broad neutron energy spectrum. In order to show the nuclear impacts, the dpa, He and H production rates through the radial depth of an FNSF blanket modelled using F82H steel are shown in figure 25 [436]. The neutron dose is at a maximum at the FW and decreases with the radial distance into the backend outboard breeding zone. The He production rate decreases much faster than the neutron dose rate, indicating that the FW/B steel structures in FNSF will experience varying He/dpa ratios along the depth from the plasma-facing wall. A similar situation is also anticipated for DEMO [55]. Further, temperature variations are expected based on the differentheating and cooling strategies, and the stresses will vary depending upon the coolant pressure and temperature [54]. Moreover, fusion utilises large permanent magnets to confine the plasma, potentially providing 3–15 T depending on the confinement approach, and it is not clear how the forces due to the magnetic fields will affect irradiation damage evolution. The H production rate inside the steels may become a concern if it is trapped and unable to diffuse out—a situation that might be aggravated in advanced nanostructured steels with high densities of precipitates that can trap gaseous species (like ODS steels).

A consequence of the spatially-dependent dpa and gas production rate is that the corresponding thermo-mechanical properties of the component will vary from location to location as one moves through the blanket. Shown in figure 26 are sections of an FNSF blanket with the Von Mises stress and temperatures, highlighting the significant variations expected throughout the blanket. Due to the difficulty in performing neutron irradiations inside the limited volumes of MTRs with controlled large spatial variations in irradiation parameters and simultaneous applied stresses, robust macroscale constitutive modelling is required that can incorporate such variables to predict FW/B degradation. Recent research to develop constitutive relations for the σ_{YS}, σ_{UTS} and swelling [437–440] show a strong effect of non-uniform dose/gas generation on FNSF's RAFM steel blanket performance [439]. Consistent with the neutron irradiation results, the macroscale modelling shows severe hardening of the blanket for temperatures <400 °C (expected at the backend) over a range of doses up to 80 dpa, and softening for temperatures >400 °C (towards the plasma-facing end) [439]. Such spatially varying material properties will significantly re-distribute stresses in the blanket calculated in the absence of irradiation. When the depth-dependent non-uniform neutron dose is incorporated, a drastic modification of stress states and deformation modes in the RAFM steel blanket sub-model can occur as compared to the results when through thickness uniform irradiation parameters are assumed [439]. The spatially-dependent swelling and plasticity parameters because of the steep gradient in

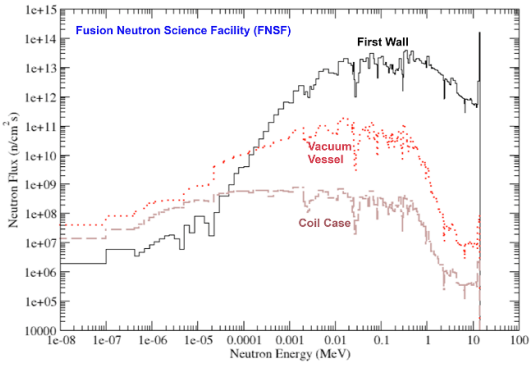

Figure 24. Neutron energy spectra in the outboard first wall, the vacuum vessel, and the toroidal field magnet coil case for the FNSF design [54], showing the significant attenuation of neutrons and broadening of their energy spectra (adapted from [435]). Courtesy of L El-Guebaly, University of Wisconsin–Madison.

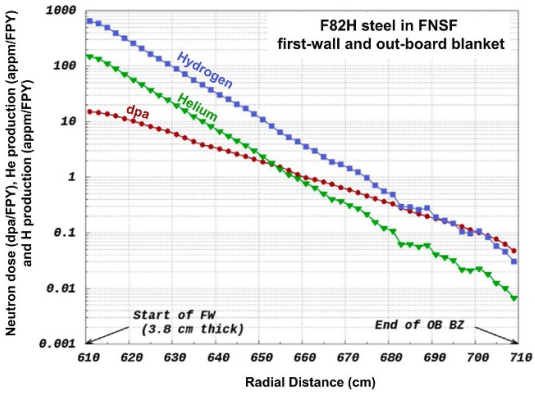

Figure 25. Radial distribution of dpa, He and H production versus depth into the outboard (OB) blanket of FNSF, in F82H steel, showing the strong gradient in production rate of these quantities. FPY = full power year, FW = first wall, BZ = breeding zone. Reprinted from [436], copyright (2018), with permission from Elsevier. CC BY-NC-ND 4.0.

neutron dose and He generation rate in an FNSF blanket module (∼14.8 dpa yr^{-1} at FW, dropping to 0.24 dpa yr^{-1} at the back end) are expected to cause displacement gradients in the blanket (figure 27). Consequentially, the stress and effective plastic strain of the blanket increases as compared to assuming uniform irradiation conditions, thereby necessitating thorough failure mode analysis of individual blanket sections separately [439]. These efforts are critical to allow proper thermo-mechanical design of fusion core components. However, the constitutive models are inherently reliant upon robust experimental data under relevant exposure conditions as input to ensure accurate predictions. Since the microstructure features after irradiation determine the large-scale properties, understanding the specific microstructural defect feature's impact on the property changes is needed to develop a bottom-up approach for designing fusion components. The characteristics of the microstructural features will likely be influenced by the variables present in the exposure conditions, including gradients in stress, temperature and gas production rates (and potentially magnetic field) that currently require experimental validation under neutron irradiation conditions to support empirical constitutive models for property prediction.

The more advanced variants of RAFM steels utilising a high density of precipitates have been shown to sequester He [190, 269, 302] and also simultaneously benefit from higher strength as a function of temperature [355]. A major benefit of such advanced steel variants is that the component lifetime (characterised by maximum allowable dpa and He-induced property degradation) may be longer and higher stress levels may be sustained at the upper end of the operating temperature range. This latter property can potentially allow higher operating temperatures that will improve the thermal conversion efficiencies for electricity generation. The maximum component lifetime will also determine how often the fusion core components are replaced, which is expected to require a major remote maintenance activity that will (a) be costly, (b) impact power-plant availability and (c) affect the radioactive waste volume produced.

Other environmental factors like corrosion can ultimately compromise the material integrity in any of the fusion in-vessel components. For both the lead–lithium liquid metal breeder and the lithium ceramic oxide solid breeder concepts, corrosion remains an issue with the RAFM steels [441–443]. Since the

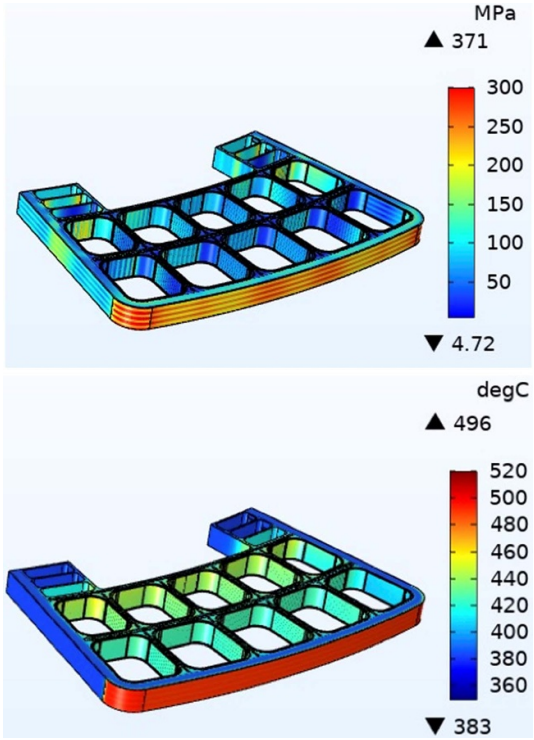

Figure 26. Von Mises stress (top) and temperature (bottom) for a section of the RAFM steel inboard blanket for the FNSF [54]. Variations throughout the blanket will create differing background fields within the materials. On the stress figure, the striations are from high pressure helium coolant channels.

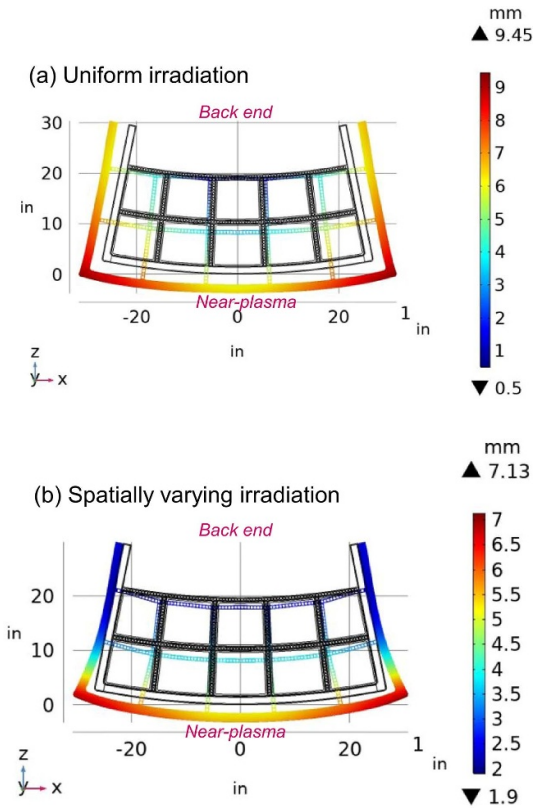

Figure 27. Effect of spatially varying dose and swelling on displacement gradients of free side walls in an FNSF blanket sub-model designed from F82H steel. (a) Case of uniform irradiations up to 90 dpa and uniform swelling. (b) Spatially varying swelling and neutron dose—14.8 dpa yr^{-1} in FW near-plasma region and progressively dropping to 0.24 dpa yr^{-1} at the back end (88.9 dpa to 1.4 dpa). Reprinted from [440], copyright (2021), with permission from Elsevier.

mechanisms are chemical, the temperature plays a central role and can limit maximum operating temperatures based on phenomena occurring at the solid–solid or solid–liquid material interface. In the case of a liquid breeder, the flow speed and magnetic field are also important factors [79], and for the solid breeders the chemical composition of the purge gas will be important. The 9%Cr-based RAFM steels are 'stainless FM steels' that benefit from corrosion resistance due to the protective Cr_2O_3 (chromia) layer on the surface. But Al_2O_3 (alumina)-rich protective surface layers in steels show improved corrosion resistance in general, and specifically in lead–lithium environments [444, 445]. Based on this well-known behaviour, Al-added steels using the Fe–Cr–Al system hold promise to mitigate corrosion issues in fusion environments. A metallurgical limitation is that both Cr and Al are ferrite stabilisers, resulting in a body-centered cubic (bcc) ferritic microstructure up to the melting point. In the absence of α–γ phase transition, Fe–Cr–Al-based steels may not obtain a tempered martensitic structure. In other words, fusion steels for enhanced corrosion resistance may either rely on a fully ferritic Fe–Cr–Al-based matrix (including Fe–Cr–Al-ODS) [445, 446] or RAFM steels with deposited Al coatings [447–449]. With the lack of neutron data, such materials require systematic evaluation under fusion-relevant irradiation conditions. It should be noted that blanket designs are complex, and will often have other integrated materials for various functionalities, such as thermal and/or electrical insulators, coolant channels (expected to be ceramics like SiC), tritium permeation barriers/corrosion barriers, and fluids (e.g. lead–lithium) that may collectively create a complex situation where they allow degrading interactions between the different material types that needs to be understood (e.g. ferritic steel and SiC [450]).

At the first-wall surface facing the burning plasma, it is typical for a low physical sputtering and high melting temperature material to be used (e.g. tungsten), which will be adhered to an RAFM structure of a blanket or radio-frequency launcher, for example [1, 54, 451, 452]. These layers are thin, ∼0.2 mm, but provide protection against plasma transients, and otherwise do not significantly affect the structural or thermal performance of the component. However, the interface between RAFM structures and thin layers such as of tungsten under various loading conditions may degrade, and their behaviour in a neutron environment is entirely unknown. Due to the difficulty in joining tungsten to an RAFM steel substrate, long-term research requires developing graded materials to remove the interface and improve the thermal properties of the structure (e.g. thermal conductivity). In fact, RAFM steel's rather low thermal conductivity makes it challenging to design efficient cooling structures in the first wall of a blanket or a divertor, that can handle multi-MW m^{-2} heat loading due to the combination of structural needs of pressurised coolants, operating material temperature limits, and coolant properties. Although many refractory metals have better thermal properties, they are typically not acceptable materials for structural loading. It should be noted that tungsten is expected to receive lower dpa and lower He and H production rates relative to RAFM steels (5 dpa, 2.5 appm He, 10 appm H per full power year at the first wall).

Overall, structural materials for the fusion core including the FW/B necessitate the development as a combined effort between materials science and engineering design, involving thermo-mechanics, coolant thermohydraulics, tritium behaviour and neutronics. Simple design criteria are likely to become challenged by the strong interactions of an evolving material and multi-element environment, although they may remain the first step in design in any material-design qualification efforts. It is paramount that at least thermo-mechanics include irradiated property data of structural materials such as RAFM steels in design assessments as a routine, and that the fusion materials database is established even if it is an early manifestation of an engineering qualified database.

10. Conclusions and recommendations

(a) ***Understanding irradiation hardening*:** RAFM steels offer better radiation tolerance, such as void-swelling resistance, as compared to austenitic steels. One of the biggest technical challenges is associated with LTHE under irradiation for operating conditions envisaged in all blanket concepts. LTHE results in an increase in hardness/yield stress (σ_{YS}), severe loss of tensile ductility, loss of strain-hardening capacity, reduction in necking ductility, and a loss of FT with the shift in DBTT to higher values. This phenomenon, which is most severe for $T_{irr} < 400$ °C and rises sharply for $T_{irr} \leqslant 350$ °C, is historically attributed to the dislocation loops; but neutron-irradiated microstructure results increasingly show the non-negligible deleterious contribution of irradiation-induced/enhanced clustering of alloying elements such as Mn–Si–P, along with Cr. Quantification of chemical phenomena under irradiation is therefore essential to develop a proper fundamental understanding of LTHE in this class of materials, necessitating irradiation research guided by advanced characterisation, mechanical property testing and multiscale modelling. Under tensile loading conditions, irradiation hardening saturates around ∼15 dpa in RAFM steels, highlighting better performance compared to conventional FM steels that show signs of saturation at doses of >30–40 dpa when $T_{irr} < 350$ °C. Similar to the

saturation in hardening, DBTT shift also saturates with neutron dose and it roughly correlates well with σ_{YS} increase of RAFM steels.

(b) ***Test temperature effect on hardening*:** Irradiation hardening, measured as an absolute or percentage increase in yield stress (σ_{YS}), is not only a function of the neutron dose and irradiation temperature but also depends on the test temperature—higher hardening will be measured at lower test temperatures, highlighting that a fixed value of $\Delta\sigma_{YS}$ must not be assumed over the envisaged range of FW/B operating temperatures.

(c) ***Loss of ductility*:** The total elongation in RAFM steels remains acceptable (∼5%) up to higher doses (>70 dpa). The uniform elongation reduces severely for doses as low as ∼0.5–1 dpa and saturates at very low values (<0.5%–1%) by ∼3–4 dpa. This means the primary ductility remaining in irradiated RAFM steels is necking ductility. The tensile failures remain largely ductile with high (>50%) RA values for doses >70 dpa.

(d) ***RAFM steels alloy design strategy to minimise LTHE*:** To minimise LTHE including the problem of immediate flow localisation, alloy development should focus on designing steels with a large separation between the σ_{YS} and plastic instability stress (σ_{PIS}) to ensure a large work hardening margin and uniform deformation capability are retained after irradiation. If LTHE improvement is the primary goal, then improvements in σ_{PIS} should not be achieved at the cost of highly increased σ_{YS}. While harder RAFM steels typically show better creep properties, their FT before/after irradiation will generally be poor, meaning a poorer LTHE performance. Moreover, the concentrations of elements prone to radiation-induced clustering/segregation such as Mn–Si–P should be minimised in the steels.

(e) ***LTHE in ODS steels*:** The FT of current-generation ODS steels in non-irradiated conditions is typically worse than that of RAFM steels. After neutron irradiations, the ODS steels are not as highly resistant to LTHE as sometimes claimed. Depending upon the details of the alloy, these materials can harden nearly as much or even higher than RAFM steels under neutron irradiation, especially at higher doses >40 dpa and up to ∼80 dpa. An emerging concern is that recent neutron irradiation results show significant hardening in 12%–20% Cr ODS steels after neutron irradiation for temperatures as high as 400 °C–500 °C, where RAFM steels do not typically show much of an LTHE problem. The higher retained hardening in ODS steels reflects the relatively worse FT properties after irradiation, due to which it is likely that the lower operational temperature limit envisaged for thick-walled ODS components may have to be higher than 350 °C. This may pose a significant design challenge because the safe operational temperature window envisaged for ODS steels may shrink for fusion applications. Many of the LTHE issues reported in the literature appear to be associated with solute additions (not directly an ODS particle phenomenon), although there are some synergistic nucleation effects. For example, the reason for the higher retained hardening in ODS steels originates from radiation-accelerated phase instabilities in the alloys, including the formation of embrittling Cr-rich α' precipitates and co-clustering of other alloying elements to form other embrittling phases (such as the Ni–Ti, Al–Ti or χ phase).

(f) ***Need for additional neutron irradiations on ODS steels and interlinked alloy designs*:** Data on LTHE in ODS steels are still largely sparse compared to FM steels, and dedicated future experimental studies are needed. With advanced characterisation techniques, emerging neutron irradiation data also suggest significant deterioration of the oxide particles after neutron irradiations. A fundamental understanding of the effect of oxide particle deterioration (combined with the effects of phase instabilities) on ODS steels' thermo-mechanical properties is needed in future studies. For ODS alloy design, minimisation of LTHE susceptibility should be targeted, which means a lean ODS steel is the likely the path forward—the Cr concentration should be reduced (8%–10%) to minimise the α' embrittlement, and the concentration of other elements that could cluster under irradiation should also be minimised in conjunction. In addition to the LTHE problem, questions remain regarding tritium retention due to trapping by nanofeatures in ODS steels (and high sink strength materials in general). This may pose risks to fusion power plant design if tritium is unable to diffuse out—raising safety concerns.

(g) ***Helium effect on LTHE*:** The influence of He on the thermo-mechanical properties of RAFM steels remains an open question, primarily due to the difficulty in generating fusion-relevant He/dpa ratios inside fission reactors. A proper understanding of the effect of He on the LTHE performance is needed. Data from SPN sources suggest an additional increase in σ_{YS} up to higher irradiation temperatures and an additional DBTT shift due to He co-generation. While SPN irradiations have generated the first-step valuable data towards addressing the He challenge, the reported results require scrutiny and unbiased validation using MTR irradiations or when a 14 MeV neutron source becomes available because of the well-known temperature excursions reported in SPN irradiations combined with results showing solid spallation products forming in RAFM steels (that may affect the mechanical properties). The threshold He concentrations that could worsen the LTHE scenario for RAFM steels are not well established due to

discrepancies between the SPN data and recent results obtained from the isotopic doping technique in MTR irradiations.

(h) ***Isotopic tailoring approach to study He effect*:** In the absence of a 14 MeV source, isotopic tailoring such as with ^{54}Fe or tuning ^{58}Ni/^{60}Ni ratios is a viable method to stimulate He generation using mixed spectrum fission reactors to develop the foundational neutron effects science for later validation with a 14 MeV source. The properties of isotopically doped and non-isotopically tailored steels, however, should not be directly compared to extract the effect of He. The irradiated materials are only comparable when two isotopes—one that produces He while the other does not produce He—are studied simultaneously (to separate any effects of chemistry modification by isotopic tailoring on the irradiation performance).

(i) ***Unknown effect of applied stress on steel performance*:** A major challenge in quantifying the effect of He on the overall properties of RAFM/ODS steels is the absence of applied stresses during irradiation, especially during in-pile neutron irradiation experiments. While some progress has been made on innovative capsule designs facilitating stress application inside MTRs, dedicated research is needed to advance the state of the art in stress application. Future research should target experiments to map the dose–temperature–He-stress scenarios to the performance of fusion structural steels.

(j) ***Susceptibility to HTHE is an open question*:** The lack of applied stresses during neutron irradiations is also one of the key reasons why the susceptibility of RAFM steels to high-temperature He embrittlement (HTHE) is not well evaluated. While it is generally accepted that RAFM steels may not suffer from HTHE, this conclusion is derived from irradiations without applied stress or with cyclotron-based He implantation plus in-beam creep experiments that may not accurately represent the bulk performance because of the shallow He implantation depths. In general, the effect of He on both fast fracture properties and on slow-strain rate deformation, including creep, needs to be evaluated in the entire temperature range of the blanket operations. These experiments are also necessary for emerging variants of RAFM steels that are tuned for high-temperature creep properties having much higher hardness in non-irradiated conditions than conventional Gen-I RAFM steels. Being already much harder may deteriorate the hardening embrittlement properties faster due to the potential effects of transmutation-induced gases. Neutron damage scenarios on mechanical properties, including the effects of He or H, are entirely missing from advanced RAFM steels such as CNA alloys.

(k) ***Cavity-swelling scenarios*:** While the cavity-swelling performance of RAFM steels is better compared to austenitic steels, additional research is needed to quantify the swelling in neutron environments in the intermediate temperature range (∼400 °C–500 °C). Furthermore, the effects of the He/dpa ratio and the additional synergistic contribution of H on swelling and swelling–creep fatigue interaction under neutron irradiation are not fully quantified. These experiments are necessary for a proper design evaluation of the FW/B. The requirement for bulk swelling and thermo-mechanical property degradation data to predict blanket performance mandates a focus on neutron irradiation testing, including the effects of transmutation gases. Cavity swelling is not expected to be a major issue for ODS steels.

(l) ***High-temperature creep performance*:** While irradiation creep may play a negligible role in the blanket performance, the thermal creep performance of Gen-I RAFM steels is inadequate to ensure operations beyond ∼550 °C. Recent progress was achieved in improving the creep properties by (a) TMTs, (b) using a combination of TMTs with chemistry modification including boron addition, (c) optimisation of chemistry processing to nucleate a high density of MX particles in advanced alloys like CNA alloys. The behaviour under neutron irradiation of such creep-resistant alloys needs investigation in the entire temperature range of FW/B operations. Qualification of advanced RAFM/ODS steels is necessary for application in later stages of DEMO or FNSF (beyond 20 dpa) where Gen-I RAFM steels may not be suitable.

(m) ***Creep–fatigue*:** Creep–fatigue interactions under irradiation that will ultimately control the upper operating temperature of RAFM/ODS steels are entirely unknown. Similarly, swelling–creep–fatigue synergies and with the added effect of transmutation gases also remain to be evaluated for fusion structural steels.

(n) ***Tritium management*:** Tritium management is essential to minimise tritium loss, release to the environment and minimise the tritium inventory in the fusion reactor. High sink strength materials such as ODS steels are superior for He management but tend to trap more tritium than RAFM steels due to the lower diffusivity of hydrogen in these materials. This is due to the positive interaction and trapping of hydrogen with a high density of grain boundaries (due to the smaller grain sizes in ODS steels), dislocations and most importantly trapping by the high density of nano-dispersoids. Future engineering and safety case studies are needed for ODS steels and emerging advanced high sink strength varieties of RAFM steels like CNA alloys to evaluate what level of tritium build-up is acceptable for the

FW/B structures in these materials. Furthermore, a fundamental understanding of tritium trapping and build-up in these materials needs to be established in the presence of neutron damage (especially during nanoscale cavity formation), which also requires dedicated future studies.

(o) ***Multiscale approach to fusion component design (including for FNSF)*:** Fusion reactor in-vessel component design requires a multiscale approach where the microstructural changes due to neutron damage and transmutation-induced gas production are established and translated up to macroscopic property changes. This multi-length scale translation requires irradiation experiments combined with advanced characterisation, feeding experimental input into microscopic models that will inform macroscopic continuum models. The multiscale approach is necessary to cover the full range of time and length scales of defect formation, and key events to address all relevant bulk failure mechanisms. Modelling activities are additionally necessary due to the difficulty in performing neutron irradiation experiments inside MTRs that can also include the potential effects of stress such as from primary loads (from coolant pressure), secondary loads (from thermal gradients), spatial variation in damage levels and gas production rates, and relevant transients.

Data availability statement

All data that support the findings of this study are included within the article (and any supplementary files).

Acknowledgments

The authors thank Yutai Katoh and David Hoelzer for their fruitful scientific discussions.

Funding

This study was supported by the US Department of Energy, Office of Fusion Energy Sciences and Laboratory Directed Research and Development Program of Oak Ridge National Laboratory under Contract DE-AC05-00OR22725 with ORNL managed by UT Battelle, LLC. MRG acknowledges funding from the RCUK Energy Programme (Grant Number EP/T012250/1).

ORCID iDs

Arunodaya Bhattacharya https://orcid.org/0000-0001-5711-7443
Mark R Gilbert https://orcid.org/0000-0001-8935-1744

References

[1] Boutard J L, Alamo A, Lindau R and Rieth M 2008 Fissile core and tritium-breeding blanket: structural materials and their requirements *C. R. Phys.* **9** 287–302
[2] Zinkle S J *et al* 2014 Fusion materials science and technology research opportunities now and during the ITER era *Fusion Eng. Des.* **89** 1579–85
[3] Tan L, Katoh Y, Tavassoli F, Henry J, Rieth M, Sakasegawa H, Tanigawa H and Huang Q 2016 Recent status and improvement of reduced-activation ferritic-martensitic steels for high-temperature service *J. Nucl. Mater.* **479** 515–23
[4] Baluc N, Schäublin R, Spätig P and Victoria M 2004 On the potentiality of using ferritic/martensitic steels as structural materials for fusion reactors *Nucl. Fusion* **44** 56–61
[5] Tanigawa H, Gaganidze E, Hirose T, Ando M, Zinkle S J, Lindau R and Diegele E 2017 Development of benchmark reduced activation ferritic/martensitic steels for fusion energy applications *Nucl. Fusion* **57** 092004
[6] Bloom E E, Conn R W, Davis J W, Gold R E, Little R, Schultz K R, Smith D L and Wiffen F W 1984 Low activation materials for fusion applications *J. Nucl. Mater.* **122** 17–26
[7] Klueh R L and Harries D R 2001 *High-Chromium Ferritic and Martensitic Steels for Nuclear Applications* (Bridgeport: ASTM)
[8] Zhong W and Tan L 2020 Radiological analysis and transmutation calculation of representative castable nanostructured alloys *Fusion Eng. Des.* **160** 111899
[9] Wiffen F and Santoro R 1983 Control of activation levels to simply waste management of fusion reactor ferritic steel components *Proc. Topical Conf. on Ferritic Alloys for Use in Nuclear Energy Technology* (Snowbird, UT: TMS/AIME)
[10] Klueh R L and Bloom E E 1985 The development of ferritic steels for fast induced-radioactivity decay for fusion reactor applications *Nucl. Eng. Des. Fusion* **2** 383–9
[11] Klueh R L, Gelles D S and Lechtenberg T A 1986 Development of ferritic steels for reduced activation: the US program *J. Nucl. Mater.* **141–143** 1081–7
[12] Tamura M, Hayakawa H, Tanimura M, Hishinuma A and Kondo T 1986 Development of potential low activation ferritic and austenitic steels *J. Nucl. Mater.* **141–143** 1067–73
[13] Dulieu D, Tupholme K W and Butterworth G J 1986 Development of low-activation martensitic stainless steels *J. Nucl. Mater.* **141–143** 1097–101
[14] Klueh R L and Nelson A T 2007 Ferritic/martensitic steels for next-generation reactors *J. Nucl. Mater.* **371** 37–52
[15] Gelles D 1990 Effects of irradiation on low activation ferritic alloys: a review *Reduced Activation Materials for Fusion Reactors* (West Conshohocken, PA: ASTM International) pp 113–7

[16] Tan L, Snead L L and Katoh Y 2016 Development of new generation reduced activation ferritic-martensitic steels for advanced fusion reactors *J. Nucl. Mater.* **478** 42–49
[17] Noda T, Abe F, Araki H and Okada M 1986 Development of low activation ferritic steels *J. Nucl. Mater.* **141–143** 1102–6
[18] Kimura A, Kayano H, Misawa T and Matsui H 1994 Designation of alloy composition of reduced-activation martensitic steel *J. Nucl. Mater.* **212–215** 690–4
[19] Kohyama A, Kohno Y, Asakura K and Kayano H 1994 R&D of low activation ferritic steels for fusion in japanese universities *J. Nucl. Mater.* **212–215** 684–9
[20] Shiba K, Tanigawa H, Hirose T and Nakata T 2012 Development of the toughness-improved reduced-activation F82H steel for demo reactor *Fusion Sci. Technol.* **62** 145–9
[21] Tupholme K W, Dulieu D and Butterworth G J 1988 The development of low-activation martensitic 9 and 11%Cr,W,V stainless steels for fusion reactor applications *J. Nucl. Mater.* **155–157** 650–5
[22] Ehrlich K, Kelzenberg S, Röhrig H D, Schäfer L and Schirra M 1994 The development of ferritic-martensitic steels with reduced long-term activation *J. Nucl. Mater.* **212–215** 678–83
[23] Van der Schaaf B, Tavassoli F, Fazio C, Rigal E, Diegele E, Lindau R and LeMarois G 2003 The development of EUROFER reduced activation steel *Fusion Eng. Des.* **69** 197–203
[24] Terentyev D, Puype A, Kachko O, Van Renterghem W and Henry J 2021 Development of RAFM steel for nuclear applications with reduced manganese, silicon and carbon content *Nucl. Mater. Energy* **29** 101070
[25] Pilloni L, Cristalli C, Tassa O, Bozzetto L, Zanin E and Bettocchi N 2019 Development of innovative materials and thermal treatments for DEMO water cooled blanket *Nucl. Mater. Energy* **19** 79–86
[26] Rieth M, Fernandez P, Henry J, Hoffmann J, Pilloni L, Puype A and de Wispelaere N 2015 *The EUROfusion Program on 9CrWVTa Steels, MatISSE/JPNM Workshop on Cross-Cutting Issues in Structural Materials R&D for Future Energy Systems*
[27] Hoffmann J, Rieth M, Klimenkov M and Baumgärtner S 2018 Improvement of EUROFER's mechanical properties by optimized chemical compositions and thermo-mechanical treatments *Nucl. Mater. Energy* **16** 88–94
[28] Huang Q *et al* 2013 Recent progress of R&D activities on reduced activation ferritic/martensitic steels *J. Nucl. Mater.* **442** S2–S8
[29] Huang Q *et al* 2011 Progress in development of CLAM steel and fabrication of small TBM in China *J. Nucl. Mater.* **417** 85–88
[30] Raj B, Rao K B S and Bhaduri A K 2010 Progress in the development of reduced activation ferritic-martensitic steels and fabrication technologies in India *Fusion Eng. Des.* **85** 1460–8
[31] Raju S, Jeya Ganesh B, Rai A K, Mythili R, Saroja S, Mohandas E, Vijayalakshmi M, Rao K B S and Raj B 2009 Measurement of transformation temperatures and specific heat capacity of tungsten added reduced activation ferritic–martensitic steel *J. Nucl. Mater.* **389** 385–93
[32] Leonteva-Smirnova M V, Ioltukhovskiy A G, Arutiunova G A, Tselischev A V and Chernov V M 2002 Investigation of heat treatment conditions on the structure of 12% chromium reduced activation steels *J. Nucl. Mater.* **307–311** 466–70
[33] Chernov V M *et al* 2007 Structural materials for fusion power reactors—the RF R&D activities *Nucl. Fusion* **47** 839
[34] Chun Y B, Kang S H, Noh S, Kim T K, Lee D W, Cho S and Jeong Y H 2014 Effects of alloying elements and heat treatments on mechanical properties of Korean reduced-activation ferritic–martensitic steel *J. Nucl. Mater.* **455** 212–6
[35] Cho S, Kim D H and Ahn M Y 2009 Development of low activation ferritic/martensitic steel welding technology for the fabrication of KO HCSB TBM *J. Nucl. Mater.* **386–388** 491–4
[36] Chun Y B, Choi B K, Han C H, Lee D W, Cho S, Kim T K and Jeong Y H 2012 Development of reduced activation ferritic-martensitic steels in South Korea *Transactions of the Korean Nuclear Society Spring Meeting* (*Jeju*)
[37] Klueh R, Hashimoto N and Sokolov M 2004 Effect of heat treatment and tantalum on microstructure and mechanical properties of Fe–9Cr–2W–0.25V steel *J. ASTM Int.* **1** 11337
[38] Tanigawa H, Shiba K, Möslang A, Stoller R E, Lindau R, Sokolov M A, Odette G R, Kurtz R J and Jitsukawa S 2011 Status and key issues of reduced activation ferritic/martensitic steels as the structural material for a DEMO blanket *J. Nucl. Mater.* **417** 9–15
[39] Raj B and Vijayalakshmi M 2012 Ferritic steels and advanced ferritic-martensitic steels *Comprehensive Nuclear Materials* vol 4, ed R J M Konings and R E Stoller (Oxford: Elsevier) pp 97–121
[40] Kohyama A, Hishinuma A, Kohno Y, Shiba K and Sagara A 1998 The development of ferritic steels for DEMO blanket *Fusion Eng. Des.* **41** 1–6
[41] Lucon E and Vandermeulen W 2009 Overview of the tensile properties of EUROFER in the unirradiated and irradiated conditions *J. Nucl. Mater.* **386–388** 254–6
[42] Ehrlich K, Dietz W, Kohyama A, Hishinuma A, Gelles D S S, Klueh R L L, Dietz W and Ehrlich K 1996 Low-activation ferritic and martensitic steels for fusion application *J. Nucl. Mater.* **233–237** 138–47
[43] Hishinuma A, Kohyama A, Klueh R L, Gelles D S, Dietz W and Ehrlich K 1998 Current status and future R&D for reduced-activation ferritic/martensitic steels *J. Nucl. Mater.* **258–263** 193–204
[44] Tavassoli F 2013 Eurofer steel, development to full code qualification *Proc. Eng.* **55** 300–8
[45] Gaganidze E, Aktaa J, Karlsruher J A and Aktaa J 2013 Assessment of neutron irradiation effects on RAFM steels *Fusion Eng. Des.* **88** 118–28
[46] Sakasegawa H, Tanigawa H, Hirose T, Kato T and Nozawa T 2020 Material strength standard of F82H for RCC-MRx *Fusion Eng. Des.* **161** 111952
[47] Salavy J F, Boccaccini L V, Chaudhuri P, Cho S, Enoeda M, Giancarli L M, Kurtz R J, Luo T Y, Rao K B S and Wong C P C 2010 Must we use ferritic steel in TBM? *Fusion Eng. Des.* **85** 1896–902
[48] Stork D, Heidinger R, Muroga T, Zinkle S J, Moeslang A, Porton M, Boutard J L, Gonzalez S and Ibarra A 2017 Towards a programme of testing and qualification for structural and plasma-facing materials in 'fusion neutron' environments *Nucl. Fusion* **57** 092013
[49] Bhattacharya A and Zinkle S J 2020 Cavity swelling in irradiated materials *Comprehensive Nuclear Materials* vol 1, ed R Konings and R E Stoller (Oxford: Elsevier) pp 406–55
[50] Zinkle S J and Snead L L 2014 Designing radiation resistance in materials for fusion energy *Annu. Rev. Mater. Res.* **44** 241–67
[51] Rowcliffe A F, Kessel C E, Katoh Y, Garrison L M, Tan L, Yamamoto Y and Wiffen F W 2018 Materials-engineering challenges for the fusion core and lifetime components of the fusion nuclear science facility *Nucl. Mater. Energy* **16** 82–7
[52] Federici G *et al* 2018 DEMO design activity in Europe: progress and updates *Fusion Eng. Des.* **136** 729–41
[53] Federici G, Biel W, Gilbert M R, Kemp R, Taylor N and Wenninger R 2017 European DEMO design strategy and consequences for materials *Nucl. Fusion* **57** 092002
[54] Kessel C E *et al* 2018 Overview of the fusion nuclear science facility, a credible break-in step on the path to fusion energy *Fusion Eng. Des.* **135** 236–70

[55] Gilbert M R, Dudarev S L, Zheng S, Packer L W and Sublet J-C 2012 An integrated model for materials in a fusion power plant: transmutation, gas production, and helium embrittlement under neutron irradiation *Nucl. Fusion* **52** 083019
[56] Gilbert M R and Sublet J C 2017 Scoping of material response under DEMO neutron irradiation: comparison with fission and influence of nuclear library selection *Fusion Eng. Des.* **125** 299–306
[57] Zinkle S J and Was G S 2013 Materials challenges in nuclear energy *Acta Mater.* **61** 735–58
[58] Zinkle S J and Ghoniem N M 2000 Operating temperature windows for fusion reactor structural materials *Fusion Eng. Des.* **51–52** 55–71
[59] Federici G, Boccaccini L, Cismondi F, Gasparotto M, Poitevin Y and Ricapito I 2019 An overview of the EU breeding blanket design strategy as an integral part of the DEMO design effort *Fusion Eng. Des.* **141** 30–42
[60] Gaganidze E, Petersen C, Materna-Morris E, Dethloff C, Weiß O J, Aktaa J, Povstyanko A, Fedoseev A, Makarov O and Prokhorov V 2011 Mechanical properties and TEM examination of RAFM steels irradiated up to 70 dpa in BOR-60 *J. Nucl. Mater.* **417** 93–98
[61] Aiello G, Aktaa J, Cismondi F, Rampal G, Salavy J F and Tavassoli F 2011 Assessment of design limits and criteria requirements for Eurofer structures in TBM components *J. Nucl. Mater.* **414** 53–68
[62] Rieth M *et al* 2021 Technological aspects in blanket design Effects of micro-alloying and thermo-mechanical treatments of EUROFER97 type steels after neutron irradiation *Fusion Eng. Des.* **168** 112645
[63] Bhattacharya A, Chen X, Graening T, Reed J, Geringer J W and Kato Y 2020 *Post-Irradiation Examination of Eurofer97 Steel Variants Irradiated to 2.5 dpa, ∼300 °C, ORNL/SPR-2020/1440* (Oak Ridge, TN: Oak Ridge National Lab)
[64] Chen X, Clowers L N, Graening T, Bhattacharya A, Campbell A A, Robertson J, Geringer J W, Sokolov M A, Katoh Y and Rieth M 2020 Post-irradiation evaluation of eurofer97 fracture toughness using miniature multinotch bend bar specimens *Am. Soc. Mech. Eng. Press. Vessels Pip. Div. (Publ.) PVP* **1** 1–8
[65] Yamamoto T, Odette G R, Kishimoto H, Rensman J W and Miao P 2006 On the effects of irradiation and helium on the yield stress changes and hardening and non-hardening embrittlement of ∼8Cr tempered martensitic steels: compilation and analysis of existing data *J. Nucl. Mater.* **356** 27–49
[66] Bhattacharya A *et al* 2021 Irradiation hardening and ductility loss of Eurofer97 steel variants after neutron irradiation to ITER-TBM relevant conditions *Fusion Eng. Des.* **173** 112935
[67] Del Nevo A *et al* 2017 WCLL breeding blanket design and integration for DEMO 2015: status and perspectives *Fusion Eng. Des.* **124** 682–6
[68] Cabet C, Dalle F, Gaganidze E, Henry J and Tanigawa H 2019 Ferritic-martensitic steels for fission and fusion applications *J. Nucl. Mater.* **523** 510–37
[69] Tavassoli A-A F, Rensman J-W, Schirra M and Shiba K 2002 Materials design data for reduced activation martensitic steel type F82H *Fusion Eng. Des.* **61–62** 617–28
[70] Zinkle S J, Boutard J L, Hoelzer D T, Kimura A, Lindau R, Odette G R, Rieth M, Tan L and Tanigawa H 2017 Development of next generation tempered and ODS reduced activation ferritic/martensitic steels for fusion energy applications *Nucl. Fusion* **57** 092005
[71] Yu G, Nita N and Baluc N 2005 Thermal creep behaviour of the EUROFER 97 RAFM steel and two European ODS EUROFER 97 steels *Fusion Eng. Des.* **75–79** 1037–41
[72] Konobeev Y, Dvoriashin A, Porollo S, Shulepin S, Budylkin N, Mironova E and Garner F 2004 Irradiation creep and swelling of Russian ferritic-martensitic steels irradiated to very high exposures in the BN-350 fast reactor at 305–335 °C *J. ASTM Int.* **1** 11342
[73] Henry J and Maloy S A 2017 Irradiation-resistant ferritic and martensitic steels as core materials for generation IV nuclear reactors *Structural Materials for Generation IV Nuclear Reactors* (Cambridge: Elsevier) pp 329–55
[74] Klueh R L, Hashimoto N and Maziasz P J 2005 Development of new nano-particle-strengthened martensitic steels *Scr. Mater.* **53** 275–80
[75] Hollner S, Piozin E, Mayr P, Caës C, Tournié I, Pineau A and Fournier B 2013 Characterization of a boron alloyed 9Cr3W3CoVNbBN steel and further improvement of its high-temperature mechanical properties by thermomechanical treatments *J. Nucl. Mater.* **441** 15–23
[76] Sachadel U A, Morris P F and Clarke P D 2013 Design of 10%Cr martensitic steels for improved creep resistance in power plant applications *Mater. Sci. Technol.* **29** 767–74
[77] Hollner S, Fournier B, le Pendu J, Cozzika T, Tournié I, Brachet J C and Pineau A 2010 High-temperature mechanical properties improvement on modified 9Cr–1Mo martensitic steel through thermomechanical treatments *J. Nucl. Mater.* **405** 101–8
[78] Boccaccini L V *et al* 2016 Objectives and status of EUROfusion DEMO blanket studies *Fusion Eng. Des.* **109–111** 1199–206
[79] Malang S, Raffray A R and Morley N B 2009 An example pathway to a fusion power plant system based on lead-lithium breeder: comparison of the dual-coolant lead-lithium (DCLL) blanket with the helium-cooled lead-lithium (HCLL) concept as initial step *Fusion Eng. Des.* **84** 2145–57
[80] Nogami S, Hasegawa A and Yamazaki M 2020 Fatigue properties of ferritic/martensitic steel after neutron irradiation and helium implantation *Nucl. Mater. Energy* **24** 100764
[81] Mahler M and Aktaa J 2018 Eurofer97 creep-fatigue assessment tool for ANSYS APDL and workbench *Nucl. Mater. Energy* **15** 85–91
[82] Vorpahl C, Möslang A and Rieth M 2011 Creep–fatigue interaction and related structure property correlations of EUROFER97 steel at 550 °C by decoupling creep and fatigue load *J. Nucl. Mater.* **417** 16–19
[83] Materna-Morris E, Möslang A and Schneider H C 2013 Tensile and low cycle fatigue properties of EUROFER97-steel after 16.3 dpa neutron irradiation at 523, 623 and 723 K *J. Nucl. Mater.* **442** S62–S66
[84] Tavassoli A A F *et al* 2004 Materials design data for reduced activation martensitic steel type EUROFER *J. Nucl. Mater.* **329–333** 257–62
[85] Dai Y, Odette G R and Yamamoto T 2012 The effects of helium in irradiated structural alloys *Comprehensive Nuclear Materials* vol 1, ed R J M Konings (Oxford: Elsevier) pp 141–93
[86] Henry J, Averty X, Dai Y and Pizzanelli J P 2008 Tensile behaviour of 9Cr–1Mo tempered martensitic steels irradiated up to 20 dpa in a spallation environment *J. Nucl. Mater.* **377** 80–93
[87] Wakai E, Hashimoto N, Miwa Y, Robertson J P, Klueh R L, Shiba K and Jistukawa S 2000 Effect of helium production on swelling of F82H irradiated in HFIR *J. Nucl. Mater.* **283–287** 799–805
[88] Lin Y R, Bhattacharya A, Chen D, Kai J J, Henry J and Zinkle S J 2021 Temperature-dependent cavity swelling in dual-ion irradiated Fe and Fe–Cr ferritic alloys *Acta Mater.* **207** 116660

[89] Ando M, Nozawa T, Hirose T, Tanigawa H, Wakai E, Stoller R E and Myers J 2015 Effect of helium on irradiation creep behavior of B-doped F82H irradiated in HFIR *Fusion Sci. Technol.* **68** 648–51
[90] Gaganidze E, Gillemot F, Szenthe I, Gorley M, Rieth M and Diegele E 2018 Development of EUROFER97 database and material property handbook *Fusion Eng. Des.* **135** 9–14
[91] Rensman J, Van Osch E V, Horsten M G and D'Hulst D S 2000 Post-irradiation mechanical tests on F82H EB and TIG welds *J. Nucl. Mater.* **283–287** 1201–5
[92] Manugula V L, Rajulapati K V, Reddy G M and Rao K B S 2017 Role of evolving microstructure on the mechanical properties of electron beam welded ferritic-martensitic steel in the as-welded and post weld heat-treated states *Mater. Sci. Eng.* A **698** 36–45
[93] Li X, Chen J, Hua P, Chen K, Kong W, Chu H, Wu Y and Zhou W 2018 Effect of post weld heat treatment on the microstructure and properties of Laser-TIG hybrid welded joints for CLAM steel *Fusion Eng. Des.* **128** 175–81
[94] Gaganidze E, Dafferner B, Ries H, Rolli R, Schneider H-C and Aktaa J 2008 Irradiation programme HFR phase IIb—SPICE impact testing on up to 16.3 dpa irradiated RAFM steels *Final Report for Task* TW2-TTMS 001b-D05 (Euratom, Forschungszentrum Karlsruhe FZKA 7371)
[95] Gaganidze E, Schneider H C, Dafferner B and Aktaa J 2007 Embrittlement behavior of neutron irradiated RAFM steels *J. Nucl. Mater.* **367–370** 81–85
[96] Gaganidze E, Schneider H-C-C, Dafferner B and Aktaa J 2006 High-dose neutron irradiation embrittlement of RAFM steels *J. Nucl. Mater.* **355** 83–88
[97] Hirose T, Sokolov M A, Ando M, Tanigawa H, Shiba K, Stoller R E and Odette G R 2013 Irradiation response in weldment and HIP joint of reduced activation ferritic/martensitic steel, F82H *J. Nucl. Mater.* **442** S557–61
[98] Sokolov M A, Tanigawa H, Odette G R, Shiba K and Klueh R L 2007 Fracture toughness and Charpy impact properties of several RAFMS before and after irradiation in HFIR *J. Nucl. Mater.* **367–370** 68–73
[99] Kim B K, Tan L, Sakasegawa H, Parish C M, Zhong W, Tanigawa H and Katoh Y 2020 Effects of helium on irradiation response of reduced-activation ferritic-martensitic steels: using nickel isotopes to simulate fusion neutron response *J. Nucl. Mater.* **545** 152634
[100] Chen Frank X, Sokolov M A, Robertson J, Ando M, Geringer J W, Tanigawa H and Katoh Y 2020 Effects of HFIR neutron irradiation on fracture toughness properties of standard and Ni-doped F82H *J. Nucl. Mater.* **542** 152501
[101] Tong Z and Dai Y 2009 Tensile properties of the ferritic martensitic steel F82H after irradiation in a spallation target *J. Nucl. Mater.* **385** 258–61
[102] Wakai E, Ando M, Matsukawa S, Taguchi T, Yamamoto T, Tomita H and Takada F 2005 Effect of initial heat treatment on DBTT of F82H steel irradiated by neutrons *Fusion Sci. Technol.* 47 856–60
[103] Wakai E, Ando M, Sawai T, Tanigawa H, Taguchi T, Stoller R E, Yamamoto T, Kato Y and Takada F 2007 Effect of heat treatments on tensile properties of F82H steel irradiated by neutrons *J. Nucl. Mater.* **367–370** 74–80
[104] Ando M, Tanigawa H, Wakai E and Stoller R E 2009 Effect of two-steps heat treatments on irradiation hardening in F82H irradiated at 573 K *J. Nucl. Mater.* **386–388** 315–8
[105] Tanigawa H, Ando M, Katoh Y, Hirose T, Sakasegawa H, Jitsukawa S, Kohyama A and Iwai T 2001 Response of reduced activation ferritic steels to high fluence ion-irradiation *J. Nucl. Mater.* **297** 279–84
[106] Hirose T, Okubo N, Tanigawa H, Ando M, Sokolov M A, Stoller R E and Odette G R 2011 Irradiation hardening in F82H irradiated at 573 K in the HFIR *J. Nucl. Mater.* **417** 108–11
[107] Lucon E, Chaouadi R and Decréton M 2004 Mechanical properties of the European reference RAFM steel (EUROFER97) before and after irradiation at 300 °C *J. Nucl. Mater.* **329–333** 1078–82
[108] Lucon E 2003 Mechanical properties of the European reference RAFM steel (EUROFER97) before and after irradiation at 300 °C *EFDA Technology Workprogramme 2002 Tritium Breeding and Materials Materials Development—TTMS-001 Deliverable, SCK.CEN-BLG-962*
[109] Materna-Morris E, Möslang A, Rolli R and Schneider H C 2009 Effect of helium on tensile properties and microstructure in 9%Cr-WVTa-steel after neutron irradiation up to 15 dpa between 250 and 450 °C *J. Nucl. Mater.* **386–388** 422–5
[110] Alamo A, Horsten M, Averty X, Materna-Morris E I, Rieth M and Brachet J C 2000 Mechanical behavior of reduced-activation and conventional martensitic steels after neutron irradiation in the range 250–450 °C *J. Nucl. Mater.* **283–287** 353–7
[111] Klueh R L, Gelles D S, Jitsukawa S, Kimura A, Odette G R, Van der Schaaf B and Victoria M 2002 Ferritic/martensitic steels—overview of recent results *J. Nucl. Mater.* **307–311** 455–65
[112] Lucon E, Decréton M and Van Walle E 2003 Mechanical characterization of EUROFER97 irradiated (0.32 dpa, 300 °C) *Fusion Eng. Des.* **69** 373–7
[113] Bhattacharya A, Chen X, Linton K, Yamamoto Y, Sokolov M, Clowers L and Katoh Y 2018 Mechanical properties and microstructure characterization of unirradiated Eurofer-97 steel variants for the EURO fusion project *ORNL Technical Report* ORNL/SPR-2018/882 (Oak Ridge, TN)
[114] Shiba K, Klueh R L, Miwa Y, Robertson J P and Hishinuma A 2000 Tensile behavior of F82H with and without spectral tailoring *J. Nucl. Mater.* **283–287** 358–61
[115] Gelles D S, Hamilton M L, Oliver B M, Greenwood L R, Ohnuki S, Shiba K, Kohno Y, Kohyama A and Robertson J P 2002 Recent results for the ferritics isotopic tailoring (FIST) experiment *J. Nucl. Mater.* **307–311** 212–6
[116] Shiba K, Suzuki M and Hishinuma A 1996 Irradiation response on mechanical properties of neutron irradiated F82H *J. Nucl. Mater.* **233–237** 309–12
[117] Chaouadi R 2008 *Neutron-Irradiation + Helium Hardening & Embrittlement Modeling of 9%Cr-Steels in an Engineering Perspective (HELENA)* vol 2 (Julich: Forschungszentrum Juelich GmbH)
[118] Kimura A, Morimura T, Narui M and Matsui H 1996 Irradiation hardening of reduced activation martensitic steels *J. Nucl. Mater.* **233–237** 319–25
[119] Klueh R L 1996 *Proc. IEA Working Group Meeting on Ferritic/Martensitic Steels IEA WORKING GROUP—TASK ANNEX II Implementing Agreement for a Program of Research and Development on Fusion Materials, ORNL/M-5674* (*Oak Ridge, TN*)
[120] Klueh R L, Sokolov M A, Shiba K, Miwa Y and Robertson J P 2000 Embrittlement of reduced-activation ferritic/martensitic steels irradiated in HFIR at 300°C and 400°C *J. Nucl. Mater.* **283–287** 478–82
[121] Klueh R L 1991 Irradiation hardening of ferritic steels: effect of composition *J. Nucl. Mater.* **179–181** 728–32
[122] Klueh R L and Vitek J M 1985 Elevated-temperature tensile properties of irradiated 9Cr–1MoVNb steel *J. Nucl. Mater.* **132** 27–31
[123] Klueh R L and Vitek J M 1987 Postirradiation tensile behavior of nickel-doped ferritic steels *J. Nucl. Mater.* **150** 272–80
[124] Klueh R L and Vitek J M 1989 Fluence and helium effects on the tensile properties of ferritic steels at low temperatures *J. Nucl. Mater.* **161** 13–23

[125] Klueh R L, Maziasz P J and Vitek J M 1986 Postirradiation tensile behavior of nickel-doped ferritic steels *J. Nucl. Mater.* **141–143** 960–5
[126] Klueh R L and Maziasz P J 1992 Effect of irradiation in HFIR on tensile properties of Cr–Mo steels *J. Nucl. Mater.* **187** 43–54
[127] Séran J L, Alamo A, Maillard A, Touron H, Brachet J C, Dubuisson P and Rabouille O 1994 Pre- and post-irradiation mechanical properties of ferritic-martensitic steels for fusion applications: EM10 base metal and EM10/EM10 welds *J. Nucl. Mater.* **212–215** 588–93
[128] Alamo A, Séran J, Rabouille O, Brachet J, Maillard A, Touron H and Royer J 1996 Irradiation effects on base metal and welds of 9Cr–1Mo (EM10) martensitic steel *ASTM Special Technical Publication* vol 1270 (West Conshohocken, PA: ASTM International) pp 761–74
[129] Séran J, Lévy V, Gilbon D, Maillard A, Fissolo A, Touron H, Cauvin R, Chalony A and Le Boulbin E 1992 Behavior under neutron irradiation of the 15–15Ti and EM10 steels used as standard materials of the Phénix fuel subassembly *ASTM Special Technical Publication* pp 1209–33
[130] Zinkle S J, Robertson J P and Klueh R 1998 Thermophysical and mechanical properties of Fe-(8-9%)Cr reduced activation steels *Fusion Materials Semiannual Progress Report for Period Ending June 30 1998, DOE/ER-0313/24* (*Oak Ridge, TN*)
[131] Rieth M, Schirra M, Falkenstein A, Graf P, Heger S, Kempe H, Lindau R and Zimmermann H 2003 EUROFER 97 tensile, charpy, creep and structural tests *FZKA 6911 Report* (Karlsruhe: Karlsruhe Institute of Technology)
[132] Shiba K, Hishinuma A, Kohyama A and Masamura K 1997 Properties of low activation ferritic steel F82H IEA heat *Interim Report of IEA Round-Robin Tests* Report JAERI-Tech 97-038 (Japan)
[133] Yamanouchi N, Tamura M, Hayakawa H, Hishinuma A and Kondo T 1992 Accumulation of engineering data for practical use of reduced activation ferritic steel: 8%Cr2%W0.2%V0.04%TaFe *J. Nucl. Mater.* **191–194** 822–6
[134] Shashank Dutt B, Nani Babu M, Shanthi G, Moitra A and Sasikala G 2018 Investigation on fracture behavior of grade 91 steel at 300–550 °C *J. Mater. Eng. Perform.* **27** 6577–84
[135] Henry J, Averty X and Alamo A 2011 Tensile and impact properties of 9Cr tempered martensitic steels and ODS-FeCr alloys irradiated in a fast reactor at 325 °C up to 78 dpa *J. Nucl. Mater.* **417** 99–103
[136] Alamo A, Bertin J L, Shamardin V K and Wident P 2007 Mechanical properties of 9Cr martensitic steels and ODS-FeCr alloys after neutron irradiation at 325 °C up to 42 dpa *J. Nucl. Mater.* **367–370** 54–59
[137] Alamo A, Lambard V, Averty X and Mathon M H 2004 Assessment of ODS-14%Cr ferritic alloy for high temperature applications *J. Nucl. Mater.* **329–333** 333–7
[138] Kohno Y, Kohyama A, Hirose T, Hamilton M L and Narui M 1999 Mechanical property changes of low activation ferritic/martensitic steels after neutron irradiation *J. Nucl. Mater.* **271–272** 145–50
[139] Henry J, Mathon M H and Jung P 2003 Microstructural analysis of 9% Cr martensitic steels containing 0.5 at.% helium *J. Nucl. Mater.* **318** 249–59
[140] van der Schaaf B, Petersen C, De Carlan Y, Rensman J W, Gaganidze E and Averty X 2009 High dose, up to 80 dpa, mechanical properties of Eurofer 97 *J. Nucl. Mater.* **386–388** 236–40
[141] Materna-Morris E, Lindau R, Schneider H C and Möslang A 2015 Tensile behavior of EUROFER ODS steel after neutron irradiation up to 16.3 dpa between 250 and 450 °C *Fusion Eng. Des.* **98–99** 2038–41
[142] Luzginova N V, Nolles H S, Ten Pierick P, Bakker T, Mutnuru R K, Jong M and Blagoeva D T 2012 Irradiation response of ODS Eurofer97 steel *J. Nucl. Mater.* **428** 192–6
[143] McClintock D A, Sokolov M A, Hoelzer D T and Nanstad R K 2009 Mechanical properties of irradiated ODS-EUROFER and nanocluster strengthened 14YWT *J. Nucl. Mater.* **392** 353–9
[144] Henry J, Doriot S, Vincent S, Caes C, Toffolon C, Wident P, Piozin E and Brachet J-C 2015 Improvement of Eurofer 97 high-temperature mechanical properties using non-standard heat treatments *17th Int. Conf. Fusion Reactor Materials, Oral Presentation* (*Aachen*)
[145] Bhattacharya A, Meslin E, Henry J, Leprêtre F, Décamps B and Barbu A 2019 Combined effect of injected interstitials and He implantation, and cavities inside dislocation loops in high purity Fe–Cr alloys *J. Nucl. Mater.* **519** 30–44
[146] Chen X, Bhattacharya A, Sokolov M A, Clowers L N, Yamamoto Y, Graening T, Linton K D, Katoh Y and Rieth M 2019 Mechanical properties and microstructure characterization of Eurofer97 steel variants in EUROfusion program *Fusion Eng. Des.* **146** 2227–32
[147] Kocks U F, Argon A S and Ashby M F 1975 Thermodynamics and kinetics of slip *Prog. Mater. Sci.* **19** 1–291
[148] Diehl J, Seidel G P and Weller M 1968 Neutron irradiation hardening of iron single crystals containing small amounts of carbon *Trans. Japan. Inst. Met.* **9** 219–25
[149] Suganuma K and Kayano H 1983 Irradiation hardening of Fe–Cr alloys *J. Nucl. Mater.* **118** 234–41
[150] ACFEN 2018 *RCC-MRx, Edition 2018, Design and Construction Rules for Mechanical Components of Nuclear Installations: High-temperature, Research and Fusion, Reactors* (France: Association Francaise pour les regles de Conception et de Construction des Materiels des Chaudieres Electro-nucleares)
[151] Farrell K and Byun T S 2003 Tensile properties of ferritic/martensitic steels irradiated in HFIR, and comparison with spallation irradiation data *J. Nucl. Mater.* **318** 274–82
[152] Byun T S, Farrell K and Li M 2008 Deformation in metals after low-temperature irradiation: part I—mapping macroscopic deformation modes on true stress-dose plane *Acta Mater.* **56** 1044–55
[153] Byun T S and Farrell K 2004 Plastic instability in polycrystalline metals after low temperature irradiation *Acta Mater.* **52** 1597–608
[154] Vanaja J, Laha K, Sam S, Nandagopal M, Panneer Selvi S, Mathew M D, Jayakumar T and Rajendra Kumar E 2012 Influence of strain rate and temperature on tensile properties and flow behaviour of a reduced activation ferritic-martensitic steel *J. Nucl. Mater.* **424** 116–22
[155] Sannazzaro G, Barabash V, Kang S C, Fernandez E, Kalinin G, Obushev A, Martínez V J, Vázquez I, Fernández F and Guirao J 2013 Development of design criteria for ITER in-vessel components *Fusion Eng. Des.* **88** 2138–41
[156] Arsenlis A, Wirth B D and Rhee M 2004 Dislocation density-based constitutive model for the mechanical behaviour of irradiated Cu *Phil. Mag.* **84** 3617–35
[157] Chaouadi R 2008 Effect of irradiation-induced plastic flow localization on ductile crack resistance behavior of a 9%Cr tempered martensitic steel *J. Nucl. Mater.* **372** 379–90
[158] Brachet J-C, Averty X, Lamagnère P, Alamo A, Rozenblum F, Raquet O and Bertin J-L 2002 Behavior of different austenitic stainless steels, conventional, reduced activation (RA) and ODS chromium-rich ferritic-martensitic steels under neutron irradiation at 325°C in PWR environment *Effects of Radiation on Materials: 20th Int. Symp., ASTM STP 1405* ed S T Rosinski, M L Grossbeck, T R Allen and A S Kumar (West Conshohocken, PA: American Society for Testing and Materials) pp 500–20

[159] Jitsukawa S, Suzuki K, Okubo N, Ando M and Shiba K 2009 Irradiation effects on reduced activation ferritic/martensitic steels—tensile, impact, fatigue properties and modelling *Nucl. Fusion* **49** 115006
[160] Rensman J 2005 NRG irradiation testing: report on 300 °C and 60 °C irradiated RAFM steels
[161] Cho H S, Kasada R and Kimura A 2007 Effects of neutron irradiation on the tensile properties of high-Cr oxide dispersion strengthened ferritic steels *J. Nucl. Mater.* **367–370** 239–43
[162] Yamashita S, Yoshitake T, Akasaka N, Ukai S and Kimura A 2007 Mechanical behavior of oxide dispersion strengthened steels irradiated in JOYO *J. Nucl. Mater.* **376–370** 202–7
[163] Bhattacharya A, Reed J, Chen X, Geringer J W, Katoh Y, Nozawa T and Tanigawa H 2020 Neutron irradiation induced hardening in RAFM and ODS steels *Fusion Reactor Materials Program Semi-Annual Report* DOE/ER-0313/69 (Oak Ridge National Lab)
[164] Kim J H, Byun T S, Hoelzer D T, Park C H, Yeom J T and Hong J K 2013 Temperature dependence of strengthening mechanisms in the nanostructured ferritic alloy 14YWT: part II—mechanistic models and predictions *Mater. Sci. Eng.* A **559** 111–8
[165] Sacksteder I, Schneider H C and Materna-Morris E 2011 Determining irradiation damage and recovery by instrumented indentation in RAFM steel *J. Nucl. Mater.* **417** 127–30
[166] Kolluri M, Edmondson P D, Luzginova N V and Berg F A V D 2014 Influence of irradiation temperature on microstructure of EU batch of ODS Eurofer97 steel irradiated with neutrons *Energy Mater.: Mater. Sci. Eng. Energy Syst.* **9** 1697–703
[167] Alam M E, Pal S, Fields K, Maloy S A, Hoelzer D T and Odette G R 2016 Tensile deformation and fracture properties of a 14YWT nanostructured ferritic alloy *Mater. Sci. Eng.* A **675** 437–48
[168] Das A, Chekhonin P, Altstadt E, McClintock D, Bergner F, Heintze C and Lindau R 2020 Microstructure and fracture toughness characterization of three 9Cr ODS EUROFER steels with different thermo-mechanical treatments *J. Nucl. Mater.* **542** 152464
[169] Hoelzer D T, Unocic K A, Sokolov M A and Byun T S 2016 Influence of processing on the microstructure and mechanical properties of 14YWT *J. Nucl. Mater.* **471** 251–65
[170] Byun T S, Farrell K and Hashimoto N 2004 Plastic instability behavior of bcc and hcp metals after low temperature neutron irradiation *J. Nucl. Mater.* **329–333** 998–1002
[171] Farrell K, Byun T S and Hashimoto N 2004 Deformation mode maps for tensile deformation of neutron-irradiated structural alloys *J. Nucl. Mater.* **335** 471–86
[172] Odette G R, He M Y, Donahue E G, Spatig P and Yamamoto T 2002 Modeling the multiscale mechanics of flow localization-ductility loss in irradiation damaged bcc alloys *J. Nucl. Mater.* **307–311** 171–8
[173] Weiss O J, Gaganidze E and Aktaa J 2012 Quantitative characterization of microstructural defects in up to 32 dpa neutron irradiated EUROFER97 *J. Nucl. Mater.* **426** 52–58
[174] Pareige C, Kuksenko V and Pareige P 2015 Behaviour of P, Si, Ni impurities and Cr in self ion irradiated Fe–Cr alloys—comparison to neutron irradiation *J. Nucl. Mater.* **456** 471–6
[175] Bergner F, Pareige C, Hernández-Mayoral M, Malerba L and Heintze C 2014 Application of a three-feature dispersed-barrier hardening model to neutron-irradiated Fe–Cr model alloys *J. Nucl. Mater.* **448** 96–102
[176] Kuksenko V, Pareige C, Genevois C and Pareige P 2013 Characterisation of Cr, Si and P distribution at dislocations and grain-boundaries in neutron irradiated Fe–Cr model alloys of low purity *J. Nucl. Mater.* **434** 49–55
[177] Gómez-Ferrer B, Dethloff C, Gaganidze E, Malerba L, Hatzoglou C and Pareige C 2020 Nano-hardening features in high-dose neutron irradiated Eurofer97 revealed by atom-probe tomography *J. Nucl. Mater.* **537** 152228
[178] Bhattacharya A, Levine S M, Poplawsky J, Edmondson P D, Geringer J W, Katoh Y, Nozawa T and Tanigawa H 2021 Microstructure Characterization of F82H-IEA after low dose HFIR neutron irradiations at 300 °C *Fusion Reactor Materials Program Semi-Annual Report* DOE/ER-0313/70 (Oak Ridge National Lab)
[179] Davis T P, Auger M A, Almirall N, Hosemann P, Odette G R, Bagot P A J, Moody M P and Armstrong D E J 2020 Atom probe characterisation of segregation driven Cu and Mn–Ni–Si co-precipitation in neutron irradiated T91 tempered-martensitic steel *Materialia* **14** 110946
[180] Lambrecht M, Meslin E, Malerba L, Hernández-Mayoral M, Bergner F, Pareige P, Radiguet B and Almazouzi A 2010 On the correlation between irradiation-induced microstructural features and the hardening of reactor pressure vessel steels *J. Nucl. Mater.* **406** 84–89
[181] Meslin E, Radiguet B, Pareige P, Toffolon C and Barbu A 2011 Irradiation-induced solute clustering in a low nickel FeMnNi ferritic alloy *Exp. Mech.* **51** 1453–8
[182] Odette G R, Almirall N, Wells P B and Yamamoto T 2021 Precipitation in reactor pressure vessel steels under ion and neutron irradiation: on the role of segregated network dislocations *Acta Mater.* **212** 116922
[183] Meslin E *et al* 2010 Characterization of neutron-irradiated ferritic model alloys and a RPV steel from combined APT, SANS, TEM and PAS analyses *J. Nucl. Mater.* **406** 73–83
[184] Terentyev D, Bergner F and Osetsky Y 2013 Cr segregation on dislocation loops enhances hardening in ferritic Fe–Cr alloys *Acta Mater.* **61** 1444–53
[185] Bhattacharya A, Meslin E, Henry J, Pareige C, Décamps B, Genevois C, Brimbal D and Barbu A 2014 Chromium enrichment on the habit plane of dislocation loops in ion-irradiated high-purity Fe–Cr alloys *Acta Mater.* **78** 394–403
[186] Boutard J-L *et al* 2014 Oxide dispersion strengthened ferritic steels: a basic research joint program in France *J. Nucl. Mater.* **455** 605–11
[187] Klimiankou M, Lindau R, Möslang A and Schröder J 2005 TEM study of PM 2000 steel *Powder Metall.* **48** 277–87
[188] Massey C P, Dryepondt S N, Edmondson P D, Frith M G, Littrell K C, Kini A, Gault B, Terrani K A and Zinkle S J 2019 Multiscale investigations of nanoprecipitate nucleation, growth, and coarsening in annealed low-Cr oxide dispersion strengthened FeCrAl powder *Acta Mater.* **166** 1–17
[189] Hoelzer D T, Massey C P, Zinkle S J, Crawford D C and Terrani K A 2020 Modern nanostructured ferritic alloys: a compelling and viable choice for sodium fast reactor fuel cladding applications *J. Nucl. Mater.* **529** 151928
[190] Odette G R and Hoelzer D T 2010 Irradiation-tolerant nanostructured ferritic alloys: transforming helium from a liability to an asset *JOM* **62** 84–92
[191] Massey C P, Edmondson P D, Field K G, Hoelzer D T, Dryepondt S N, Terrani K A and Zinkle S J 2019 Post irradiation examination of nanoprecipitate stability and α' precipitation in an oxide dispersion strengthened Fe–12Cr–5Al alloy *Scr. Mater.* **162** 94–8
[192] Aydogan E *et al* 2019 Response of 14YWT alloys under neutron irradiation: a complementary study on microstructure and mechanical properties *Acta Mater.* **167** 181–96
[193] Wang J, Toloczko M B, Voyevodin V N, Bryk V V, Borodin O V, Mel'nychenko V V, Kalchenko A S, Garner F A and Shao L 2021 Atom probe tomography characterization of high-dose ion irradiated MA957 *J. Nucl. Mater.* **545** 152528

[194] Ribis J 2013 Structural and chemical matrix evolution following neutron irradiation in a MA957 oxide dispersion strengthened material *J. Nucl. Mater.* **434** 178–88
[195] Ribis J 2020 Phase stability in irradiated alloys *Comprehensive Nuclear Materials* vol 1 (Amsterdam: Elsevier) pp 265–309
[196] Monnet I 1999 Stabilité sous irradiation de particules d'oxydes finement disperses dans les alliages ferritiques *PhD Thesis* Ecole Centrale de Paris, France Report CEA-R-5868
[197] Levine S M, Bhattacharya A, Hoelzer D T, Katoh Y and Zinkle S J 2020 Irradiation induced phase separation in oxide dispersion strengthened alloys *Fusion Materials Research at Oak Ridge National Laboratory in Fiscal Year 2020, ORNL/TM-2020/1837* ed F W Wiffen, Y Katoh and S Melton (Oak Ridge, TN: Oak Ridge National Lab) p 21
[198] Lee J S, Jang C H, Kim I S and Kimura A 2007 Embrittlement and hardening during thermal aging of high Cr oxide dispersion strengthened alloys *J. Nucl. Mater.* **367–370** 229–33
[199] Zhang Z, Saleh T A, Maloy S A and Anderoglu O 2020 Microstructure evolution in MA956 neutron irradiated in ATR at 328 °C to 4.36 dpa *J. Nucl. Mater.* **533** 152094
[200] Bhattacharya A, Levine S, Reed J, Geringer J, Hoelzer D, Chen X, Katoh Y, Edmondson P and Katoh Y 2022 Tensile testing and microstructure characterization of HFIR irradiated F82H and ODS steels *2022 Annual DOE-QST Steering Committee Meeting Presentation and Report* (Oak Ridge National Lab)
[201] Oh S, Lee J S, Jang C and Kimura A 2009 Irradiation hardening and embrittlement in high-Cr oxide dispersion strengthened steels *J. Nucl. Mater.* **386–388** 503–6
[202] Senninger O, Soisson F, Martínez E, Nastar M, Fu C-C and Bréchet Y 2016 Modeling radiation induced segregation in iron–chromium alloys *Acta Mater.* **103** 1–11
[203] Bonny G, Terentyev D and Malerba L 2008 On the α–α′ miscibility gap of Fe–Cr alloys *Scr. Mater.* **59** 1193–6
[204] Bailey N A, Stergar E, Toloczko M and Hosemann P 2015 Atom probe tomography analysis of high dose MA957 at selected irradiation temperatures *J. Nucl. Mater.* **459** 225–34
[205] Monnet I, Dubuisson P, Serruys Y, Ruault M O, Kaïtasov O and Jouffrey B 2004 Microstructural investigation of the stability under irradiation of oxide dispersion strengthened ferritic steels *J. Nucl. Mater.* **335** 311–21
[206] Dubuisson P, Maillard A, Delalande C, Gilbon D and Seran J L 1990 The effect of phosphorus on the radiation induced microstructure of stabilized austenitic stainless steels *15th Int. Symp. on the Effects of Radiation on Materials* (*Nashville, TN*) pp 1–23
[207] Senninger O, Martínez E, Soisson F, Nastar M and Bréchet Y 2014 Atomistic simulations of the decomposition kinetics in Fe–Cr alloys: influence of magnetism *Acta Mater.* **73** 97–106
[208] Dubuisson P, Gilbon D and Séran J L 1993 Microstructural evolution of ferritic-martensitic steels irradiated in the fast breeder reactor Phénix *J. Nucl. Mater.* **205** 178–89
[209] Levine S, Zinkle S, Bhattacharya A, Poplawsky J, Hoelzer D and Katoh Y 2021 Temperature and dose effects on phase separation in neutron irradiated PM2000 and MA957 *Fusion Reactor Materials Program, Semi-annual Report, DOE/ER-0313/70* vol 70 (Oak Ridge, TN: Oak Ridge National Lab) pp 31–35
[210] Sang W, Dou P and Kimura A 2020 Early-stage thermal ageing behavior of 12Cr, 12Cr–7Al and 18Cr–9Al ODS steels *J. Nucl. Mater.* **535** 152164
[211] Capdevila C, Aranda M M, Rementeria R, Chao J, Urones-Garrote E, Aldazabal J and Miller M K 2016 Strengthening by intermetallic nanoprecipitation in Fe–Cr–Al–Ti alloy *Acta Mater.* **107** 27–37
[212] Levine S M, Zinkle S J, Bhattacharya A, Poplawsky J, Hoelzer D and Katoh Y 2021 Temperature and dose effects on phase separation in neutron irradiated PM2000 and MA957 *DOE-FES Fusion Materials Semi-Annual Report* DOE-ER-0313/70 vol 70 (Oak Ridge, TN) p 31
[213] Hoelzer D and Massey C P 2021 Development of ODS Fe–10Cr alloys *DOE-FES Fusion Reactor Materials Program Semi-Annual Report* DOE/ER-0313/69 vol 69 (Oak Ridge, TN) p 67
[214] Bhattacharya A, Meslin E, Henry J, Decamps B and Barbu A 2013 Ion irradiation damage in FeCr and ODS alloys *Report to CPR-ODISSEE* DEN/DMN/SRMP (Gif-sur-Yvette: CEA-Saclay)
[215] Bhattacharya A 2014 Ion irradiation effects on high purity bcc Fe and model FeCr alloys *PhD Thesis* University of Paris SUD, France
[216] Wharry J P, Swenson M J and Yano K H 2017 A review of the irradiation evolution of dispersed oxide nanoparticles in the b.c.c. Fe–Cr system: current understanding and future directions *J. Nucl. Mater.* **486** 11–20
[217] Dubuisson P, de Carlan Y, Garat V and Blat M 2012 ODS ferritic/martensitic alloys for sodium fast reactor fuel pin cladding *J. Nucl. Mater.* **428** 6–12
[218] Ribis J and Lozano-Perez S 2014 Nano-cluster stability following neutron irradiation in MA957 oxide dispersion strengthened material *J. Nucl. Mater.* **444** 314–22
[219] Ribis J, Bordas E, Trocellier P, Serruys Y, de Carlan Y and Legris A 2015 Comparison of the neutron and ion irradiation response of nano-oxides in oxide dispersion strengthened materials *J. Mater. Res.* **30** 2210–21
[220] Yamashita S, Akasaka N, Ukai S and Ohnuki S 2007 Microstructural development of a heavily neutron-irradiated ODS ferritic steel (MA957) at elevated temperature *J. Nucl. Mater.* **367–370** 202–7
[221] Klimenkov M, Lindau R, Jäntsch U and Möslang A 2017 Effect of irradiation temperature on microstructure of ferritic-martensitic ODS steel *J. Nucl. Mater.* **493** 426–35
[222] Rogozhkin S V, Aleev A A, Zaluzhnyi A G, Nikitin A A, Iskandarov N A, Vladimirov P, Lindau R and Möslang A 2011 Atom probe characterization of nano-scaled features in irradiated ODS Eurofer steel *J. Nucl. Mater.* **409** 94–99
[223] Levine S M, Bhattacharya A, Lupini A R, Uberuaga B P, Hoelzer D T, Katoh Y and Zinkle S J 2022 Irradiation-induced transformation of embedded crystalline nano-oxides into nanoporous sponge-like structures under neutron irradiation (in preparation)
[224] Levine S M, Bhattacharya A, Lupini A R, Hoelzer D T, Geringer J W, Katoh Y and Zinkle S J 2019 Dispersoid nanostructure of PM2000 ODS steel after >80 dpa neutron irradiation *19th Int. Conf. on Fusion Reactor Materials, Poster* (La Jolla, CA) (https://doi.org/10.1089/hum.2019.008)
[225] Akasaka N, Yamashita S, Yoshitake T, Ukai S and Kimura A 2004 Microstructural changes of neutron irradiated ODS ferritic and martensitic steels *J. Nucl. Mater.* **329–333** 1053–6
[226] Certain A, Kuchibhatla S, Shutthanandan V, Hoelzer D T and Allen T R 2013 Radiation stability of nanoclusters in nano-structured oxide dispersion strengthened (ODS) steels *J. Nucl. Mater.* **434** 311–21
[227] Ohtsuka S, Kaito T, Yano Y, Yamashita S, Ogawa R, Uwaba T, Koyama S and Tanaka K 2013 Investigation of the cause of peculiar irradiation behavior of 9Cr-ODS steel in BOR-60 irradiation tests *J. Nucl. Sci. Technol.* **50** 470–80

[228] Rogozhkin S V *et al* 2015 Nanostructure evolution in ODS Eurofer steel under irradiation up to 32 dpa *Phys. Met. Metallogr.* **116** 72–78
[229] Jung H J, Edwards D J, Kurtz R J, Yamamoto T, Wu Y and Odette G R 2017 Structural and chemical evolution in neutron irradiated and helium-injected ferritic ODS PM2000 alloy *J. Nucl. Mater.* **484** 68–80
[230] Miller M K and Hoelzer D T 2011 Effect of neutron irradiation on nanoclusters in MA957 ferritic alloys *J. Nucl. Mater.* **418** 307–10
[231] Allen T R, Gan J, Cole J I, Ukai S, Shutthanandan S and Thevuthasan S 2005 The stability of 9Cr-ODS oxide particles under heavy-ion irradiation *Nucl. Sci. Eng.* **151** 305–12
[232] Allen T R, Gan J, Cole J I, Miller M K, Busby J T, Shutthanandan S and Thevuthasan S 2008 Radiation response of a 9 chromium oxide dispersion strengthened steel to heavy ion irradiation *J. Nucl. Mater.* **375** 26–37
[233] Kishimoto H, Yutani K, Kasada R, Hashitomi O and Kimura A 2007 Heavy-ion irradiation effects on the morphology of complex oxide particles in oxide dispersion strengthened ferritic steels *J. Nucl. Mater.* **367–370** 179–84
[234] Song P, Kimura A, Yabuuchi K, Dou P, Watanabe H, Gao J and Huang Y-J 2020 Assessment of phase stability of oxide particles in different types of 15Cr-ODS ferritic steels under 6.4 MeV Fe ion irradiation at 200 °C *J. Nucl. Mater.* **529** 151953
[235] Monnet I, Grygiel C, Lescoat M L and Ribis J 2012 Amorphization of oxides in ODS steels/materials by electronic stopping power *J. Nucl. Mater.* **424** 12–16
[236] Ribis J, Lescoat M L, Zhong S Y, Mathon M H and de Carlan Y 2013 Influence of the low interfacial density energy on the coarsening resistivity of the nano-oxide particles in Ti-added ODS material *J. Nucl. Mater.* **442** 101–5
[237] Asano K, Kohno Y, Kohyama A, Suzuki T and Kusanagi H 1988 Microstructural evolution of an oxide dispersion strengthened steel under charged particle irradiation *J. Nucl. Mater.* **155–157** 928–34
[238] Certain A G, Field K G, Allen T R, Miller M K, Bentley J and Busby J T 2010 Response of nanoclusters in a 9Cr ODS steel to 1 dpa, 525 °C proton irradiation *J. Nucl. Mater.* **407** 2–9
[239] Chen T, Gigax J G, Price L, Chen D, Ukai S, Aydogan E, Maloy S A, Garner F A and Shao L 2016 Temperature dependent dispersoid stability in ion-irradiated ferritic-martensitic dual-phase oxide-dispersion-strengthened alloy: coherent interfaces vs. incoherent interfaces *Acta Mater.* **116** 29–42
[240] de Castro V, Briceno M, Lozano-Perez S, Trocellier P, Roberts S G and Pareja R 2014 TEM characterization of simultaneous triple ion implanted ODS Fe12Cr *J. Nucl. Mater.* **455** 157–61
[241] He J, Wan F, Sridharan K, Allen T R, Certain A, Shutthanandan V and Wu Y Q 2014 Stability of nanoclusters in 14YWT oxide dispersion strengthened steel under heavy ion-irradiation by atom probe tomography *J. Nucl. Mater.* **455** 41–45
[242] Edmondson P D, London A, Xu A, Armstrong D E J and Roberts S G 2015 Small-scale characterisation of irradiated nuclear materials: part I—microstructure *J. Nucl. Mater.* **462** 369–73
[243] Kaoumi D, Motta A and Kirk M 2008 Characterization and *in-situ* ion-irradiation of MA957 ODS steel *Trans. Am. Nucl. Soc.* **98** 1113–4
[244] Little E A 1996 Influence of thermomechanical treatment on irradiation microstructures in an ODS ferritic steel *ASTM Special Technical Publication* vol 1270 pp 739–52
[245] Liu C, Yu C, Hashimoto N, Ohnuki S, Ando M, Shiba K and Jitsukawa S 2011 Micro-structure and micro-hardness of ODS steels after ion irradiation *J. Nucl. Mater.* **417** 270–3
[246] London A J, Panigrahi B K, Tang C C, Murray C and Grovenor C R M 2016 Glancing angle XRD analysis of particle stability under self-ion irradiation in oxide dispersion strengthened alloys *Scr. Mater.* **110** 24–27
[247] Yutani K, Kasada R, Kishimoto H, Kimura A, Lott R and Dean S W 2007 Irradiation hardening and microstructure evolution of ion-irradiated ODS ferritic steels *J. ASTM Int.* **4** 100701
[248] Pareige P, Miller M K, Stoller R E, Hoelzer D T, Cadel E and Radiguet B 2007 Stability of nanometer-sized oxide clusters in mechanically-alloyed steel under ion-induced displacement cascade damage conditions *J. Nucl. Mater.* **360** 136–42
[249] Pasebani S, Charit I, Burns J, Alsagabi S, Butt D P, Cole J I, Price L M and Shao L 2015 Microstructural stability of a self-ion irradiated lanthanum-bearing nanostructured ferritic steel *J. Nucl. Mater.* **462** 191–204
[250] Ribis J, Lescoat M L, de Carlan Y, Costantini J M, Monnet I, Cozzika T, Delabrouille F and Malaplate J 2011 Stability of nano-oxides upon heavy ion irradiation of an ODS material *J. Nucl. Mater.* **417** 262–5
[251] Ramar A, Baluc N and Schäublin R 2007 Effect of irradiation on the microstructure and the mechanical properties of oxide dispersion strengthened low activation ferritic/martensitic steel *J. Nucl. Mater.* **367–370** 217–21
[252] Robertson C, Panigrahi B K, Balaji S, Kataria S, Serruys Y, Mathon M H and Sundar C S 2012 Particle stability in model ODS steel irradiated up to 100 dpa at 600 °C: TEM and nano-indentation investigation *J. Nucl. Mater.* **426** 240–6
[253] Saito J, Suda T, Yamashita S, Ohnuki S, Takahashi H, Akasaka N, Nishida M and Ukai S 1998 Void formation and microstructural development in oxide dispersion strengthened ferritic steels during electron-irradiation *J. Nucl. Mater.* **258–263** 1264–8
[254] Šćepanović M, de Castro V, Leguey T, Auger M A, Lozano-Perez S and Pareja R 2016 Microstructural stability of ODS Fe–14Cr (–2W–0.3Ti) steels after simultaneous triple irradiation *Nucl. Mater. Energy* **9** 490–5
[255] Schäublin R, Ramar A, Baluc N, de Castro V, Monge M A, Leguey T, Schmid N and Bonjour C 2006 Microstructural development under irradiation in European ODS ferritic/martensitic steels *J. Nucl. Mater.* **351** 247–60
[256] Swenson M J and Wharry J P 2015 The comparison of microstructure and nanocluster evolution in proton and neutron irradiated Fe–9%Cr ODS steel to 3 dpa at 500 °C *J. Nucl. Mater.* **467** 97–112
[257] Swenson M J and Wharry J P 2017 Nanocluster irradiation evolution in Fe–9%Cr ODS and ferritic-martensitic alloys *J. Nucl. Mater.* **496** 24–40
[258] Swenson M J, Dolph C K and Wharry J P 2016 The effects of oxide evolution on mechanical properties in proton- and neutron-irradiated Fe–9%Cr ODS steel *J. Nucl. Mater.* **479** 426–35
[259] Williams C A, Hyde J M, Smith G D W and Marquis E A 2011 Effects of heavy-ion irradiation on solute segregation to dislocations in oxide-dispersion-strengthened Eurofer 97 steel *J. Nucl. Mater.* **412** 100–5
[260] Yu C Z, Oka H, Hashimoto N and Ohnuki S 2011 Development of damage structure in 16Cr–4Al ODS steels during electron-irradiation *J. Nucl. Mater.* **417** 286–8
[261] Li F, Abe H, Ishizaki T, Li Y, Nagasaka T, Muroga T, Nagase T and Yasuda H 2014 Stability of oxide particles under electron irradiation in a 9Cr ODS steel at 400 °C *J. Nucl. Mater.* **455** 724–7
[262] Monnet I, van den Berghe T and Dubuisson P 2012 A comparison between different oxide dispersion strengthened ferritic steel ongoing in situ oxide dissolution in high voltage electron microscope *J. Nucl. Mater.* **424** 204–9
[263] Kimura A, Cho H-S, Toda N, Kasada R, Yutani K, Kishimoto H, Iwata N, Ukai S and Fujiwara M 2007 High burnup fuel cladding materials R and D for advanced nuclear systems *J. Nucl. Sci. Technol.* **44** 323–8

[264] Lescoat M L et al 2014 Radiation-induced Ostwald ripening in oxide dispersion strengthened ferritic steels irradiated at high ion dose *Acta Mater.* **78** 328–40
[265] Lescoat M L, Ribis J, Gentils A, Kaïtasov O, de Carlan Y and Legris A 2012 In situ TEM study of the stability of nano-oxides in ODS steels under ion-irradiation *J. Nucl. Mater.* **428** 176–82
[266] Bhattacharya A, Lupini A R, Hoelzer D T, Geringer J W, Katoh Y, Levine S M and Zinkle S J 2019 Novel insights into neutron irradiated ODS alloys by advanced characterization *Fusion Reactor Materials Program Semi-Annual Report* vol 67 DOE/ER-0313/67 (Oak Ridge, TN)
[267] Batygin Y K and Pitcher E J 2020 Advancement of LANSCE accelerator facility as a 1-MW fusion prototypic neutron source *Nucl. Instrum. Methods Phys. Res.* A **960** 163569
[268] Egle B, Ferguson P and White T 2019 U.S. fusion D-Li neutron irradiation facility: fusion prototypic neutron source (FPNS) technology study *Oak Ridge National Laboratory Technical Report* ORNL/TM-2019/1453 (Oak Ridge, TN)
[269] Parish C M, Unocic K A, Tan L, Zinkle S J, Kondo S, Snead L L, Hoelzer D T and Katoh Y 2017 Helium sequestration at nanoparticle-matrix interfaces in helium + heavy ion irradiated nanostructured ferritic alloys *J. Nucl. Mater.* **483** 21–34
[270] Odette G R, Alinger M J and Wirth B D 2008 Recent developments in irradiation-resistant steels *Annu. Rev. Mater. Res.* **38** 471–503
[271] Rieth M *et al* 2010 EUROFER-Fe54 specimen production and irradiation proposal *EFDA Fusion Report* No. 375 (Germany: Karlsruhe Institute of Technology)
[272] Hashimoto N, Klueh R L and Shiba K 2002 Pros and cons of nickel- and boron-doping to study helium effects in ferritic/martensitic steels *J. Nucl. Mater.* **307–311** 222–8
[273] Mansur L K, Rowcliffe A F, Grossbeck M L and Stoller R E 1986 Isotopic alloying to tailor helium production rates in mixed-spectrum reactors *J. Nucl. Mater.* **139** 228–36
[274] Odette G R, Miao P, Edwards D J, Yamamoto T, Kurtz R J and Tanigawa H 2011 Helium transport, fate and management in nanostructured ferritic alloys: in situ helium implanter studies *J. Nucl. Mater.* **417** 1001–4
[275] Kuksenko V, Pareige C, Pareige P and Dai Y 2014 Production and segregation of transmutation elements Ca, Ti, Sc in the F82H steel under mixed spectrum irradiation of high energy protons and spallation neutrons *J. Nucl. Mater.* **447** 189–96
[276] Bhattacharya A, Parish C M, Koyanagi T, Petrie C M, King D, Hilmas G, Fahrenholtz W G, Zinkle S J and Katoh Y 2019 Nano-scale microstructure damage by neutron irradiations in a novel Boron-11 enriched TiB_2 ultra-high temperature ceramic *Acta Mater.* **165** 26–39
[277] Simeone D, Hablot O, Micalet V, Bellon P and Serruys Y 1997 Contribution of recoil atoms to irradiation damage in absorber materials *J. Nucl. Mater.* **246** 206–14
[278] Zanini L, Huang Y, Dai Y, Konobeyev A Y and Pitcher E J 2010 Radiation damage and He production calculations for the fourth SINQ target irradiation program, STIP-IV *19th Meeting on Collaboration of Advanced Neutron Sources, ICANS XIX* (*Grindelwald, Switzerland*)
[279] Sawai T, Ando M, Wakai E, Shiba K and Jitsukawa S 2017 Ni-doped F82H to investigate He effects in HFIR irradiation *Fusion Sci. Technol.* **44** 201–5
[280] Schäublin R and Chiu Y L L 2007 Effect of helium on irradiation-induced hardening of iron: a simulation point of view *J. Nucl. Mater.* **362** 152–60
[281] Gaganidze E, Petersen C and Aktaa J 2009 Study of helium embrittlement in boron doped EUROFER97 steels *J. Nucl. Mater.* **386–388** 349–52
[282] Schäublin R, Henry J and Dai Y 2008 Helium and point defect accumulation: (i) microstructure and mechanical behaviour *C. R. Phys.* **9** 389–400
[283] Dai Y, Henry J, Tong Z, Averty X, Malaplate J and Long B 2011 Neutron/proton irradiation and He effects on the microstructure and mechanical properties of ferritic/martensitic steels T91 and EM10 *J. Nucl. Mater.* **415** 306–10
[284] Klueh R L and Sokolov M A 2007 Mechanical properties of irradiated 9Cr–2WVTa steel with and without nickel *J. Nucl. Mater.* **367–370** 102–6
[285] Wakai E, Okubo N, Ando M, Yamamoto T and Takada F 2010 Reduction method of DBTT shift due to irradiation for reduced-activation ferritic/martensitic steels *J. Nucl. Mater.* **398** 64–67
[286] Tanigawa H, Shiba K, Sokolov M A and Klueh R L 2003 Charpy impact properties of reduced-activation ferritic/martensitic steels irradiated in HFIR up to 20 dpa *Fusion Sci. Technol.* **44** 206–10
[287] Hasegawa A, Ejiri M, Nogami S, Ishiga M, Kasada R, Kimura A, Abe K and Jitsukawa S 2009 Effects of helium on ductile-brittle transition behavior of reduced-activation ferritic steels after high-concentration helium implantation at high temperature *J. Nucl. Mater.* **386–388** 241–4
[288] Henry J, Averty X, Dai Y, Pizzanelli J P and Espinas J J 2009 Tensile properties of ODS-14%Cr ferritic alloy irradiated in a spallation environment *J. Nucl. Mater.* **386–388** 345–8
[289] Singh B N and Foreman A J E 1991 Some limitations of simulation studies using the ppm to dpa ratio as the helium generation rate *J. Nucl. Mater.* **179–181** 990–3
[290] Yabuuchi K, Sato K, Nogami S, Hasegawa A, Ando M and Tanigawa H 2014 Effect of He implantation on fracture behavior and microstructural evolution in F82H *J. Nucl. Mater.* **455** 690–4
[291] Hasegawa A and Shiraishi H 1992 Helium implantation effects on low activation 9Cr martensitic steels *J. Nucl. Mater.* **191–194** 910–4
[292] Hasegawa A, Shiraishi H, Matsui H and Abe K 1994 Behavior of helium gas atoms and bubbles in low activation 9Cr martensitic steels *J. Nucl. Mater.* **212–215** 720–4
[293] Schroeder H and Ullmaier H 1991 Helium and hydrogen effects on the embrittlement of iron- and nickel-based alloys *J. Nucl. Mater.* **179–181** 118–24
[294] Schroeder H and Stamm U 1990 High temperature helium embrittlement: austenitic versus martensitic stainless steels *Effects of Radiation on Materials: 14th Int. Symp.* vol I (West Conshohocken, PA: ASTM International) p 223
[295] Kimura A *et al* 2002 High resistance to helium embrittlement in reduced activation martensitic steels *J. Nucl. Mater.* **307–311** 521–6
[296] Ullmaier H and Trinkaus H 1992 Helium in metals: effect on mechanical properties *Mater. Sci. Forum* **97–99** 451–72
[297] Ullmaier H 1984 The influence of helium on the bulk properties of fusion reactor structural materials *Nucl. Fusion* **24** 1039–83
[298] Braski D N, Schroeder H and Ullmaier H 1979 The effect of tensile stress on the growth of helium bubbles in an austenitic stainless steel *J. Nucl. Mater.* **83** 265–77

[299] Stork D *et al* 2014 Materials R&D for a timely DEMO: key findings and recommendations of the EU Roadmap Materials Assessment Group *Fusion Eng. Des.* **89** 1586–94
[300] Odette G R 2018 On the status and prospects for nanostructured ferritic alloys for nuclear fission and fusion application with emphasis on the underlying science *Scr. Mater.* **143** 142–8
[301] Edmondson P D, Parish C M, Zhang Y, Hallén A and Miller M K 2013 Helium bubble distributions in a nanostructured ferritic alloy *J. Nucl. Mater.* **434** 210–6
[302] Lin Y R, Chen W Y, Tan L, Hoelzer D T, Yan Z, Hsieh C Y, Huang C W and Zinkle S J 2021 Bubble formation in helium-implanted nanostructured ferritic alloys at elevated temperatures *Acta Mater.* **217** 117165
[303] Zinkle S J, Möslang A, Muroga T and Tanigawa H 2013 Multimodal options for materials research to advance the basis for fusion energy in the ITER era *Nucl. Fusion* **53** 104024
[304] Was G S 2007 *Fundamentals of Radiation Materials Science* (Berlin: Springer)
[305] Garner F A, Toloczko M B and Sencer B H 2000 Comparison of swelling and irradiation creep behavior of fcc-austenitic and bcc-ferritic/martensitic alloys at high neutron exposure *J. Nucl. Mater.* **276** 123–42
[306] Wakai E *et al* 2002 Effect of triple ion beams in ferritic/martensitic steel on swelling behavior *J. Nucl. Mater.* **307–311** 278–82
[307] Wakai E, Kikuchi K, Yamamoto S, Aruga T, Ando M, Tanigawa H, Taguchi T, Sawai T, Oka K and Ohnuki S 2003 Swelling behavior of F82H steel irradiated by triple/dual ion beams *J. Nucl. Mater.* **318** 267–73
[308] Gelles D S 1996 Microstructural examination of commercial ferritic alloys at 200 dpa *J. Nucl. Mater.* **233–237** 293–8
[309] Toloczko M B, Garner F A, Voyevodin V N, Bryk V V, Borodin O V, Mel'Nychenko V V and Kalchenko A S 2014 Ion-induced swelling of ODS ferritic alloy MA957 tubing to 500 dpa *J. Nucl. Mater.* **453** 323–33
[310] Toloczko M B, Gelles D S, Garner F A, Kurtz R J and Abe K 2004 Irradiation creep and swelling from 400 to 600 °C of the oxide dispersion strengthened ferritic alloy MA957 *J. Nucl. Mater.* **329–333** 352–5
[311] Klimenkov M, Jäntsch U, Rieth M and Möslang A 2020 Correlation of microstructural and mechanical properties of neutron irradiated EUROFER97 steel *J. Nucl. Mater.* **538** 152231
[312] Klimenkov M, Möslang A and Materna-Morris E 2014 Helium influence on the microstructure and swelling of 9%Cr ferritic steel after neutron irradiation to 16.3 dpa *J. Nucl. Mater.* **453** 54–59
[313] Morimura T, Kimura A and Matsui H 1996 Void swelling of Japanese candidate martensitic steels under FFTF/MOTA irradiation *J. Nucl. Mater.* **239** 118–25
[314] Vitek J M and Klueh R L 1984 Microstructure of 9Cr–1MoVNb steel irradiated to 36 dpa at elevated temperatures in HFIR *J. Nucl. Mater.* **122** 254–9
[315] Van Den Bosch J, Anderoglu O, Dickerson R, Hartl M, Dickerson P, Aguiar J A, Hosemann P, Toloczko M B and Maloy S A 2013 SANS and TEM of ferritic-martensitic steel T91 irradiated in FFTF up to 184 dpa at 413 °C *J. Nucl. Mater.* **440** 91–7
[316] Miwa Y, Wakai E, Shiba K, Hashimoto N, Robertson J P, Rowcliffe A F and Hishinuma A 2000 Swelling of F82H irradiated at 673 K up to 51 dpa in HFIR *J. Nucl. Mater.* **283–287** 334–8
[317] Kohno Y, Gelles D S, Kohyama A, Tamura M and Hishinuma A 1992 Irradiation response of a reduced activation Fe–8Cr–2W martensitic steel (F82H) after FFTF irradiation *J. Nucl. Mater.* **191–194** 868–73
[318] Ogiwara H, Sakasegawa H, Tanigawa H, Ando M, Katoh Y and Kohyama A 2002 Void swelling in reduced activation ferritic/martensitic steels under ion-beam irradiation to high fluences *J. Nucl. Mater.* **307–311** 299–303
[319] Hall M M and Flinn J E 2010 Stress state dependence of in-reactor creep and swelling. Part 2: experimental results *J. Nucl. Mater.* **396** 119–29
[320] Konobeevsky T T, Prafdyuk N F and Kutaitsev V I 1955 Effect of irradiation on structure and properties of fissionable materials *UN Conf. on Peaceful Uses of Atomic Energy* vol 7 (New York: United Nations) pp 433–40
[321] Matthews J R and Finnis M W 1988 Irradiation creep models—an overview *J. Nucl. Mater.* **159** 257–85
[322] Wolfer W G 1980 Correlation of radiation creep theory with experimental evidence *J. Nucl. Mater.* **90** 175–92
[323] Heald P T and Speight M V 1974 Steady-state irradiation creep *Phil. Mag.* **29** 1075–80
[324] Mansur L K 1979 Irradiation creep by climb-enabled glide of dislocations resulting from preferred absorption of point defects *Phil. Mag.* A **39** 497–506
[325] Paxton M M, Chin B A, Gilbert E R and Nygren R E 1979 Comparison of the in-reactor creep of selected ferritic, solid solution strengthened, and precipitation hardened commercial alloys *J. Nucl. Mater.* **80** 144–51
[326] Ehrlich K 1981 Irradiation creep and interrelation with swelling in austenitic stainless steels *J. Nucl. Mater.* **100** 149–66
[327] Stoller R E, Grossbeck M L and Mansur L K 1992 A theoretical model of accelerated irradiation creep at low temperatures by transient interstitial absorption *ASTM Special Technical Publication* (West Conshohocken, PA: ASTM International) pp 517–29
[328] Garner F A 2012 Radiation damage in austenitic steels *Comprehensive Nuclear Materials* vol 4 (Oxford: Elsevier) pp 33–95
[329] Uehira A, Mizuta S, Ukai S and Puigh R J 2000 Irradiation creep of 11Cr–0.5Mo–2W,V,Nb ferritic–martensitic, modified 316, and 15Cr–20Ni austenitic S.S. irradiated in FFTF to 103–206 dpa *J. Nucl. Mater.* **283–287** 396–9
[330] Jitsukawa S, Kimura A, Kohyama A, Klueh R L, Tavassoli A A, van der Schaaf B, Odette G R, Rensman J W, Victoria M and Petersen C 2004 Recent results of the reduced activation ferritic/martensitic steel development *J. Nucl. Mater.* **329–333** 39–46
[331] Garner F A and Gelles D S 1988 Irradiation creep mechanisms: an experimental perspective *J. Nucl. Mater.* **159** 286–309
[332] Gelles D S, Garner F A and Brager H R 1981 Frank loop formation in irradiated metals in response to applied and internal stresses *ASTM Special Technical Publication* (West Conshohocken, PA: ASTM International) pp 735–53
[333] Toloczko M B, Garner F A and Maloy S A 2012 Irradiation creep and density changes observed in MA957 pressurized tubes irradiated to doses of 40–110 dpa at 400–750 °C in FFTF *J. Nucl. Mater.* **428** 170–5
[334] Toloczko M B, Garner F A and Eiholzer C R 1994 Irradiation creep and swelling of the US fusion heats of HT9 and 9Cr–1Mo to 208 dpa at ∼400 °C *J. Nucl. Mater.* **212–215** 604–7
[335] Walters L C and Ruther W E 1977 In-reactor stress relaxation of Inconel X75O springs *J. Nucl. Mater.* **68** 324–33
[336] Lemaitre J and Plumtree A 1979 Application of damage concepts to predict creep-fatigue failures *J. Eng. Mater. Technol.* **101** 284–92
[337] Rolfe S T and Barsom J M 1977 *Fracture and Fatigue Control in Structures. Applications of Fracture Mechanics* (Englewood Cliffs, NJ: Prentice-Hall)
[338] Kasahara N, Satoh K, Tsukimori K and Kawasaki N 2011 Proposals of guidelines for high temperature structural design of fast reactor vessels *Am. Soc. Mech. Eng. Press. Vessels Pip. Div. (Publ.) PVP* **1** 315–22
[339] Marie S, Drubay B, Berton M N, Gelineau O, Escaravage C, Bonne D and Sperandio M 2010 Presentation of RCC-MR code 2007 for high temperature reactor and ITER projects: general overview *Am. Soc. Mech. Eng. Press. Vessels Pip. Div. (Publ.) PVP* **1** 771–7
[340] Hoffelner W 2010 Damage assessment in structural metallic materials for advanced nuclear plants *J. Mater. Sci.* **45** 2247–57

[341] Asayama T and Tachibana Y 2008 *Creep-Fatigue Data and Evaluation Procedures for Grade 91 Steel and Hastelloy XR for VHTR. STP-NU-018* (New York: ASME Standards Technology, LLC) p 162
[342] Sham T L and Zinkle S J 2010 Creep and fatigue issues for structural materials in demonstration fusion energy systems *Trans. Indian Inst. Met.* **63** 331–7
[343] Tavassoli A A F, Fournier B and Sauzay M 2010 High temperature creep-fatigue design *Trans. Indian Inst. Met.* **63** 235–44
[344] Tanigawa H *et al* 2008 Technical issues of reduced activation ferritic/martensitic steels for fabrication of ITER test blanket modules *Fusion Eng. Des.* **83** 1471–6
[345] Zinkle S J, Terrani K A and Snead L L 2016 Motivation for utilizing new high-performance advanced materials in nuclear energy systems *Curr. Opin. Solid State Mater. Sci.* **20** 401–10
[346] Pintsuk G, Diegele E, Dudarev S L, Gorley M, Henry J, Reiser J and Rieth M 2019 European materials development: results and perspective *Fusion Eng. Des.* **146** 1300–7
[347] Abe F 2008 Precipitate design for creep strengthening of 9% Cr tempered martensitic steel for ultra-supercritical power plants *Sci. Technol. Adv. Mater.* **9** 013002
[348] Abe F 2011 Strengthening mechanisms in creep of advanced ferritic power plant steels based on creep deformation analysis *Advanced Steels* (New York: Springer) pp 409–22
[349] Vitek J M and Klueh R L 1983 Precipitation reactions during the heat treatment of ferritic steels *Metall. Trans.* A **14** 1047–55
[350] Klimenkov M, Lindau R, Materna-Morris E and Möslang A 2012 TEM characterization of precipitates in EUROFER 97 *Prog. Nucl. Energy* **57** 8–13
[351] Fernández P, Lancha A M, Lapeña J, Serrano M and Hernández-Mayoral M 2002 Metallurgical properties of reduced activation martensitic steel Eurofer'97 in the as-received condition and after thermal ageing *J. Nucl. Mater.* **307–311** 495–9
[352] Ennis P J, Zielinska-Lipiec A, Wachter O and Czyrska-Filemonowicz A 1997 Microstructural stability and creep rupture strength of the martensitic steel P92 for advanced power plant *Acta Mater.* **45** 4901–7
[353] Hald J and Korcakova L 2003 Precipitate stability in creep resistant ferritic steels-experimental investigations and modelling *ISIJ Int.* **43** 420–7
[354] Tan L, Parish C M and Hu X 2018 Microstructure and property tailoring of castable nanostructured alloys through thermomechanical treatments *J. Nucl. Mater.* **509** 267–75
[355] Tan L, Graening T, Hu X, Zhong W, Yang Y, Zinkle S J and Katoh Y 2020 Effects of carbonitrides and carbides on microstructure and properties of castable nanostructured alloys *J. Nucl. Mater.* **540** 152376
[356] Hald J 2017 High-alloyed mastensitic steel grades for boilers in ultra-supercritical power plants *Materials for Ultra-Supercritical and Advanced Ultra-Supercritical Power Plants* ed A Di Gianfrancesco (Cambridge: Woodhead Publishing) pp 77–97
[357] Tan L, Katoh Y and Snead L L 2018 Development of castable nanostructured alloys as a new generation RAFM steels *J. Nucl. Mater.* **511** 598–604
[358] Masuyama F and Shingledecker J P 2013 Recent status of ASME code on creep strength enhanced ferritic steels *Proc. Eng.* **55** 314–25
[359] Pintsuk G, Aiello G, Dudarev S, Gorley M, Henry J, Richou M, Rieth M, Terentyev D and Vila R Creep performance of 3%W-B added RAFM steels *Fusion Eng. Des.*
[360] Cristalli C, Pilloni L, Tassa O, Bozzetto L, Sorci R and Masotti L 2018 Development of innovative steels and thermo-mechanical treatments for DEMO high operating temperature blanket options *Nucl. Mater. Energy* **16** 175–80
[361] Materna-Morris E *et al* 2007 Structural material EUROFER97-2, characterization of rod and plate material: structural, tensile, charpy, and creep properties *Report on the EFDA Task* TW4-TTMS-005 D2 (Germany: Karlsruhe Institute of Technology)
[362] Anon 2005 *European Creep Collaborative Committee (ECCC) Datasheets, ASTM Grade91 and Grade92*
[363] Fujita T 1992 Review of current progress in adbanced high temperature ferritic martensitic steels for high-temperature applications *ISIJ Int.* **32** 81
[364] Hättestrand M and Andrén H O 1999 Boron distribution in 9–12% chromium steels *Mater. Sci. Eng.* A **270** 33–7
[365] Hättestrand M, Schwind M and Andrén H-O 1998 Microanalysis of two creep resistant 9–12% chromium steels *Mater. Sci. Eng.* A **1** 27–36
[366] Liu F, Fors D H R, Golpayegani A, Andrén H O and Wahnström G 2012 Effect of boron on carbide coarsening at 873 K (600 °C) in 9 to 12 pct chromium steels *Metall. Mater. Trans.* A **43** 4053–62
[367] Klueh R L 2008 Reduced-activation steels: future development for improved creep strength *J. Nucl. Mater.* **378** 159–66
[368] Abe F 2005 Effect of fine precipitation and subsequent coarsening of Fe2W laves phase on the creep deformation behavior of tempered martensitic 9Cr-W steels *Metall. Mater. Trans.* A **36** 321–32
[369] Tan L, Busby J T, Maziasz P J and Yamamoto Y 2013 Effect of thermomechanical treatment on 9Cr ferritic–martensitic steels *J. Nucl. Mater.* **441** 713–7
[370] Vivas J, Capdevila C, Altstadt E, Houska M and San-Martín D 2018 Importance of austenitization temperature and ausforming on creep strength in 9Cr ferritic/martensitic steel *Scr. Mater.* **153** 14–8
[371] Vivas J, Capdevila C, Jimenez J A, Benito-Alfonso M and San-Martin D 2017 Effect of ausforming temperature on the microstructure of G91 steel *Metals* **7** 236
[372] Hoffmann J, Rieth M, Commin L, Fernández P and Roldán M 2016 Improvement of reduced activation 9%Cr steels by ausforming *Nucl. Mater. Energy* **6** 12–17
[373] Poizin E 2015 Effect of thermomechanical treatments on the microstructure and mechanical properties of 9%Cr martensitic steel (Grade 91), CEA-R-6402 *PhD Thesis* CEA-Saclay
[374] Tan L, Yang Y and Busby J T 2013 Effects of alloying elements and thermomechanical treatment on 9Cr Reduced Activation Ferritic-Martensitic (RAFM) steels *J. Nucl. Mater.* **442** S13–S17
[375] Abdou M A, Wittenberg L J and Maynard C W 1975 A fusion design study of nonmobile blankets with low lithium and tritium inventories *Nucl. Technol.* **26** 400–19
[376] Nakamura H, Sakurai S, Suzuki S, Hayashi T, Enoeda M and Tobita K 2006 Case study on tritium inventory in the fusion DEMO plant at JAERI *Fusion Eng. Des.* **81** 1339–45
[377] Serra E, Benamati G and Ogorodnikova O V 1998 Hydrogen isotopes transport parameters in fusion reactor materials *J. Nucl. Mater.* **255** 105–15
[378] Serra E, Perujo A and Benamati G 1997 Influence of traps on the deuterium behaviour in the low activation martensitic steels F82H and Batman *J. Nucl. Mater.* **245** 108–14
[379] Esteban G A, Peña A, Legarda F and Lindau R 2007 Hydrogen transport and trapping in ODS-EUROFER *Fusion Eng. Des.* **82** 2634–40

[380] Esteban G A, Peña A, Urra I, Legarda F and Riccardi B 2007 Hydrogen transport and trapping in EUROFER'97 *J. Nucl. Mater.* **367–370** 473–7
[381] Higaki M, Otsuka T, Tokunaga K, Hashizume K, Ezato K, Suzuki S, Enoeda M and Akiba M 2015 Determination of hydrogen diffusion coefficients in F82H by hydrogen depth profiling with a tritium imaging plate technique *Fusion Sci. Technol.* **67** 379–81
[382] Otsuka T, Goto K, Sakamoto K and Hashizume K 2018 Chemical forms of hydrogen desorbed by permeation through pure iron and oxide dispersion strengthened steels *Fusion Eng. Des.* **132** 107–9
[383] Aiello A, Ricapito I, Benamati G and Valentini R 2002 Hydrogen isotopes permeability in Eurofer 97 martensitic steel *Fusion Sci. Technol.* **41** 872–6
[384] Chen Z, Hu X, Ye M and Wirth B D 2021 Deuterium transport and retention properties of representative fusion blanket structural materials *J. Nucl. Mater.* **549** 152904
[385] Urabe Y, Hashizume K, Otsuka T and Sakamoto K 2020 Tritium permeation through Ce-ODS steel *Fusion Sci. Technol.* **76** 392–7
[386] Sakamoto K *et al* 2021 Development of accident tolerant FeCrAl-ODS fuel cladding for BWRs in Japan *J. Nucl. Mater.* **557** 153276
[387] Emelyanova O V, Ganchenkova M G, Malitskii E, Yagodzinskyy Y N, Klimenkov M, Borodin V A, Vladimirov P V, Lindau R, Möslang A and Hänninen H 2016 Investigation of microstructure changes in ODS-EUROFER after hydrogen loading *J. Nucl. Mater.* **468** 355–9
[388] Huang G-Y, Hu X and Wirth B D 2020 First-principles investigations of hydrogen trapping in Y_2O_3 and the Y_2O_3 |bcc Fe interface *J. Phys.: Condens. Matter* **32** 495001
[389] Bhattacharya A, Parish C M, Henry J and Katoh Y 2019 High throughput crystal structure and composition mapping of crystalline nanoprecipitates in alloys by transmission Kikuchi diffraction and analytical electron microscopy *Ultramicroscopy* **202** 33–43
[390] Tissot O, Pareige C, Mathon M-H, Roussel M, Meslin E, Décamps B and Henry J 2019 Comparison between SANS and APT measurements in a thermally aged Fe–19 at.%Cr alloy *Mater. Charact.* **151** 332–41
[391] Miller M K, Wirth B D and Odette G R 2003 Precipitation in neutron-irradiated Fe–Cu and Fe–Cu–Mn model alloys: a comparison of APT and SANS data *Mater. Sci. Eng.* A **353** 133–9
[392] Edmondson P D, Parish C M and Nanstad R K 2017 Using complimentary microscopy methods to examine Ni–Mn–Si-precipitates in highly-irradiated reactor pressure vessel steels *Acta Mater.* **134** 31–39
[393] Kano S, Yang H, Shen J, Zhao Z, McGrady J, Hamaguchi D, Ando M, Tanigawa H and Abe H 2018 Instability of MX and M23C6 type precipitates in F82H steels under 2.8 MeV Fe2+ irradiation at 673 K *Nucl. Mater. Energy* **17** 56–61
[394] Bhattacharya A, Levine S M, Zinkle S J, Chen W-Y, Baldo P, Parish C M and Edmondson P D 2022 Radiation induced amorphization of carbides in additively manufactured and conventional ferritic-martensitic steels: *in-situ* experiments on extraction replicas *J. Nucl. Mater.* **563** 153646
[395] Williams C A, Marquis E A, Cerezo A and Smith G D W 2010 Nanoscale characterisation of ODS-Eurofer 97 steel: an atom-probe tomography study *J. Nucl. Mater.* **400** 37–45
[396] Wu Y, Haney E M, Cunningham N J and Odette G R 2012 Transmission electron microscopy characterization of the nanofeatures in nanostructured ferritic alloy MA957 *Acta Mater.* **60** 3456–68
[397] Miller M K, Fu C L, Krcmar M, Hoelzer D T and Liu C T 2009 Vacancies as a constitutive element for the design of nanocluster-strengthened ferritic steels *Front. Mater. Sci. China* **3** 9–14
[398] Reader S W, Mitchell M R, Johnston K E, Pickard C J, Whittle K R and Ashbrook S E 2009 Cation disorder in pyrochlore ceramics: 89Y MAS NMR and first-principles calculations *J. Phys. Chem.* C **113** 18874–83
[399] Farnan I, Cho H and Weber W J 2007 Quantification of actinide α-radiation damage in minerals and ceramics *Nature* **445** 190–3
[400] Sickafus K E, Grimes R W, Valdez J A, Cleave A R, Tang M, Ishimaru M, Corish S M, Stanek C R and Uberuaga B P 2007 Radiation-induced amorphization resistance and radiation tolerance in structurally related oxides *Nat. Mater.* **6** 217–23
[401] Donnelly S E 1985 The density and pressure of helium in bubbles in implanted metals: a critical review *Radiat. Eff.* **90** 1–47
[402] Jenkins M L 1994 Characterisation of radiation-damage microstructures by TEM *J. Nucl. Mater.* **216** 124–56
[403] Fréchard S, Walls M, Kociak M, Chevalier J P, Henry J and Gorse D 2009 Study by EELS of helium bubbles in a martensitic steel *J. Nucl. Mater.* **393** 102–7
[404] David M L, Pailloux F, Mauchamp V and Pizzagalli L 2011 In situ probing of helium desorption from individual nanobubbles under electron irradiation *Appl. Phys. Lett.* **98** 171903
[405] Krivanek O L, Lovejoy T C, Murfitt M F, Skone G, Batson P E and Dellby N 2014 Towards sub-10 meV energy resolution STEM-EELS *J. Phys.: Conf. Ser.* **522** 012023
[406] Yang L, Jiang Y, Odette G R, Yamamoto T, Liu Z and Liu Y 2014 Trapping helium in Y2Ti2O7 compared to in matrix iron: a first principles study *J. Appl. Phys.* **115** 143508
[407] Lin Y-R, Chen W-Y, Li M, Henry J and Zinkle S J 2021 Dynamic observation of dual-beam irradiated Fe and Fe–10Cr alloys at 435°C *Acta Mater.* **209** 116793
[408] Gilbert M R *et al* 2021 Perspectives on multiscale modelling and experiments to accelerate materials development for fusion *J. Nucl. Mater.* **554** 153113
[409] Sublet J C *et al* 2019 Neutron-induced damage simulations: beyond defect production cross-section, displacement per atom and iron-based metrics *Eur. Phys. J. Plus* **134** 1–50
[410] Gilbert M R and Sublet J C 2018 Differential dpa calculations with SPECTRA-PKA *J. Nucl. Mater.* **504** 101–8
[411] Gilbert M R, Marian J and Sublet J C 2015 Energy spectra of primary knock-on atoms under neutron irradiation *J. Nucl. Mater.* **467** 121–34
[412] Greenwood L R and Smither R K 1985 SPECTER: neutron damage calculations for materials irradiations *Fusion Power Program Report* ANL/FPP/TM-197 (Argonne, IL: Argonne National Lab)
[413] Iwamoto Y, Sato T, Hashimoto S, Ogawa T, Furuta T, Abe S I, Kai T, Matsuda N, Hosoyamada R and Niita K 2017 Benchmark study of the recent version of the PHITS code *J. Nucl. Sci. Technol.* **54** 617–35
[414] Sato T *et al* 2018 Features of Particle and Heavy Ion Transport code System (PHITS) version 3.02 *J. Nucl. Sci. Technol.* **55** 684–90
[415] Huang C H, Gilbert M R and Marian J 2018 Simulating irradiation hardening in tungsten under fast neutron irradiation including Re production by transmutation *J. Nucl. Mater.* **499** 204–15
[416] Luneville L and Simeone D 2016 DART, a BCA code to assess and compare primary irradiation damage in nuclear materials submitted to neutron and ion flux *EPJ Web Conf.* **115** 02002
[417] Lunéville L, Simeone D and Jouanne C 2006 Calculation of radiation damage induced by neutrons in compound materials *J. Nucl. Mater.* **353** 89–100
[418] Sublet J C, Eastwood J W, Morgan J G, Gilbert M R, Fleming M and Arter W 2017 FISPACT-II: an advanced simulation system for activation, transmutation and material modelling *Nucl. Data Sheets* **139** 77–137

[419] Gilbert M R, Packer L W, Sublet J-C and Forrest R A 2014 Inventory simulations under neutron irradiation: visualization techniques as an aid to materials design *Nucl. Sci. Eng.* **177** 291–306
[420] Soisson F and Jourdan T 2016 Radiation-accelerated precipitation in Fe–Cr alloys *Acta Mater.* **103** 870–81
[421] Ke J H, Reese E R, Marquis E A, Odette G R and Morgan D 2019 Flux effects in precipitation under irradiation—simulation of Fe–Cr alloys *Acta Mater.* **164** 586–601
[422] Balbuena J P, Malerba L, Castin N, Bonny G and Caturla M J 2021 An object kinetic Monte Carlo method to model precipitation and segregation in alloys under irradiation *J. Nucl. Mater.* **557** 153236
[423] Chiapetto M, Becquart C S and Malerba L 2016 Simulation of nanostructural evolution under irradiation in Fe–9%CrC alloys: an object kinetic Monte Carlo study of the effect of temperature and dose-rate *Nucl. Mater. Energy* **9** 565–70
[424] Chiapetto M, Malerba L and Becquart C S 2015 Effect of Cr content on the nanostructural evolution of irradiated ferritic/martensitic alloys: an object kinetic Monte Carlo model *J. Nucl. Mater.* **465** 326–36
[425] Bhattacharya A, Meslin E, Henry J, Barbu A, Poissonnet S and Décamps B 2016 Effect of chromium on void swelling in ion irradiated high purity Fe–Cr alloys *Acta Mater.* **108** 241–51
[426] Bonny G, Terentyev D and Malerba L 2010 New contribution to the thermodynamics of Fe–Cr alloys as base for ferritic steels *J. Phase Equilib. Diffus.* **31** 439–44
[427] Dudarev S L, Mason D R, Tarleton E, Ma P W and Sand A E 2018 A multi-scale model for stresses, strains and swelling of reactor components under irradiation *Nucl. Fusion* **58** 126002
[428] Reali L, Boleininger M, Gilbert M R and Dudarev S L 2022 Macroscopic elastic stress and strain produced by irradiation *Nucl. Fusion* **62** 016002
[429] Sand A E, Byggmästar J, Zitting A and Nordlund K 2018 Defect structures and statistics in overlapping cascade damage in fusion-relevant bcc metals *J. Nucl. Mater.* **511** 64–74
[430] Sand A E, Aliaga M J, Caturla M J and Nordlund K 2016 Surface effects and statistical laws of defects in primary radiation damage: tungsten vs. iron *Europhys. Lett.* **115** 36001
[431] Derlet P M and Dudarev S L 2020 Microscopic structure of a heavily irradiated material *Phys. Rev. Mater.* **4** 023605
[432] Mason D R *et al* 2020 Observation of transient and asymptotic driven structural states of tungsten exposed to radiation *Phys. Rev. Lett.* **125** 225503
[433] Fedorov M, Wróbel J S, Fernández-Caballero A, Kurzydłowski K J and Nguyen-Manh D 2020 Phase stability and magnetic properties in fcc Fe–Cr–Mn–Ni alloys from first-principles modeling *Phys. Rev.* B **101** 174416
[434] Goryaeva A M, Lapointe C, Dai C, Dérès J, Maillet J B and Marinica M C 2020 Reinforcing materials modelling by encoding the structures of defects in crystalline solids into distortion scores *Nat. Commun.* **11** 4691
[435] Elias M T and El-Guebaly L 2015 *Shielding and Activation Analyses for Outboard Region of FESS-FNSF Design* (Madison, WI: Fusion Technology Institute, University of Wisconsin—Madison)
[436] Davis A, Harb M, El-Guebaly L, Wilson P and Marriott E 2018 Neutronics aspects of the FESS-FNSF *Fusion Eng. Des.* **135** 271–8
[437] Yamamoto T and Robert Odette G 2019 Fusion relevant engineering void swelling model for 9Cr tempered martensitic steels *DOE-FES Fusion Semiannual Technical Report* DOE/ER-0313/67 vol 67 (Oak Ridge, TN)
[438] Yamamoto T and Robert Odette G 2020 Constitutive models for hardening of tempered martensitic steels at 300 to 500 C up to high dpa and helium *DOE-FES Fusion Semiannual Technical Report. Fusion Reactor Materials Semiannual Report* DOE/ER-0313/68 vol 68 (Oak Ridge, TN)
[439] Alam E, Yamamoto T and Robert Odette G 2020 Primary creep models for 9CrW tempered martensitic steels: effects on the high-temperature dimensional stability of fusion structures *DOE-FES Fusion Semiannual Technical Report. Fusion Reactor Materials Semiannual Report* DOE/ER-0313/68 vol 68 (Oak Ridge, TN)
[440] Ghazari A, Forte R, Yamamoto T, Odette R and Ghoniem N 2021 Radiation effects on stress evolution and dimensional stability of large fusion energy structures *Fusion Eng. Des.* **172** 112756
[441] Atchutuni S S, Agravat H S, Chauhan J P and Kumar R 2018 Corrosion behavior of IN-RAFM steel with stagnant lead-lithium at 550 °C up to 9000 h *Fusion Eng. Des.* **135** 102–9
[442] Hernández T, Gázquez M C, Sánchez F J and Malo M 2018 Corrosion mechanisms of Eurofer produced by lithium ceramics under fusion relevant conditions *Nucl. Mater. Energy* **15** 110–4
[443] Bassini S, Cuzzola V, Antonelli A and Utili M 2020 Long-term corrosion behavior of EUROFER RAFM steel in static liquid Pb–16Li at 550 °C *Fusion Eng. Des.* **160** 111829
[444] Unocic K A, Hoelzer D T and Pint B A 2015 Microstructure and environmental resistance of low Cr ODS FeCrAl *Mater. High Temp.* **32** 123–32
[445] Pint B A, Dryepondt S, Unocic K A and Hoelzer D T 2014 Development of ODS FeCrAl for compatibility in fusion and fission energy applications *JOM* **66** 2458–66
[446] Jun J, Unocic K A, Lance M J, Meyer H M and Pint B A 2020 Compatibility of FeCrAlMo with flowing PbLi at 500 °C–650 °C *J. Nucl. Mater.* **528** 151847
[447] Wulf S E, Krauss W and Konys J 2018 Long-term corrosion behavior of Al-based coatings in flowing Pb–15.7Li, produced by electrochemical ECX process *Nucl. Mater. Energy* **16** 158–62
[448] Glasbrenner H, Konys J, Voss Z and Wedemeyer O 2002 Corrosion behaviour of Al based tritium permeation barriers in flowing Pb–17Li *J. Nucl. Mater.* **307–311** 1360–3
[449] Krauss W, Konys J, Holstein N and Zimmermann H 2011 Al-based anti-corrosion and T-permeation barrier development for future DEMO blankets *J. Nucl. Mater.* **417** 1233–6
[450] Pint B A, Jun J and Romedenne M 2021 Compatibility of SiC with ODS FeCrAl in flowing Pb-Li at 600 °C–700 °C *Fusion Eng. Des.* **166** 112389
[451] Norajitra P *et al* 2004 Development of a helium-cooled divertor concept: design-related requirements on materials and fabrication technology *J. Nucl. Mater.* **329–333** 1594–8
[452] Takahashi K, Kobayashi N, Ohmori J, Suzuki S, Kasugai A and Sakamoto K 2017 Progress on design and development of ITER equatorial launcher: analytical investigation and R&D of the launcher components for the design improvement *Fusion Sci. Technol.* **52** 266–80